Rediscovery of the Microtubule System in Chlamydomonas

Yi Liu
Marquette University

REDISCOVERY OF THE MICROTUBULE SYSTEM IN *CHLAMYDOMONAS*

by

Yi Liu, B.S.

A Dissertation submitted to the Faculty of the Graduate School,
Marquette University,
in Partial Fulfillment of the Requirements for
the Degree of Doctor of Philosophy

Milwaukee, Wisconsin

August 2017

ABSTRACT

REDISCOVERY OF THE MICROTUBULE SYSTEM IN *CHLAMYDOMONAS*

Yi Liu, B.S.

Marquette University, 2017

Extensive studies have revealed the complex mechanisms underlying the roles of the microtubule system in fundamental cellular processes, the severe consequences in development and health resulted from its anomaly, and the irreplaceable therapeutic agents that perturbs this vital yet inherently unstable cytoskeletal system. Most of the concepts derived from a handful of model organisms become dogma of the field despite contrary observations. By overcoming a major limitation of biflagellate green alga *Chlamydomonas* - the intense autofluorescence common to photosynthetic cells - this dissertation discovered new phenomena of the microtubule system and conceived an invention. The microtubule system of the green alga is exceedingly sensitive to H^+ and Na^+ , contrary to the perceived tight control of this cytoskeleton in best known for its dynamic instability, but similar to stress-induced changes in plants. This indicates that this presumptive conserved system has diverged substantially. Organisms potentially could use a sensitive microtubule system to sense mechanical force as well as osmotic pressures. On the other hand, they must adapt or perish when global environments promise to alter the concentrations of H^+ and Na^+ at an accelerated pace in the coming decades. H^+ and Na^+ -induced changes of algal microtubule system are rapid. Quantification of the rapid responses in real-time inspired the conversion of the microtubule-based biological nanomachine that drives the rhythmic beating of *Chlamydomoans* flagella into fluorescent intensity standards. The large-scale preparation of flagellar standards from the transgenic green algae will accelerate broad implementation of quantitative fluorescence microscopy. Collectively, its two outcomes will have broad impacts on multiple fronts. This dissertation encourages researchers to take a fresh look at the well-understood microtubule system in the green algae.

ACKNOWLEDGEMENTS

Yi Liu, B.S.

I would like to give my deepest and sincerest thanks to my mentor, Dr. Pinfen Yang. I have been so fortunate to have such a fabulous advisor during my graduate study at Marquette University. Her enthusiasm, creativity, and foresightedness have deeply reshaped my perception and understanding of doing science. Her advice and guidance help me grow as a critical and careful thinker. Especially, I want to thank her for exposing me to the field of fluorescence microscopy, which illuminates my passion for biology. I would have never accomplished this dissertation without her support!

I would also like to thank all my committee members, Dr. Stephen Downs, Dr. Thomas Eddinger, Dr. Michelle Mynlieff, and Dr. Michael Schlappi for putting out their suggestions and advice on my research and dissertation.

I would like to thank my lab member, Xiaoyan Zhu for what she has done to make lab organized and all the autolysin she has made for my *Chlamydomonas* transformation.

I would like to give my special thanks to my best buddies in Milwaukee, Fengchao Wang and Yuning Chen for all the help and happiness they gave to me. I treasure every moment that we had together! Also, thanks Rui Gu and Xiangyu Zhou for their tremendous help when I was in difficulties.

Although words are powerless when I am expressing my gratefulness to my dear family, I would simply like to thank my parents for everything. Without your support and give, nothing would have been possible!

TABLE OF CONTENTS

LIST OF TABLES

LIST OF FIGURES

LIST OF ABBREVIATIONS

ARMC	Armadillo Repeat Containing
BAC	Bacterial Artificial Chromosome
CCD	Charge Coupled Device
CH domain	Caponin Homology domain
CrEB1	*Chlamydomonas* End-Binding 1 protein
CrGFP	*Chlamydomonas* Green Fluorescent Protein
Ddw	Double Distilled Water
Dhc	Dynein Heavy Chain
EB	End-Binding protein
EBH domain	EB Homology domain
EGFP	Enhanced Green Fluorescent Protein
EGTA	Ethylene Glycol-bis(β-Aminoethyl Ether)-N,N,N',N'-Tetraacetic Acid
EM	Electron Microscopy
FAP	Flagella-Associated Protein
FITC	Fluorescein Isothiocyanate
Fla	Flagella
FP	Fluorescent Protein
GDP	Guanosine Diphosphate
GFP	Green Fluorescent Protein
GTP	Guanosine Triphosphate
HA	Acetic Acid
HAHis	Hemagglutinin Histidine
HEPES	4-(2-Hydroxyethyl)-1-Piperazineethanesulfonic Acid
SDS-PAGE	Sodium Dodecyl Sulfate Polyacrylamide Gel Electrophoresis
Hyg	Hygromycin
IC	Dynein Intermediate Chain
IFT	Intraflagellar Transport
Lf	Long flagella
MAP	Microtubule-Associated Protein
MT	Microtubule
MTOC	Microtubule-Organizing Center
NDK	Nucleoside-Diphosphate Kinase
NG	NeonGreen
PCR	Polymerase Chain Reaction
PDB	Protein Data Bank
Pf	Paralyzed Flagella
PMM	Paromomycin

PMSF	Phenylmethane Sulfonyl Fluoride
ROI	Region of Interest
RS	Radial Spoke
RSP	Radial Spoke Protein
S/B	Signal to Background Ratio
SOS	Salt Overly Sensitive
TAP	Tris/Acetate/Phosphate
Tub	Tubulin
WT	Wild Type

CHAPTER 1: INTRODUCTION

1.1 The Model System of *Chlamydomonas*

Chlamydomonas reinhardtii, a unicellular biflagellated fresh water green alga, has been used as a model organism to elucidate a number of fundamental questions. With genetic and cellular features of both animal and plant cells, *Chlamdyomonas* is proposed to preserve many genes that were lost during evolution of the common ancestor of land plant and animals (Merchant *et al.*, 2007). It is easy and economical to culture in standard laboratories. It is amenable to various classical and modern experimental approaches (Jinkerson and Jonikas, 2015; Mussgnug, 2015; Shin *et al.*, 2016). Its short doubling time hastens turnover of experiments. Importantly, like *Saccharomyces cerevisiae*, its haploid genome simplifies genetic approaches. Completion of its genome sequencing (Merchant *et al.*, 2007) further empowers this experimental system.

For example, *Chlamydomonas* has been an indispensable tool for the studies of chloroplast biology, photosynthesis and plant metabolism (Harris, 2001). In the era that is seeking new energy sources alternative to fossil fuel, this microalga has now become a go-to system to address key challenges in the biofuel industry (Scranton *et al.*, 2015).

Research of its two flagella is instrumental to the current expansive field of flagellar biology. Diverse organisms use flagella and synonymous cilia to propel themselves in surrounding fluid. The regulated rhythmic beating has enchanted biologists since they were first visualized more than three hundred years ago by Leeuwenhoek. The combined experimental advantages of *Chlamydomonas* made it possible to elucidate the

complicated microtubule (MT)-based machinery that converts chemical energy into rhythmic movements (Lindemann and Lesich, 2010). The findings of algal dynein motor species fueled the elucidation of molecular motors in general (Roberts *et al.*, 2013).

The discovery of a second motion, intracellular transport (IFT) (Kozminski *et al.*, 1993) that occurs along the length of *Chlamydomonas* mutant flagella, ignited the renaissance of flagellar biology and revolutionized the concept of eukaryotic sensory mechanisms. The bi-directional trafficking mechanism has proven to be evolutionarily conserved for delivering a wide array of molecules into and out of cilia and flagella for ciliogenesis, signal transduction and developmental control (Rosenbaum and Witman, 2002; Scholey and Anderson, 2006; Taschner and Lorentzen, 2016). This milestone in the history of the cytoskeleton field allowed scientists finally to conceptualize how eukaryotic cilia and flagella are built and how these slender organelles communicate with the cell body. A wealth of discoveries led to the conclusion that cilia and flagella are also the signaling center of nucleated cells (Scholey and Anderson, 2006; Lechtreck *et al.*, 2009) in multicellular animals and that defects in the signaling process underlie a host of congenital disorders, collectively referred to ciliopathies (Habbig and Liebau, 2015).

Another ground-breaking event is the discovery is light-gated cation channels, channelrhodopsin I and channelrhodopsin II. Illumination-elicited depolarization through these channels signals phototactic responses (Nagel *et al.*, 2002; Nagel *et al.*, 2003). The subsequent changes of $[Ca^{2+}]$ in the two flagella influences green algae swimming directions during the photoresponse (Yoshimura, 2011). Subsequently these green algal light-gated channels were genetically engineered into optical tools, launching the field of optogenetics. For example, expression of channelrhodopsins in neurons allows scientists

to activate subsets of neurons using a light beam with unprecedented spacious and temporal precision. Optogenetics has become an indispensable tool in modern neuroscience research (Deisseroth, 2011; Hegemann and Moglich, 2011).

1.2 The Similarities and Divergence of the MT System

While *Chlamydomonas* has been used for the study of microtubules and flagella for four decades, its potential for the study of the MT system has not been fully realized. The 9+2 MT scaffold in flagella is only part of a sophisticated cytoskeletal system that is integral to numerous processes in eukaryotic cells. MTs are hollow tubes typically comprised of 13 protofilaments polymerized from heterodimers of α- and β-tubulins (**Figure 1.1**). The cylindrical polymers are directional with the β-tubulin end designated as the plus end, based on the faster rate of stochastically growing and shrinking than the minus end that terminates with α-tubulin (Gardner *et al.*, 2013). The polarity, the seemingly random dynamic instability (Mitchison and Kirschner, 1984) and the distinct properties of both ends are harnessed for vital processes by a number of post-translational modifiers and a wide array of accessory proteins (Song and Brady, 2015), including MT associated proteins (MAPs) and molecular motors for purposeful actions, such as transportation, steering MT orientations, stabilizing and destailizing MTs, in space and time (Helenius *et al.*, 2006; Akhmanova and Steinmetz, 2010; Kumar and Wittmann, 2012; Roberts *et al.*, 2013).

Polarized MTs are literally central for establishing the polarity of cells (Siegrist and Doe, 2007). MT triplets form the centrioles, in the centrosome, which is located near the nucleus inside typical animal cells (Bornens, 2008). As the MT organizing center

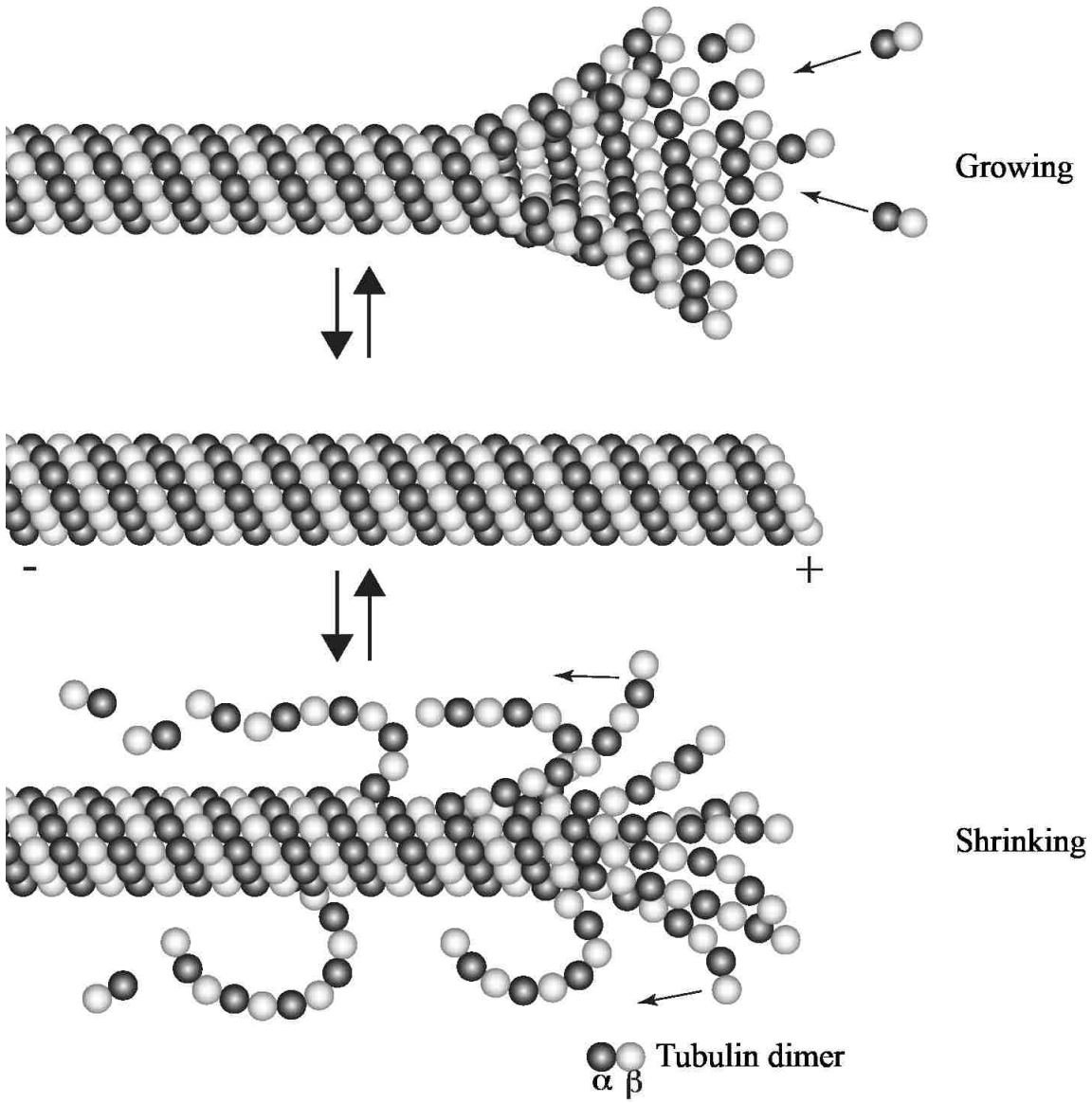

Figure 1.1. A schematic illustrating MT dynamic instability. + and – depicts respectively the directions of the plus-end and minus-end of a microtubule.

(MTOC), the centrosome nucleates numerous MTs (Conduit *et al.*, 2015) - including the MT doublets in cilia and flagella (Harris, 2001) - with plus ends directing toward the

periphery (Piehl *et al.*, 2004). Assisted by accessory proteins, the dynamic system spanning the entire cytosolic space positions and distributes intracellular contents in timely fashion at interphase. The organization is tightly coupled to the cell cycle (Akhmanova and Steinmetz, 2015). Prior to cell division, flagella resorb and the system is converted into the mitotic apparatus that drives the segregations of chromosomes. Given these crucial roles, it is not surprising that MTs are the target of natural toxins (Mukhtar *et al.*, 2014), such as Taxol and colchicine that are used to treat cancers (Weaver, 2014) and gout (Cocco *et al.*, 2010), respectively. These two compounds bind to tubulins directly to stabilize and destabilize MTs (Ravelli *et al.*, 2004; Xiao *et al.*, 2006). Similarly, a host of synthetic herbicides directly bind to tubulins, perturbing the assembly and disassembly of MTs (Hashimoto, 2015),

Notably, the organization of MTs in animal and plant cells differs substantially. The plant mitotic apparatus is established at nuclear envelope which does not require a typical MT organizing center found in animal, centrosome (Hashimoto, 2015). Contrary to MTs emerging from the centrosome in animal cells, most of plant MTs at interphase nucleate from the existed MTs and form parallel patterns in the cortex. (Lloyd and Chan, 2004; Hashimoto, 2015). These cortical MTs are physically linked to the plasma membrane for delivering enzymes that catalyze the synthesis and remodeling of the cell wall (Hashimoto, 2015). Despite the drastically different organizations of MTs, it is generally believed that the MT system in diverse organisms operates with the same principles.

Emerging evidence suggests that stress responses diverge as well. Aside from the cold lability (Melki *et al.*, 1989), the MT system at interphase in animal cells is

considered tightly controlled (Lieuvin, 1994). In contrast, a variety of biotic and abiotic stresses perturb MTs in plant cells (Zhang *et al.*, 2012; Hardham, 2013; Hepler, 2015; Oda, 2015). Studies of Arabidopsis demonstrate that plants tolerate salinity stress by reorganization, depolymerizing, or stabilizing cortical MTs, signaled through the salt overly sensitive (SOS) pathway and phospholipase D pathway (Wang *et al.*, 2011b; Zhang *et al.*, 2012).

A multitude of challenges hinder the elucidation of these salt responses in space and time. Different parts of higher plants, such as roots, stems and leaves are exposed to water and salt differently, and may have distinct abilities in regulating water and salt permeability. In addition, chloroplast emits intense light (Lang *et al.*, 1991; Rasala *et al.*, 2013) under fluorescence microscopy which limits the application of fluorescent proteins that are commonly used to report the dynamic properties of the MT system in real time in animal cells. Exactly how salt is sensed and activates these pathways remain to be resolved.

1.3 *Chlamydomonas* Microtubule System

I reason that *Chlamydomonas* (**Figure 1.2**) is suitable for identifying the similarities and distinctions of the MT system in both animal and plant cells, if the obstacle of autofluorescence is addressed. Its MTOC at interphase consists of four basal bodies (BBs, synonymous to centrioles in non-ciliated cells) that nucleate the axoneme in flagella common among animal cells and organize rootlet microtubule bundles and cortical MTs in the cell body that are unique to plant cells (Harris, 2001; Umen, 2014). Intriguingly, the MT system in *Chlamydomonas* appears to rapidly respond to a number

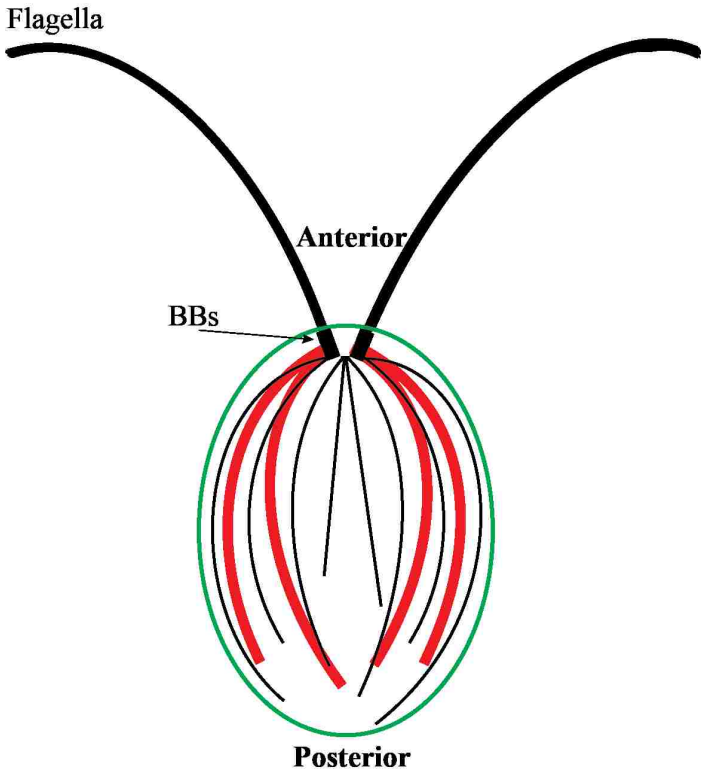

Figure 1.2. A schematic picture depicting flagella and the MT network in the cell body. Black rectangles, basal bodies (BBs). Thick red lines, four stable rootlet microtubule bundles. Thin black lines in the cell body, the dynamic cortical MTs.

of environmental stimuli. For example, organic acids, such as acetic acid and benzoic acid, can trigger axoneme severing within seconds (Lohret *et al.*, 1998; Wheeler *et al.*, 2007) and changes in cortical MT within 5 minutes as revealed by immunofluorescence (Wang *et al.*, 2011b).

Notably, immunofluorescence revealed an unexpected pattern of the master plus end - tracking protein EB1 (**Figure 1.3**). Typically, EB1 homodimer preferentially binds to the plus end of a growing microtubule. As such, fluorescent EB1 is known to exhibit a

comet pattern, and has been commonly used to report the dynamics of growing MTs in live cells (Kumar and Wittmann, 2012). Yet in fixed *Chlamydomonas* cells EB1 was only visible at MT plus-ends at flagella tips and BBs without revealing the cortical MTs (Pedersen *et al.*, 2003), suggesting that algal cortical MTs depolymerized during fixation. These observations pose a number of interesting questions. Does EB1 pass through the gated flagellar entrance and reach the plus-end at the flagellar tip distal to the cell body by IFT or novel trafficking modalities? How does pH shock that severs flagella change the MT dynamics in real time? And how do MTs reassemble in the cell body and flagella after pH is restored?

1.4 Challenges of Live Fluorescent Imaging in *Chlamydomonas*

While live cell imaging using EB1 tagged with a fluorescent protein (FP) as a reporter is ideal to investigate the dynamics of algal MT system in *Chlamydomonas* with higher spatial and temporal resolutions, autofluorescence from photosynthetic pigments in chloroplast (Lang *et al.*, 1991) has hindered the use of fluorescent protein as a reporter. For example, the absorption spectra of chlorophyll a, b, and carotenoid (Grossman *et al.*, 2004) span the entire visible light wavelength range (350 - 680 nm) with absorption peaks between 400 – 480 nm and 625 – 700 nm (Ustin *et al.*, 2009). The emission spectra of chlorophyll a and b range from 600 – 750 nm with peaks at 640 - 680 nm (Welschmeyer, 1994), while carotenoid emits light of 500 - 800 nm with two peaks between 540 – 600 nm and 650 – 700 nm (Kleinegris *et al.*, 2010). Other chromophores contribute to the autofluorescence of the blue-green spectra (Rasala *et al.*, 2013). In order to reveal signals above the autofluorescence of such a wide spectrum it is necessary to

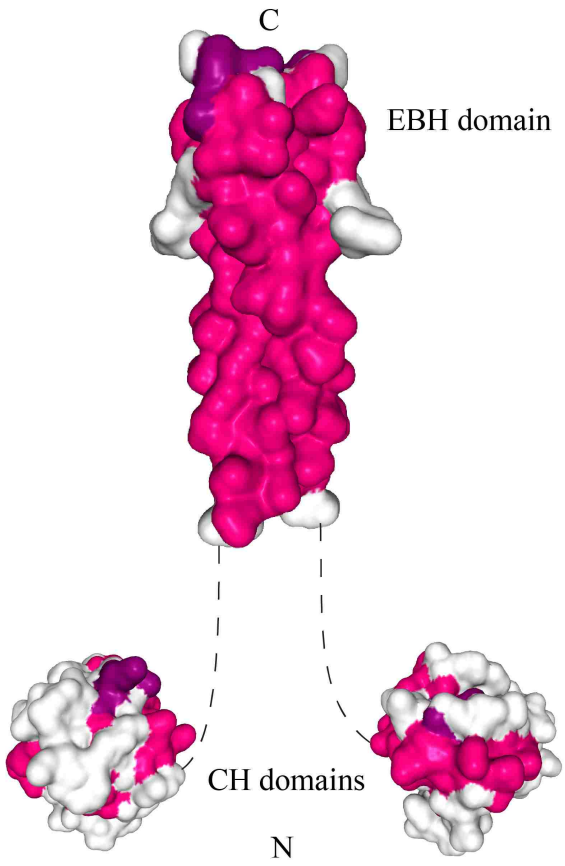

Figure 1.3. Structure view of EB1. EB1 is a homo dimer with two C-terminal coiled coil motifs dimerized into a EB homology (EBH) domain that functions to bind other MAPs. Meanwhile, its two N-terminal caponin homology (CH) domains interacts with MT for plus-end tracking. The structures of EBH domain (PDB entry: 1WU9) and CH domains (PDB entry: 1PA7) are shown in surface views with secondary structure helixes designated in pink and purple. Dashed lines represent uncharacterized EB1 linker regions. The amine and carboxyl ends of EB1 polypeptide are labelled by letters N and C respectively. Structures are generated by NGL web 3D viewer (Rose and Hildebrand, 2015; Rose *et al.*, 2016).

consider spectra, intensity and abundance of fluorophores and the filter sets of the microscope concomitantly. Addressing the autofluorescence from photosynthetic

pigments will allow researchers to take full advantage of the modern tools in imaging to answer questions that would not otherwise be possible in this model system.

1.5 Tools for Live Fluorescent Image analysis

With the invention of a wide array of advanced light microscope systems and fluorophores imaging has become a major approach for discoveries and testing hypotheses in biomedical sciences. In conjunction with the development of computer programs and quantitative image analysis, scientists now are capable of extracting hidden information from each pixel and reach resolutions beyond the diffraction limit of light, enabling visualization and quantification of reactions at the single molecule level. Based on quantitative data, models can be established and equations can be formulated.

Typically, two types of microscopic data are quantifiable - location and intensity in space and time. While these parameters convey critical information, especially for dynamic processes like MT-supported trafficking, it is challenging to quantify absolute light intensity for a number of reasons. For example, emission intensity of fluorophores can be readily affected by various factors (Shaner *et al.*, 2005; Seward and Bagshaw, 2009), such as the intensity and spectra of excitation illumination, photobeaching, autofluorescence, pH, and salinity. Thus, it is difficult to compare intensity information among independent experiments directly unless a reliable intensity standard is present. While several fluorescent reagents and biological complexes, such as quantum dots (Michalet *et al.*, 2005), DNA-origami (Schmied *et al.*, 2014), bacteria flagellar motor, and virus-like particles (Verdaasdonk *et al.*, 2014) can be used as intensity standards, the

standard for day-to-day regular fluorescent microscopy - akin to protein markers or a DNA ladders for electrophoresis -remains elusive.

Suitable intensity standards should meet several criteria. Intensity standards should have stable composition with known fluorescent molecule numbers. Furthermore, the intensity of standards and objects should be within the linear range and the dimension should be similar. Third, the optical properties of the fluorophore should be similar, if not identical. I reason that the MT-based nanomachine in *Chlamydomonas* flagella could be converted into such standards.

Each flagellum is typically 12 μm, physically supported by the axoneme, a MT-based structural scaffold comprised of thousands of 96-nm repeats, each containing a number of axonemal complexes located at particular locations like a molecular ruler (Heuser *et al.*, 2012; Bower *et al.*, 2013). The combined experimental advantages of *Chlamydomonas* have been leveraged to reveal the locations and functions of a number of axonemal complexes. I envisage that a well-characterized protein of known stoichiometry in an axonemal complex distributed periodically throughout flagella could be used as a carrier of fluorescent proteins. Flagella harboring such fusion proteins could become biocompatible fluorescent intensity standards. Transgenic *Chlamydomonas* cells generating such flagella can be easily grown in large quantities at a low cost and flagella can be purified with a straightforward fractionation procedure. Thus, fluorescent flagella potentially can become economical easy-to-apply quantification tools for every day fluorescence microscopy.

1.6 Objectives of the Research

Objective 1: Generate transgenic *Chlamydomonas* strains for live cell imaging of the MT system in flagella as well as in the cytosol.

To investigate the dynamics of the MT system in *Chlamydomonas* and to leverage the ruler-like MT scaffold in its flagella, I generated transgenic strains expressing fluorescent fusion proteins. Chapter 2 describes the materials and methods used to generate these tools for this dissertation and future studies.

Objective 2: Discoveries of swift changes of cortical MT dynamics in real-time in *Chlamydomonas* cells under various stresses.

Using these new tools, bias diffusion of EB1-FPs to the tip of *Chlamydomonas* flagella was imaged in real time (Harris *et al.*, 2015). The tools also allowed us to reveal new phenomena previously obscured by autofluorescence in the cell body. Chapter 3 describes unexpected changes of the MT system elicited by lowering pH and increasing Na^+, and their broad implications.

Objective 3: Develop fluorescent intensity standards using transgenic *Chlamydomonas* flagella.

Radial spoke protein (RSP) 3 is a well-defined protein in the radial spoke (RS) complex along the axoneme of motile cilia and flagella. Chapter 4 describes the conception and application of fluorescent flagella containing fusion RSP3 as a fluorescent protein carrier as intensity standards

The experimental strategies, discoveries, and inventions made in this dissertation will have direct impacts on the plant sciences and the MT field. In addition, this study illuminates new ramification associated with the accelerated climate changes and drought. The contributions and future directions of this work will be discussed in Chapter 5.

CHAPTER 2: MATERIALS AND METHODS

The strains, the procedures used in molecular biology, cell biology and biochemistry methods, fluorescence microscopy, and data analysis are summarized in this chapter.

2.1 Molecular Biology

2.1.1 Engineering of *Chlamydomonas* EB1 (CrEB1) Constructs

A 6-kB CrEB1 genomic DNA, including 1.2 and 1.7-kb 5' and 3' flanking sequence, was amplified by colony-PCR using a *Chlamydomonas* BAC clone as a template and the primers (gcacacggtctagattcgcactgccgtgagc) and (gtctagaccaggcatcggaagtggcttcggagcc) that contained an underlined XbaI site. The PCR fragment digested with XbaI was ligated into the complementary SpeI site in the pGEM-T Easy vector with a paromomycin (PMM)-resistant cassette to create the pCrEB1 for single plasmid transformation (Zhu *et al.*, 2013).

To tag the C-terminus of CrEB1, a 2.8-kB 3' CrEB1 genomic DNA was amplified from the BAC clone using the primer pair (gcaagaccggtgacatgaagcacagcg) and (ccagagcgactgacccaggcatcg) and TA-cloned into pGEM-T vector (Promega). A QuikChange Site-Directed mutagenesis strategy (Stratagene) was used to convert the sequence before the stop codon into an XhoI site for the insertion of a *Chlamydomonas* GFP (CrGFP)-coding fragment derived from pKL3-GFP (Lechtreck *et al.*, 2009) or of a 3HA6His-coding DNA released from pRSP3-HAHis (Gupta *et al.*, 2012). The tagged 3'

genomic DNA was re-amplified to add a KpnI site through an antisense primer (taggtaccccagagcgactgacccaggc). The PCR fragment, digested with KpnI, replaced the 3'untagged fragment in the pCrEB1 to create the pCrEB1-CrGFP and pCrEB1-HAHis.

For expressing NeonGreen (NG)-tagged protein, a plasmid pBR25-CrNG containing NeonGreen DNA was custom synthesized based on mNeonGreen protein sequence (Shaner *et al.*, 2013) and *Chlamydomonas* codon bias. The NG DNA was amplified using the primer pair (ctcgagatggtgtccaagg) and (ctcgagcttgtacagctcgtcc) with an added XhoI site. Then, the NG DNA was cloned into a pBlueScprit vector to build pNG. The XhoI-digested NG fragment from the pNG replaced the GFP fragment in the pCrEB1-CrGFP to create pCrEB1-NG.

In a similar manner, the mCherry DNA was amplified with added flanking XhoI sites from an mCherry-tubulin vector (kindly provided by Dr. Karl Lechtreck at University of Georgia) derived from pRS306-mCherry-TUB1 (Khmelinskii *et al.*, 2009). The XhoI-cut mCherry DNA was used to replace CrGFP fragment in the pCrEB-CrGFP to generate pCrEB1-mCherry.

2.1.2 Engineering of *Chlamydomonas* RSP3 Constructs

To express RSP3-NG and RSP3-CrGFP, the HAHis DNA in plasmid pRSP3-HAHis (Gupta *et al.*, 2012) was replaced with the NG and CrGFP DNA to generate pRSP3-NG and pRSP3-CrGFP respectively. To generate the construct expressing $RSP3_{1\text{-}316}$-CrGFP, CrGFP DNA was inserted into XbaI-digested $pRSP3_{1\text{-}316}$ (Sivadas *et al.*, 2012) to create $pRSP3_{1\text{-}316}$-CrGFP. To add NG and HAHis triple tags, the 3HA12His DNA was deleted from pRSP3-HAHis by XhoI and XbaI. The resulting fragment was ligated with the NG

DNA released from pNG (**see 2.1.1**) by XhoI/BamHI double digest and the 3HA12His DNA released from p3HA12His by BamH1/XbaI double digest to generate pRSP3-NG-HAHis.

2.2 Cell Biology

2.2.1 Cell Culture

The *Chlamydomonas* strains used in this dissertation (**Table 2.1**) were acquired from *Chlamydomonas* Resource Center (http://www.chlamycollection.org/). For liquid cultures, *Chlamydomonas* cells were grown in 300 ml pH 7.0 standard tris/acetate/phosphate (TAP) liquid media (Gorman and Levine, 1965) with aeration at 25°C over a 14/10 light/dark cycle until reaching logarithmic phase of growth (5 -10 X 10^6 cells/ml). For agar cultures, cells were grown on 1.5% agar plates made with TAP media.

2.2.2 Generation of *Chlamydomonas* Strains

Double mutant strains were generated using classic *Chlamydomonas* genetics. Briefly, cells from each single mutant were grown on TAP plate cultures for 1 week to induce gametogenesis. After incubation in nitrogen-minus TAP media for ~ 5 hours, equal amounts of gametes of opposite mating types were mixed together. The mixture was placed under constant light for ~2 hours to allow mating. Cell pellets were then plated on TAP plates. Following 18 hours under constant light, the plates were wrapped in aluminum foil for 5 – 7 days. Tetrad dissection and genetic analysis were performed afterwards (Jiang and Stern, 2009).

All transgenic strains (**Table 2.1**) were generated using the glass beads method (Kindle, 1990). After vortex with glass beads in the presence of plasmids

Table 2.1. List of *Chlamydomonas* transgenic and double mutant strains.

Double Mutant	**Parental Strain**	**Plasmid**	**Selection Marker**	**Tag**
Pf5pf14 (crossing)	CC-1028 *pf5*; CC-613 *pf14* (RSP3 mutants)			
Pf17pf14 (crossing)	CC-1035 *pf17* (spoke-head-less muatant); CC-613 *pf14*			
Pf18pf14 (crossing)	CC-1036 *pf18* (central pair mutant); CC-613 *pf14*			
Transgenic Strain	**Parental Strain**	**Plasmid**	**Selection Marker**	**Tag**
*Armc*2 NDK5-NG-HAHis	LMJ.RY0402.155726 (CLiP mutant)	pNDK5-NG-HAHis	Hyg	NG; 3HA6His
*Armc*2 ARMC2	LMJ.RY0402.155726	pARMC2	Hyg	
*Armc*2 ARMC2-mCherry	LMJ.RY0402.155726	pARMC2-mCherry	Hyg	mCherry
Bld10-EB1-NG	CC-4076 (basal bodies mutant)	pCrEB1-NG	PMM	NG
CC-124 EB1-NG	CC-124 Wild type (WT)	pCrEB1-NG	PMM	NG
CC-124 EB1-mCherry	CC-124 WT	pCrEB1-NG	PMM	mCherry
CC-125 EB1-CrGFP	CC-125 WT	pCrEB1-CrGFP	PMM	CrGFP
CC-620 tubulin-GFP+EB-mCherry	CC-620 tubulin-GFP (kindly provided by Dr. Karl Lechtreck)	pCrEB1-mCherry	PMM	mCherry
Dhc1b EB1-CrGFP	CC-4423 *dhc1b-3* (dynein heavy chain mutant)	pCrEB1-NG	PMM	CrGFP
Dhc1b EB1-NG	CC-4423 *dhc1b-3*	pCrEB1-NG	PMM	NG
Eyeless EB1-NG	CC-4307 *min1 eye2* (eyeless mutant)	pCrEB1-NG	PMM	NG
Fla10 EB1-HAHis	CC-1919 *fla10-1* (kinesin mutant)	pCrEB1-HAHis	PMM	3HA6His
Fla10 EB1-CrGFP	CC-1919 *fla10-1*	pCrEB1-CrGFP	PMM	CrGFP
Fla10 EB1-NG	CC-1919 *fla10-1*	pCrEB1-NG	PMM	NG
Fla11 EB1-CrGFP	CC-1920 *fla11* (IFT172 mutant)	pCrEB1-CrGFP	PMM	CrGFP
Fla11 EB1-NG	CC-1920 *fla11*	pCrEB1-NG	PMM	NG
Lf1 $RSP3_{1-316}$-CrGFP	*Lf1* (CDK-related kinase mutant)	$pRSP3_{1-316}$-CrGFP	PMM	CrGFP
Lf4 IFT20-mCherry+EB1-CrGFP	CC-4535 *lf4* (long-flagella mutant)	pCrEB1-CrGFP;	PMM	CrGFP; mCherry

		pKL3-IFT20-mCherry (Lechtreck et al., 2009)		
Pf5 RSP3$_{1-316}$-CrGFP	CC-1028 *pf5*	pRSP3$_{1-316}$-CRGFP	PMM	CrGFP
Pf5pf14 RSP3-CrGFP	*Pf5pf14* (crossing)	pRSP3-CrGFP	PMM	CrGFP
Pf5pf14 RSP3-NG	*Pf5pf14* (crossing)	pRSP3-NG	PMM	NG
Pf14 RSP3$_{1-316}$-CrGFP	CC-1032 *pf14* (RSP3 mutant)	pRSP3$_{1-316}$-CrGFP	PMM	CrGFP
Pf14 RSP3$_{1-316}$-CrGFP TtoA double	CC-1032 *pf14*	pRSP3$_{1-316}$-CrGFP T87A&T130A	PMM	CrGFP
Pf14 RSP3-CrGFP	CC-613; CC1032	pRSP3-CRGFP	PMM	CrGFP
Pf14 RSP3-CrGFP TtoA double	CC-1032 *pf14*	pRSP3-CrGFP T87A&T130A	PMM	CrGFP
Pf14 RSP3-HAHis	CC-1032 *pf14*	pRSP3-HAHis	PMM	3HA12His
Pf14 RSP3-HAHis TtoA double	CC-1032 *pf14*	pRSP3-HAHis T87A&T130A	PMM	3HA12His
Pf14 RSP3-NG	CC-613 *pf14*	pRSP3-NG	PMM	NG
Pf14 RSP3-NG-HAHis	CC-613 *pf14*	pRSP3-NG-HAHis	PMM	NG; 3HA6His
Pf14 EB1-NG	CC-613	pCrEB1-NG	PMM	NG
Pf18 EB1-CrGFP	CC-1036 *pf18*	pCrEB1-CrGFP	PMM	CrGFP
Pf18 EB1-NG	CC-1036 *Pf18*	pCrEB1-NG	PMM	NG
Pf19 EB1-NG	CC-1037 *pf19* (katanin mutant)	pCrEB1-NG	PMM	NG
Pf27 RSP3$_{1-316}$-CrGFP	CC-1387 *pf27*	pRSP3$_{1-316}$-CrGFP	PMM	CrGFP
Pf27 NDK5-NG-HAHis	CC-1387 *pf27*	pNDK5-NG-HAHis	Hyg	NG; 3HA6His
Pf27 ARMC2	CC-1387 *pf27*	pARMC2	Hyg	
Pf27 ARMC2-NG-HAHis	CC-1387 *pf27*	pARMC2-NG-HAHis	Hyg	NG; HAHis
Pf27 ARMC2-mCherry	CC-1387 *pf27*	pARMC2-mCherry	Hyg	mCherry
Tub2-1 EB1-NG	CC-2681 colR4 22a (β-tubulin mutant)	pCrEB1-NG	PMM	NG

(Sivadas *et al.*, 2012), cells were plated on TAP plates containing 10 μg/ml PMM or Hygromycin (Hgy). The antibiotic-resistant clones were resuspended in double distilled water (ddw) or 10 mM HEPES and screened for motility or fluorescence using a Nikon Eclipse wide field microscope and a CoolSNAP-ES CCD camera.

2.2.3 Solutions

Glacial acetic acid (HA) was diluted with ddw to various concentrations ranging from 5 to 1000 mM as specified in the text. The 10 mM HCl solution was titrated to pH 3 with 1

M NaOH. The 1000 mM HA was added to the TAP medium to make 20 mM pH 4.5 HA/TAP. For 5 mM Na^+ /HEPES and K^+/HEPES, pH of 10 mM HEPES was adjusted to 7.4 with NaOH or KOH respectively. To make 21 mM Na^+/EGTA and K^+/EGTA solutions, 10 mM EGTA was titrated to pH 8 with NaOH or KOH. The 5 mM NaCl and KCl solutions were made by dissolving the respective salt in ddw. The 5, 55, and 150 mM Na^+/HEPES solutions were made by adding NaCl into 5 mM pH 7.4 Na^+/HEPES. The solutions containing 30 or 75 mM Ca^{2+} were made by dissolving $CaCl_2$ in 5 mM pH 7.4 Na^+/HEPES.

2.3 Western Blots

Flagella were isolated as described (Yang *et al.*, 2009). For whole cell samples, the cell pellet from a 5-ml late log phase TAP liquid culture was resuspended with 50 μl HEPES buffer, followed by the addition of 100-μl 5 X SDS-PAGE sample buffer and boiling for 5 min. After the addition of 2 μl of 1.7 mg/ml PMSF, vortex and centrifugation, the supernatants were fractionated in a 9% SDS-PAGE gel and the blot was probed with polyclonal anti-EB1 (Pedersen *et al.*, 2003), monoclonal anti-IC1 (King and Witman, 1990) or monoclonal anti-α-tubulin (Sigma). Following incubation with horseradish peroxidase-conjugated secondary antibodies, the signals revealed by enhanced chemiluminiscence were captured by UVP Autochemi Bioimaging System (Cambridge, UK).

2.4 Fluorescence Microscopy

Fluorescence images were acquired with Nikon Eclipse widefield microscope

equipped with a short-arc mercury lamp, a FITC-HYQ optical filter set (Excitation 460 nm – 500 nm; Emission 510 nm – 560 nm) for CrGFP, EGFP and NG, a modified Texas Red optical filter set (Excitation 532 nm – 587 nm; Emission 595 nm – 635 nm) for mCherry, a CoolSNAP-ES CCD camera and a MetaMorph software.

2.4.1 Imaging EB1-FPs in Live *Chlamydomonas*

Each EB1-FP image was captured at 1-second exposure and saved as a 16-bit grayscale file. Streaming videos were recorded for 100 frames at a rate of 1 frame/second and played at a 16 frames/second frame rate.

Typically, cells were resuspended in solutions for 5 minutes unless indicated otherwise. An aliquot of 5 μl cell suspension was placed on a slide and then covered by an 18 X 18-mm cover slip. The edges were sealed with nail polish before imaging. To reveal the effect of compression, a 3-μl aliquot of cell suspension was placed on a glass slide and then covered with a 22 X 22-mm cover slip. Cells became gradually compressed by the coverslip as evident by flattened cell body. For pH pulse in a perfusion chamber, an aliquot of 10 μl of cells in the TAP medium was placed on a cover slip pre-coated with 5 μl 0.001% poly-L-lysine. The cover slip was then inverted to assemble a perfusion chamber as shown in **Figure 3.2a**. The chamber was flushed with 200 μl of 20 mM pH 4.5 HA/TAP. Subsequently, HA/TAP was replaced by a flush of 200 μl TAP. The entire process was recorded in two consecutive live-stream clips. For this long recording duration, excitation light intensity was reduced to 25% with a neutral density filter. For HA pulse in a diffusion chamber, 40 μl of cells in 5 mM pH 7.4 Na^+/HEPES was placed at one side of a diffusion chamber underneath a 40X objective

lens (**Figure 3.2a**). A live-streaming video was recorded following the injection of 20 μl of 100 mM pH 2.8 HA through the Vaseline wall to the opposite side of the chamber. For the HA bath, a cell pellet from 500 μl liquid culture was resuspended in 50 μl of 10 mM pH 3 HA. A 10 μl aliquot of cell mixture was placed on a cover slip. The cell-loaded cover slip was inverted to create a perfusion chamber. After a total 5-minute exposure to HA, HA was flushed away with a 200 μl aliquot of indicated fluid and then a video was recorded. To test MT cold lability after recovery from HA bath, a perfusion chamber with treated cells was chilled by ice for 3 minutes. A video was taken immediately afterwards, ~20 seconds after the chamber was removed from ice.

2.4.2 Imaging Flagella Standards

Chlamydomonas cells in a 5-μl suspension were imaged. Cells oriented in the side view were selectively imaged to reveal entire flagella. With this limited volume, the coverslip prevented cells from swimming. For top views, 30-50 μl of cells were placed in a chamber slide, allowing cells to swim toward light from the microscope and become immobilized as flagella attached to the coverslip. Purified flagella were placed on glass slides directly or slides coated with 0.01% poly-L-lysine. After air drying and rehydration in the HEPES buffer, coverslips with flagella were inverted on a glass slide. Inverted coverslips were moved manually back-and-forth to splay axonemes mechanically. To image yeast cells with flagella, 0.5 μl of ~2×10^5 flagella/μl 10 mM HEPES were applied to a coated slide, air dried and then rehydrated prior to the application of yeast cells resuspended in the same buffer.

For methanol fixation, poly-L-lysine-coated slides with attached flagella were submerged to a methanol jar in a -20°C freezer for 10 min. The treated slide was then air dried and washed 3 times with the 10 mM HEPES buffer prior to imaging. For imaging fixed and unfixed samples together, unfixed flagella were added to the rehydrated methanol-treated slide prior to imaging.

2.5 Data Analysis

2.5.1 Quantifications of EB1-NG in *Chlamydomonas*

To measure EB1 comet speed, a 40-second sub-stack containing side views of immobilized cells were first made by the open source image processing software, ImageJ (https://imagej.nih.gov/ij/index.html); and individual comets were analyzed with a Matlab-based particle tracking software, plusTipTracker (Applegate *et al.*, 2011). In each cell that maintained completely quiescent for the tracking period, all tractable comets which transverse at least one third of the cell length were analyzed. The numbers of qualified cells and comets from numerous recordings were indicated. To generate line scans of EB1 intensity at microtubule plus ends, a line tool in ImageJ was used to measure gray values along the length of comets. Relative fluorescence intensity was normalized after subtracting a background gray value measured next to the comet with the line tool. Histograms were generated with the Microsoft program, Excel. Kymographs were generated with an ImageJ plug-in multiple kymograph (https://www.embl.de/eamnet/html/body_kymograph.html). All data are given as mean ± SEM (standard error of the mean) and analyzed with Sigmaplot 13.0 (Systat Software, Inc., San Jose, CA).

2.5.2 Quantifications of Flagellar Standards

ImageJ was used to quantify background-subtracted 16-bits fluorescence images. The Plot Profile function was used to measure the intensity of pixels along a straight line across a region of interest (ROI). The boundary of ROI was defined by the Triangle method and the area and mean intensity (total intensity/area) were measured. The resulting histograms were generated with Excel. All data are given as mean ± SEM and analyzed with Sigmaplot 13.0. In theory, the total intensity captured by the camera from all fluorescence molecules in each ROI can be expressed as a general equation

$$B_{FM} \times N_{FM} = \overline{I_{FM}} \times A_{FM} \quad (1)$$

with B_{FM}, the brightness of light emitted from one fluorescence molecule; N_{FM}, the number of fluorescence molecules; $\overline{I_{FM}}$ and A_{FM}, measured mean intensity and the area of a ROI. For the standard of a 2-μm flagellar segment with 720 RSP3-NG molecules, Equation (1) could be converted into

$$B_{NG} \times 720 = \overline{I_{NG}} \times A_{NG} \quad (2)$$

Equation (1) and (2) could be combined into

$$N_{FM} = 720 \times \frac{B_{NG}}{B_{FM}} \times \frac{A_{FM} \times \overline{I_{FM}}}{A_{NG} \times \overline{I_{NG}}} \quad (3)$$

Using Equation (3), N_{FM} in a ROI can be derived from the ratio between the measured $A_{FM} \cdot \overline{I_{FM}}$ of the ROI and $A_{NG} \cdot \overline{I_{NG}}$ of the intensity standard, and the known ratio of brightness ($\frac{B_{NG}}{B_{FM}}$) between one NG and one fluorescence molecule– either NG or CrGFP in this study.

CHAPTER 3: H^+- AND NA^+-ELICITED SWIFT CHANGES OF MT SYSTEM IN BIFLAGELLATED GREEN ALGA *CHLAMYDOMONAS*

3.1 Introduction

The microtubule (MT) cytoskeletal system is integral to many crucial processes in eukaryotic cells. The opposing ends of these cylindrical polymers exhibit distinct properties, with the plus end growing and shrinking stochastically and the minus captured by centrosomes. MTs establish the polarity of cells and serve as tracks for positioning and trafficking intracellular components. They can also form complex machineries. One example is the mitotic apparatus enabling accurate segregation of chromosomes during mitosis and meiosis. These actions require harnessing MT dynamic instability and the involvement of a wide array of accessory proteins and various post-translational modifications (Hashimoto, 2015; Song and Brady, 2015). Not surprisingly, MTs are the target of natural toxins, such as Taxol (Weaver, 2014), and a number of herbicides (Hashimoto, 2015). Notably, biotic and abiotic stresses alter plant MTs, while Taxol exacerbates stress-induced maldevelopment of seedlings (Wang *et al.*, 2011a; Hardham, 2013; Hepler, 2015; Oda, 2015). Yet the mechanisms underlying stress-induced changes of MTs and the broad implications remain elusive.

Chlamydomonas reinhardtii is uniquely suited for addressing these issues. The unicellular fresh water green alga has signature features of both animal and plant cells

(Merchant *et al.*, 2007). Like animal cells, it has motile flagella that contain stable MT bundles. Like typical plant cells, the alga is equipped with vacuoles, chloroplast, and dynamic cortical MTs that serve as tracks for the delivery of the enzymes which synthesize the cell wall (Paredez, 2006). Curiously, its MT system appears susceptible to environmental changes. Its flagella sever readily when the aqueous environment changes suddenly (Lefebvre, 1978; Quarmby, 2009). The best characterized stimulus is pH shock. Organic acid, such as acetic acid (HA) diffuses across the plasma membrane and then becomes ionized. The resulting acidification in the cytosol triggers nearly simultaneous influx of extracellular Ca^{2+}, which signals flagella amputation (Quarmby, 1996; Wheeler *et al.*, 2007; Hilton *et al.*, 2016). Cortical MTs become fewer and shorter, detected by immunofluorescence and biochemistry, 5 minutes after pH shock (Wang *et al.*, 2013).

While live cell imaging will be ideal for revealing these acid-induced responses with higher spatial and temporal resolution, autofluorescence from photosynthetic pigments in chloroplast obscures commonly used fluorescent reporters (Lang *et al.*, 1991; Rasala *et al.*, 2013). Recently, I succeeded in revealing dynamic cortical MTs by taking advantage of the new fluorescent protein, NeonGreen (NG) that is 2.7 X brighter than EGFP (Shaner *et al.*, 2013), and the relative abundant plus end-binding protein, EB1, as the NG carrier (Harris *et al.*, 2015).

EB1 plays central roles in eukaryotes (Su *et al.*, 1995; Akhmanova and Steinmetz, 2010; Kumar and Wittmann, 2012). Its N-terminal domain preferentially binds to the lattice among tubulins at the plus end of MTs, whereas its C-terminal domain can associate with a wide array of proteins. The two domains operate in concert to accelerate MT dynamics (Rogers *et al.*, 2002; Vitre *et al.*, 2008; Maurer *et al.*, 2014) and recruit

various +TIP effector proteins that function at the plus end. In live cell imaging, fluorescent EB1 exhibits a comet pattern seemingly leading the plus end of nascent growing MTs, where tubulins transition from the GTP state to the GDP state (Zanic *et al.*, 2009; Maurer *et al.*, 2012; Gardner *et al.*, 2013). Thus, fluorescent EB1 has been commonly used to report newly generated growing MTs (Piehl *et al.*, 2004; Matov *et al.*, 2010). However, increased binding to the GDP zone occurs in a number of scenarios, such as overexpression of the EB1, perturbation of the tubulin GTP hydrolysis or disruption of the function of EB2 protein (Tirnauer, 2002; Goldspink *et al.*, 2013; Tortosa *et al.*, 2013; Sayas and Avila, 2014). The cause of the switch from plus tip to GDP zone remains uncertain.

Using EB1-NG as a reporter, I captured in real time unexpected changes in EB1-NG patterns and MT dynamics signaled through H^+ and Na^+. The remarkable sensitivity and the distinct responses in WT cells and mutants shed critical insight on the divergence of the MT system, pH regulated processes and the vulnerability of organisms subjected to environmental stresses.

3.2 Results

3.2.1 EB1-NG Reports Remarkable Sensitivity of the MT System in *Chlamydomonas*

The MTOC in *Chlamydomonas* cells at interphase is comprised of two pairs of basal bodies (BBs) (**Figure 3.1a, top panel**). The mother BB nucleates the assembly of the axoneme, a MT-based scaffold that drives the rhythmic beating of the flagellum. Four rootlet MT bundles (**thick lines**) arrange in a cruciate pattern with BBs at the apical end and the other organelles toward the basal (Mittelmeier *et al.*, 2011; Picariello *et al.*, 2014). These MT bundles consist of more than two acetylated stable MTs. In contrast, cortical MTs (**thin lines**) are singular (Horst *et al.*, 1999) and highly dynamic (Harris *et al.*, 2015). Under widefield fluorescence microscopy EB1-NG expressed at the level of endogenous EB1 from a genomic construct does not reveal stable MTs except the flagellar tip where plus ends of axonemal MTs undergo turnover continuously (Harris *et al.*, 2015). In addition, plus ends of growing cortical MTs appear like the typical comets observed in other eukaryotic cells. Comets emerged from four spots underneath flagella, corresponding to BBs (**Figure 3.1a, bottom panel**) (Pedersen *et al.*, 2003). As shown from the top, side and rear views of cells, comets of nascent cortical MTs travel along the contour of the cell body toward the posterior pole (**Figure 3.1b, white arrowhead**). Near the pole comets vanish presumably when MTs stop growing or switch to the shrinking phase. The pattern appears similar in cells resuspended in the commonly used TAP culture medium or 10 mM HEPES buffer (with 5 mM Na^+).

The birth of new comets from BBs appeared stochastic. I did not measure the birth rates, hindered by substantial fluctuations and the narrow apical area. Instead I

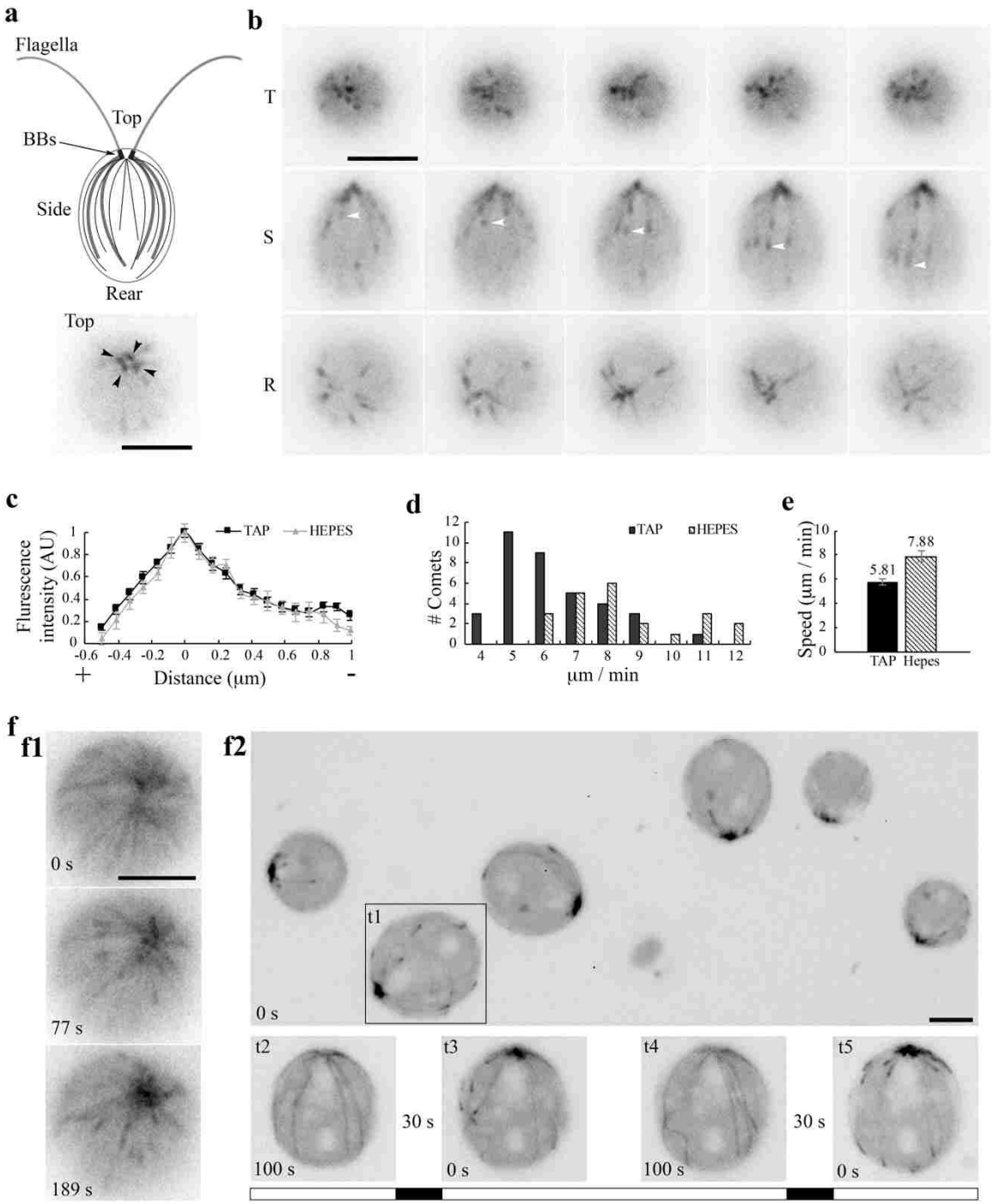

Figure 3.1. EB1 in *Chlamydomonas*. (a) A schematic picture depicting flagella and the MT network in the cell body (top panel). Black dots, basal bodies (BB). Thick lines, four

stable rootlet microtubule bundles. Thin lines in the cell body, the dynamic cortical MTs. A top view of EB1-NG transgenic cells reveal a pattern that resembles 4 BBs (bottom panel). (b) Time-lap fluorescent images were taken 10 seconds apart from the top (T), side (S) and rear (R) of cells resuspended in the TAP culture medium. EB1-NG appeared like typical comets (arrowheads), emerging from the BB area, coursing along the contour of the cell body and then vanishing as approaching the rear end. The frame rate is 1 frame/sec. (c) Normalized line scans along the length of MT plus ends showed a similar EB1 intensity profile in the TAP medium (n = 18 comets from 6 cells) and the Na+/HEPES buffer (n=11 comets from 3 cells). The position with peak intensity was designated as 0. The value was negative toward plus end; positive toward BBs. AU, arbitrary unit of fluorescence intensity. (d) The distribution and (e) the mean and the SEM of EB1 comet speed in the TAP medium (n = 36 comets from 6 cells in 6 recordings) and 5 mM Na+/HEPES buffer (n = 22 comets from 3 cells in 3 recording) are significant different (Mann-Whitney U test, $P < 0.001$). (f) Altered MT patterns during fluorescence microscopy. The EB1 comet pattern occasionally switched to a bird cage pattern (f1). Comets returned while the bird cage receded in ~ 1 min. In flattened cells that were gradually compressed by the cover slip, both MTs and comets became more visible (f2, top panel). Comets disappeared after ~ 100 sec (bottom panel, t2), but returned after illumination was switched off for 30 sec (t3). The process was repeatable after another 100 seconds illumination and then another light off period (t4 and t5). The alternate white and black bars illustrate the scheme of alternate illumination and dark periods. Scale bars, 5 μm.

analyzed comet length and speed from the side view. Line scans along the lengths of comets show the typical feature of EB1 comets - the brightest spot corresponds to the area where tubulins are primarily at the transitional state, slightly behind the leading edge of plus ends with GTP-tubulins (**Figure 3.1c**). The distribution of comet speeds shows that MT growth rates vary nearly two folds (**Figure 3.1d**). The dataset from cells in the TAP medium (**black bars**) skews toward the slow end relative to the Na^+/HEPES dataset (**hatched bars**). The average velocities are significantly different (Mann-Whitney U test, $p < 0.001$), at 5.8 ± 0.26 and 7.9 ± 0.42 μm/sec respectively (**Figure 3.1e**), which are within the normal range measured in diverse eukaryotic cells (Harris *et al.*, 2015).

Curiously, in some long recordings, comets suddenly gave way to a bird cage-like pattern (**Figure 3.1f1, top panel**) in which EB1 bound throughout MTs as if all cortical

MTs were revealed by anti-tubulin immunofluorescence (Horst *et al.*, 1999; Dymek, 2006). Comets returned automatically after ~1 minute (**middle and bottom panels**). This unpredictability suggests that this pattern is caused by fluctuating intracellular conditions. When cells were gradually flattened by the coverslip, MTs also became visible as a broken bird cage with comets (**Figure 3.1f2, top panel, t1**). However, comets disappeared after ~100 seconds (**bottom panel, t2**). Interestingly, after a 30-second dark period, comets returned when the excitation light was switched back on (**t3**). Simply alternating the dark and light period replicated the disappearance and return of comets (**t4–t5**). These observations demonstrate that the *Chlamydomonas* MT system is highly mercurial; and suggests that excitation illumination creates a condition that is unfavorable for MT dynamics, but is reversed in the dark. As illumination opens channelrhodopsins that conduct a number of cations and Cl^- (Nagel *et al.*, 2002; Nagel *et al.*, 2003; Hegemann and Berthold, 2009), I hypothesize that fluctuations of electrolyte concentrations modulate the MT system in *Chlamydomonas*. Considering the light sensitivity, I elected to use wide field microscopy with minimal excitation intensity to test this.

3.2.2 Sequential Changes in the MT System Elicited by a Short HA Pulse and Subsequent Wash

I first used the well-defined pH shock, recording EB1-NG signals in cells exposed to HA in two complementary devices, a perfusion chamber and a diffusion chamber (**Figure 3.2a**). Recording of events in perfusion chambers started immediately before injection. Similar to pH shock, all cells were subjected to a swift change of environments

as the injected solution was immediately pulled across the chamber by filter papers placed at the opposite end (Wheeler *et al.*, 2007). However, the initial period was not decipherable due to flowing of injected fluid and unattached cells. For the diffusion chamber encircled by Vaseline, cells were placed at one side, underneath the coverslip and objective lens (**right panel**). Recording started after 100 mM HA was injected into the opposite side and cells stopped flowing. This design decelerated the acidification process and captured the events as HA diffused across the field and into cells that were being recorded. However, the precise exposure time was uncertain; HA concentrations increased gradually, deflagellation was less effective; and not all cells were acidified to the same degree at the same time. Also, the enclosed chamber cannot be washed.

Following the injection of 20 mM HA/TAP into the perfusion chamber, all comets vanished in the first discernable image taken at ~90 seconds (**Figure 3.2, b1–b2**). After wash with 10 mM pH 7 HEPES, comets re-appeared at the BB area within ~ 45 seconds and MT dynamics resumed (**b3–b5**). Thus, HA exposure elicits the disappearance of EB patterns either by perturbing EB-MT interplays or causing cortical MTs to pause or disassemble. New dynamic MTs re-form rapidly after HA is washed away.

Diffusion chambers in which the acidification process occurs gradually allow us to capture another unexpected phenomenon before comets vanish. A broken bird cage pattern with a few MTs (**Figure 3.2c, left and middle panel, black arrowhead**) and comets (**white arrowheads**) appeared before the disappearance at a time designated as 78 seconds (**right panel**). To decipher the disappearance, I analyzed digitally enhanced recordings (**Figure 3.2d, top panels**). As shown in two representative cells, overall EB1

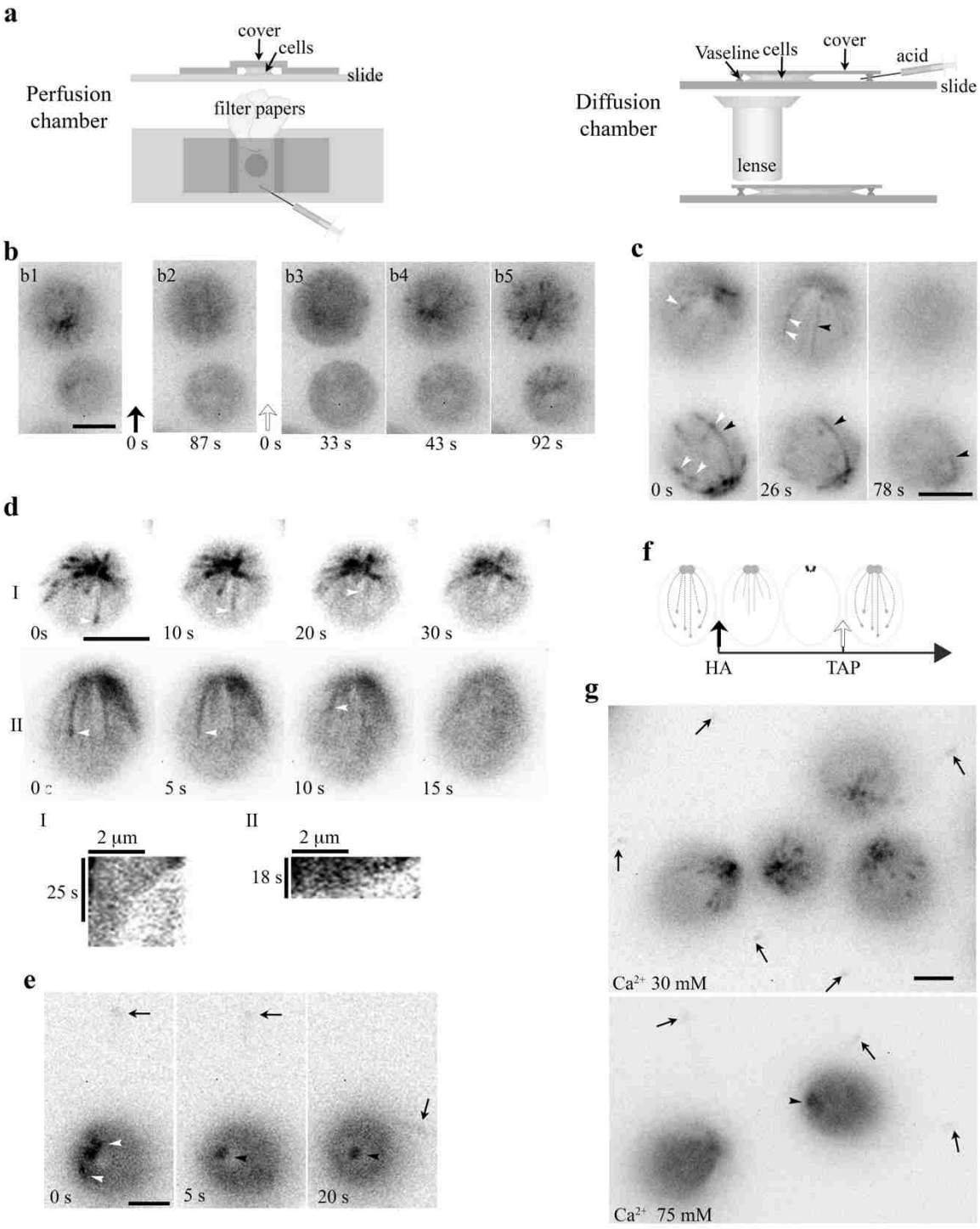
a
Perfusion chamber
cover
cells
slide
filter papers
Diffusion chamber
Vaseline
cells
cover
acid
slide
lense
b
b1
b2
b3
b4
b5
0 s
87 s
0 s
33 s
43 s
92 s
c
0 s
26 s
78 s
d
I
0s
10 s
20 s
30 s
II
0 s
5 s
10 s
15 s
I
2 µm
25 s
II
2 µm
18 s
e
0 s
5 s
20 s
f
HA
TAP
g
Ca2+ 30 mM
Ca2+ 75 mM

Figure 3.2. An HA pulse elicited swift sequential changes in the MT system. (**a**) Schematics depicting an open-ended perfusion chamber (left panels) and a diffusion chamber (right panels) for capturing the HA-induced rapid changes. (**b**) A 10-µl aliquot of cells resuspended in the TAP medium was placed in a perfusion chamber. The images (**b1, 2**) were captured before and after perfusion with 20 mM HA/TAP (pH 4.5, t=0, black arrow). The following recordings (**b3-5**) captured the events right after the TAP medium (pH 7) was injected to wash away HA (t=0, clear arrow). B3 is the first clear image after fluid and cells stopped flowing. Comets already disappeared within 87 seconds after HA perfusion. They started emerging 43 seconds after wash. (**c**) The process preceding HA-induced disappearance of EB1 comets in diffusion chambers. A 40-µl aliquot of cells resuspended in HEPES was placed in a diffusion chamber encircled by Vaseline, under the coverslip and an objective lens. HA was injected to the other side of the chamber and diffused toward cells that were being imaged. During the gradual acidification process, both comets (white arrowheads) and shank binding MTs (black arrowheads) were evident first and then both patterns vanished. (**d**) Time lapse images and kymographs revealed endwise resorption of EB1-decorated MTs (white arrowheads). (**e**) Comets (white arrowheads) in the cell body vanished first before the excision of flagella (arrows). Following deflagellation, EB1 diffused away from the tip. EB1 signals remained at BBs but was static (black arrowhead). (**f**) A schematic depicting sequential changes in MTs upon exposure to HA and a subsequent wash with the TAP medium. Dotted lines with a comet, growing MTs. Dotted lines alone, shrinking MTs. Solid lines, shrinking MTs with EB1 shank binding. (**g**) Effects of $[Ca^{2+}]_{ex}$ on MTs. In cells resuspended in 30 mM $[Ca^{2+}]_{ex}$, flagella remained attached (arrows in left panel), while comets were vibrant. In the 75 mM $[Ca^{2+}]_{ex}$ group, comets disappeared and flagella were amputated (arrows in bottom panel). Static EB1 signals remained at BBs (arrowhead). Scale bars, 5 µm.

signals were fading with time, which could be due to photobleaching, pH sensitivity of fluorescent proteins, disassociation of EB1 or system-wide MT disassembly. Some MTs clearly underwent endwise resorption (**arrowheads**). Kymographs tracking plus ends of prominent MTs in two rare still cells show that, as expected, comets disappeared before the resorption of the respective MT. Measurements of the slopes show that the initial shortening speeds for these two events are 8 and 13 µm/min but decelerate toward the BB area. These speeds revealed by EB1-NG are in line with the averaged 10±3 µm/min shortening speed of cortical MTs in cultured tobacco cells (Dixit, 2004), faster than kinesin-13 catalyzed shortening (Helenius *et al.*, 2006), and slower than the maximal

shortening speed (30 μm/min) of MTs assembled from purified tubulins (O'Brien *et al.*, 1997). Statistics of shortening speed was not analyzed because of few motionless cells and few shortening MTs with a definitive plus end. Tubulin reporters will be more appropriate for shortening analysis.

As for cells with EB1 signals detected in the cell body and flagella (**Figure 3.2e**) simultaneously, comets (**white arrowheads in left panel**) vanished first (**middle panel**) before flagella (**arrow**) were amputated (**right panel**). EB1 signals remained at the BB area but were static (**black arrowhead**). Contrary to deflagellation within seconds upon HA perfusion (Wheeler *et al.*, 2007), the deflagellation in the diffusion chamber takes more than one minute due to gradual acidification. Thus, when cells are exposed to HA, shank binding increases, comets disappear, endwise resorption becomes evident and then flagella become amputated. The sequential events occurring in the diffusion chamber are summarized in **figure 3.2f**.

Lowering intracellular pH elicits Ca^{2+} influx, and Ca^{2+} prevents MT formation and promotes MT disassembly (Weisenberg, 1972; O'Brien *et al.*, 1997). To differentiate whether HA-induced changes are due to H^+ or Ca^{2+}, I raised $[Ca^{2+}]_{in}$ without adding HA. Calcium ionophore A23187 did not trigger deflagellation or evident changes in the MT system in our hands. This is not surprising since A23187 cannot elicit consistent effects in *Chlamydomonas* (Bloodgood and Levin, 1983). So I simply raised $[Ca^{2+}]_{ex}$. Perfusions of either HA or $CaCl_2$ solution elicit Ca^{2+} influx, leading to deflagellation, although the latter is less efficient (Wheeler *et al.*, 2007). WT cells resuspended in 30 mM Ca^{2+}/HEPES appeared restless, suggesting entry of Ca^{2+} (**Figure 3.2g, top panel**). However, flagella remained attached (**arrows**) and comet activity was robust. When cells

were resuspended in 75 mM Ca^{2+}/HEPES solution (**right panel**), cells shed flagella (**arrows**). Comets disappeared, while static EB1 signals remained at the BB area (**arrowhead**). Thus the outcomes elicited by high $[Ca^{2+}]_{ex}$ and HA are similar. The experiments testing the effects of Ca^{2+} and hypertonicity will be described later.

3.2.3 Formation of Cold-Resistant Thick MT Fibers in the Recovery Phase after HA Bath

Chlamydomonas expresses Na^+/H^+ exchangers (Pittman *et al.*, 2008), as well as various channels and pumps at different locations (Fujiu *et al.*, 2011; Taylor *et al.*, 2012) to maintain electrolyte homeostasis. I reasoned that altering HA treatment might also change other cations such as Na^+ or K^+. To test this, I extended HA exposure - resuspending cells in pH 3, 10 mM HA/ddw for 5 minutes. As expected, EB1 patterns were absent except for the static signal at the BB area (**Figure 3.3a, left panel**), mimicking the final outcome of HA exposure in the diffusion chamber (**Figure 3.2e**). In contrast, resuspension in pH 3, 10 mM HCl did not alter comet activity. Thus, as with deflagellation, HA-elicited changes in cortical MTs are due to intracellular rather than extracellular acidification. Images were taken as cells were washed with Na^+/HEPES in a perfusion chamber. After washing, dynamic EB1 signals emerged at the BB area after ~50 seconds (**Figure 3.3a, cell I in right panel**). Interestingly, nascent MTs were not adorned with a typical comet. Compared to the bird cage pattern, they appeared thicker, fewer and nearly uniformly decorated, as if plus end tracking EB1 stayed behind growing MTs. In cells recorded at a later period (**cell II and III, between 60 – 159 seconds**), MT growth decelerated, especially between 109-159 seconds. In cells recorded after 180

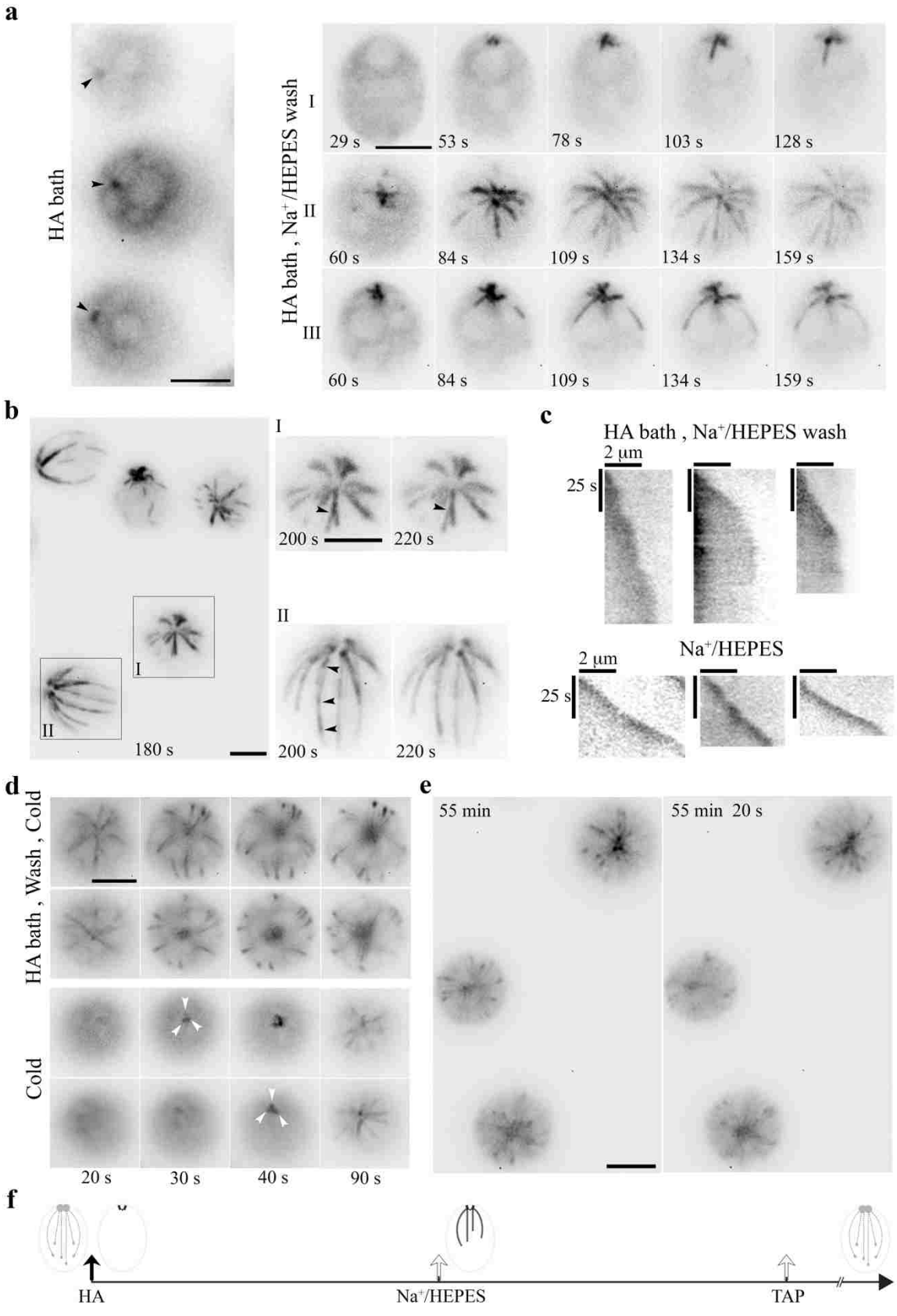
a
HA bath
HA bath , Na+/HEPES wash
I
II
III
29 s
53 s
78 s
103 s
128 s
60 s
84 s
109 s
134 s
159 s
60 s
84 s
109 s
134 s
159 s
b
I
II
180 s
200 s
220 s
200 s
220 s
c
HA bath , Na+/HEPES wash
2 µm
25 s
Na+/HEPES
2 µm
25 s
d
HA bath , Wash , Cold
Cold
20 s
30 s
40 s
90 s
e
55 min
55 min 20 s
f
HA
Na+/HEPES
TAP

Figure 3.3. HA bath and a subsequent wash induced long-lived yet reversible changes to the MT system. (**a**) Static EB1 signals remained at BBs after cells were resuspended in 10 mM pH 3 HA for 5 minutes (left panel). After replacing HA with the HEPES buffer, EB1 signal at the BB area intensified within 1minute (black arrowheads). But newly formed MTs were thick and prominent, lacking the typical comet (right panel, cell I). In cells recorded 60 seconds after wash (cell II and III), MT elongation slowed down gradually. (**b**) In cells imaged ~180 second after wash, EB1-decorated MTs in all cells stopped growing (top panel), as highlighted in two additional images of two representative cells captured 20 seconds apart. In addition, a MT fiber in cell I split into two, while a fiber in cell II had multiple comets aligned in tandem, as if new MTs nucleated or grew on older ones. (**c**) Kymograms comparing the growth of three representative MTs in cells pretreated with 5-min HA bath and then the wash buffer (top panels) and in control cells in the HEPES wash buffer (lower panels). Comets in the latter manifested as intense spots at the plus end. The sharper slopes in the former indicated slower growth and eventually unchanged as the growth paused. (**d**) HA -induced long-lived MTs formed after HA bath and wash were cold resistant (top panels). As shown in two representative cells, frozen MTs remained in the image captured 20 seconds after 3 minutes on ice. The changes in subsequent images were due to drift of focal planes as cells were floating gradually as warming up. In control cells without previous HA exposure (bottom panels), EB1 signals were absent initially (20 second), consistent with cold lability. They gradually emerged at the BB area (white arrowheads) afterwards. (**e**) Although the MT system froze within minutes after HA bath and HEPES wash (t=0 min), comets resumed 55 minutes in cells recovered in TAP media as shown in two images captured 20 seconds apart. Scale bars, 5 μm. (**f**) A schematic summarizes the sequence of MT changes induced by HA bath and wash

seconds, all growth stopped (**Figure 3.3b, left panel**). This is further illustrated by two nearly identical images taken 20 seconds apart of two representative cells (**cell I and II, right panels**). Notably, some static fibers split, or had more than one comet aligned in tandem (**arrowheads**).

Taken together, these observations strongly suggest that nascent MTs generated after HA bath and wash are abnormal, perhaps with a propensity to nucleate ectopically, branching, bundling or growing on top of the other MTs as piggy-back patterns. Kymograms comparing three representative MTs (**Figure 3.3c, top panels**) with growing

MTs in the untreated control cells (**bottom panels**) confirm that EB1 signals extend further toward the BB area in cells recovering from HA bath. MT growth rates, shown by the slopes, fluctuate but were mostly slower than those in untreated control cells. Overall the rates decline until MT growth stops. Thus, contrary to thin, dim, transient MT fibers in the acidification phase (**Figure 3.2**), MTs formed in the recovery phase after HA bath were thick, short, long-lived and bright.

MTs are cold labile, particularly in animal cells. Cold treatment induces MT endwise resorption *in vitro* (Muller-Reichert et al., 1998). To test the stability of these thick MTs formed in the recovery phase, glass slides with a droplet of cells after HA bath and wash were placed on ice for 3 min. Images were taken using the microscope at the room temperature (RT), about 20 seconds after slides were removed from ice. Unexpectedly, most cells were imaged from the apical end and the focal planes drifted continuously, indicating that cells oriented toward the objective lens and floated gradually during this warm up period. As shown in two representative cells, EB1-decorated MTs after HA bath and wash remained after the removal from ice amidst the drift of focal planes (**Figure 3.3d, top panels**). Thus, the thick static MTs formed after HA bath and wash are cold stable. The pattern remained for the subsequent 70-second recording period. In contrast, for the control without HA bath, EB1 patterns were undetectable initially (**bottom panels**), indicating cold lability. Dynamic EB1 signals gradually re-emerged at BBs after 30 second (**white arrowheads**).

To learn if frozen thick MTs after HA bath and wash were reversible, I continued imaging cells in the recovery phase. To prepare for the long recovery, wash buffer was replaced with TAP media. Thawing signs emerged gradually. Compared to frozen thick

MTs (**Figure 3.3a and 3.3b**), at the 55-minute post wash, comet activity was vibrant as if the freeze had never occurred (**Figure 3.3e**). The sequential events occurring after HA bath and wash are summarized in **Figure 3.3f**.

3.2.4 Testing HA-Induced Phenomena by Using a Tubulin Mutant and by Reducing HA Concentrations

To decelerate pH-induced resorption in the acidification phase, I took advantage of a tubulin mutant, *tub2*. A missense mutation near the colchicine binding site in β-tubulin increases MT stability since *tub2* cells are colchicine-resistant, and have more acetylated MTs (Schibler, 1991). In the EB1-NG transgenic *tub2* cells, the comet pattern (**Figure 3.4a, top panels**) appeared indistinguishable from that in WT transgenic cells (**Figure 3.1b**). Thus, our assay is not sensitive enough to report increased MT stability. Interestingly though, in the image taken immediately after resuspension in 10 mM HA, the bird cage pattern with a few comet-like spots already formed in every *tub2* cell (**Figure 3.4a, bottom panels**). The pattern was rather stable, although some MTs seemed to be out of focus intermittently, suggesting detachment from the plasma membrane. As shown in two representative cells, similar frozen bird cage pattern remained even after 5-min HA bath (**Figure 3.4b**). After wash, comets returned (**panel I–II**) and lengthened as in WT cells. However, comets (**white arrowheads**) appeared at the plus end of existing MTs first rather than at BBs where nascent MTs emerged. The bird cage pattern gradually faded concomitantly. For images taken 60 seconds and later after wash, comets formed and moved along existing MTs (**Panel III**). This strengthens the interpreted bundling propensity of MTs in WT cells recovered from HA bath (**Figure 3.3b**). These

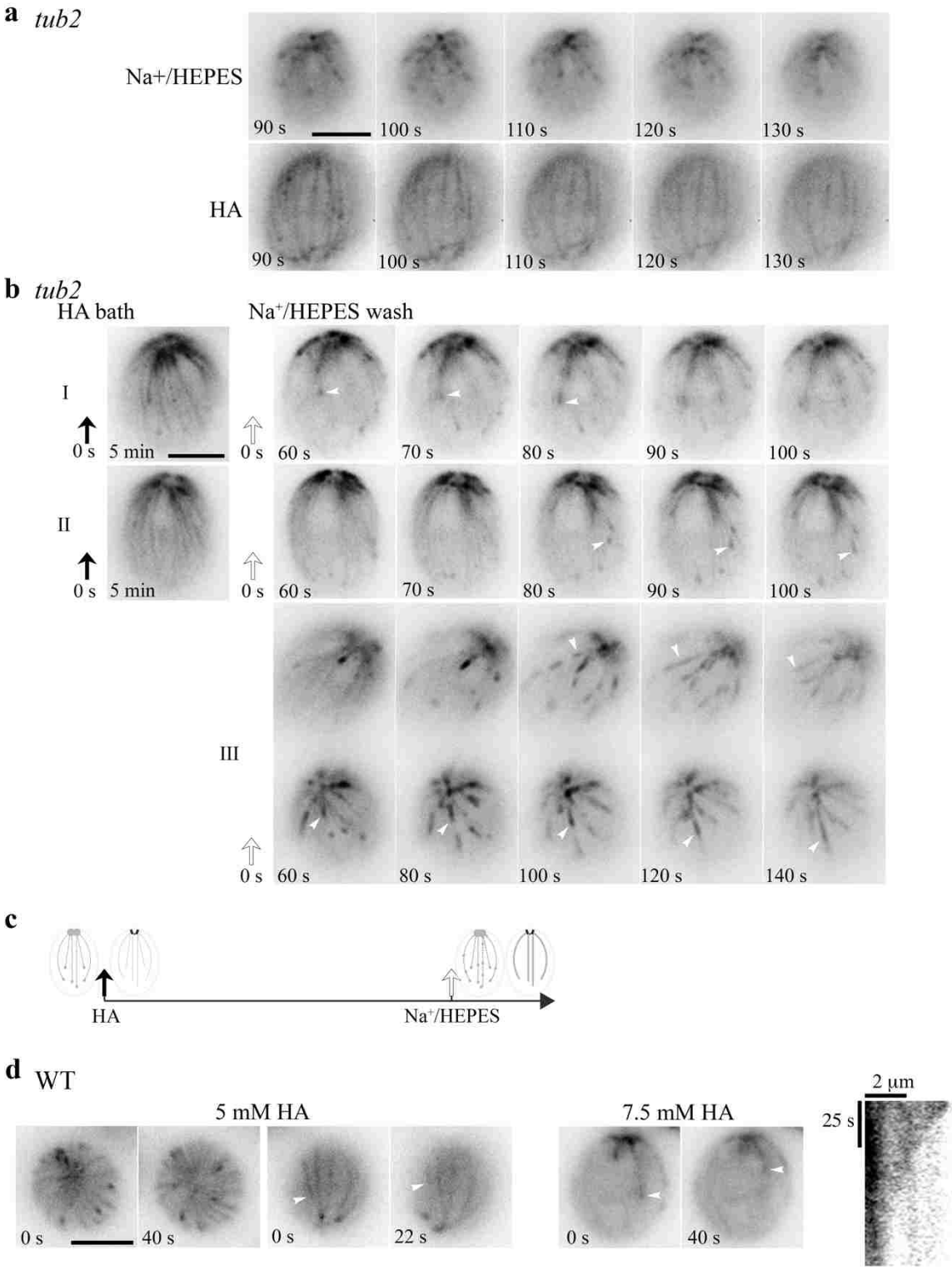
a tub2
Na+/HEPES
HA
90 s
100 s
110 s
120 s
130 s
b tub2
HA bath
Na+/HEPES wash
I
II
III
0 s
5 min
60 s
70 s
80 s
90 s
100 s
120 s
140 s
c
HA
Na+/HEPES
d WT
5 mM HA
7.5 mM HA
0 s
40 s
22 s
2 µm
25 s

Figure 3.4. Tempered HA-induced changes by a β-tubulin mutation (a-c) and by reduced HA concentrations (d). (**a**) Time-lapse images at 10 second intervals showed normal comets in *tub2* cells resuspended in 5 mM pH 7.4 Na^+/HEPES (top panels). In contrast, a bird cage pattern with fine MT fibers was present in *tub2* cells resuspended in 10 mM, pH 3 HA (bottom panels). Most MTs froze but some appeared in and out of focus. (**b**) Frozen bird cage remains after 5-min HA bath as shown in two representative cells (left panel). After wash, comets (white arrowheads) reemerged at the plus end of existing fine MTs, instead of the BB area, while the bird cage pattern was fading. MTs were growing but comets were lengthening and the pace was very slow. In videos recorded only after wash, the recovery was faster. Some comets already emerged from the BB area. Some moved along old MTs and lengthened (panel III, white arrowheads). (**c**) A schematic summary of HA-induced changes in *tub2*. (**d**) Concentration-dependent effects of HA on MTs in WT cells. WT cells resuspended in 5 mM HA exhibited a dynamic bird cage pattern with dynamic comets (left, top and side view). Shrinking MTs were visible in the two side view images taken 22 seconds apart (white arrowhead). Most patterns were absent in cells resuspended in 7.5 mM HA, except a few shrinking MTs (right). A kymograph revealed the endwise resorption. Scale bars, 5 μm.

collective results indicate that the mutation in *tub2* hinders endwise resorption elicited by HA exposure, so that the bird cage pattern with cortical MTs uniformly decorated with EB1 does not vanish; the other responses in *tub2* and WT cells are similar. The HA responses of *tub2* cells are summarized in **Figure 3.4c**.

I further tested whether I could replicate the bird cage pattern in WT cells with less concentrated HA. As shown in two top view images taken 40 seconds apart immediately after resuspension in 5 mM HA (**Figure 3.4d, left panel**), all WT cells had motile flagella and had a dynamic, rather than frozen and long-lived, bird cage pattern in which MTs shrink or grow with a comet, as if the entire MT system were revealed by fluorescent tubulins and fluorescent EB1 simultaneously. The side view images recorded 22 seconds apart revealed endwise resorption of a shrinking MT (**arrowhead**). Only a few resorbing MTs were captured in cells resuspended in 7.5 mM HA (**Figure 3.4d, right panel**). This still cell allows us to plot the kymograph, which shows a tapered

endwise resorption with the initial shortening speed of 4 μm/min. All MT patterns and comets disappeared in cells resuspended in 10 mM HA. Therefore, low [HA] increases EB1 shank-binding, rendering the bird-cage pattern. As HA concentrations increase, MTs stop growing and comets are lost. As resorption continues, perhaps even at a hastening pace, comet and bird cage patterns vanish. The 5 mM HA experiment consistently replicates the light-induced sporadic transient appearance of the bird cage pattern in WT cells (**Figure 3.1, f1**). Changes elicited by 7.5 mM HA partially mimics HA-induced responses in diffusion chambers (**Figure 3.2b–e**).

3.2.5 The Long-Lived EB1-Decorated MTs Are Due to the Rise of Intracellular [Na^+] But Not [K^+]

To identify the ion causing the formation of static thick EB1-decorated MT bundles in cells recovering from HA bath, HA-bathed cells were washed with different solutions. Interestingly, as shown by time-lapse images separated by a 10-second interval, EB1-decorated MT fibers formed only if the wash solution contained Na^+, such as the NaOH-buffered HEPES (5 mM Na^+) or 5 mM NaCl in ddw (**Figure 3.5a, top two panels**). On the other hand, comets resumed profusely if the wash solution lacked Na^+, such as the KOH-buffered HEPES buffer, 5 mM KCl in ddw or plain ddw (**bottom three panels**). Therefore, Na^+ accounts for the reformation of thick, long-lived static MTs in the recovery phase of HA-bathed cells.

Since Na^+ has low permeability compared to K^+ (Ronkin and Buretz, 1960) I predict that Na^+ ions from the wash buffer are entering the cytosol when Na^+/H^+

exchangers are removing H^+. To test this, I resuspended WT cells in 10 mM, pH 8 EGTA buffered by NaOH (final ~21 mM Na^+). Concentrated EGTA and EDTA are classical tools for creating permeable cell models perhaps by Ca^{2+} chelation or other mechanisms (Miller, 1979; Tazawa and Shimmen, 1987; Arikawa and Suzaki, 2002; Prachayasittikul *et al.*, 2007). However, EGTA at this concentration does not influence polymerization of MTs from purified tubulins *in vitro* (Olmsted and Borisy, 1975). As expected, thick EB1-decorated MTs formed after cells were resuspended in Na^+/EGTA for 5 minutes (**Figure 3.5b, left panels**). Thick MTs appeared static after 10 minutes. In contrast, cells resuspended in KOH-buffered EGTA had vibrant comet activities (**Figure 3.5b, right panels**). The static EB1-binding MTs in Na^+/EGTA treated cells were also cold-resistant.

As K^+/ EGTA did not affect comet activity, I depleted $[Ca^{2+}]_{ex}$ with K^+/ EGTA rather than Na^+/ EGTA to test if Ca^{2+} is required for the changes elicited by10 mM HA. After 5 minutes in K^+/ EGTA, 10 mM HA resuspension still elicited the bird cage pattern in *tub2* cells, and caused comets to vanish in WT cells. However, cells quickly burst, indicating perturbed plasma membrane. Thus HA-elicited changes in MTs do not require extracellular Ca^{2+}.

Despite low Na^+ permeability of the plasma memberane, I further tested if boosting Na^+ in HEPES buffer to 55 mM with NaCl was sufficient to change EB1 patterns in WT transgenic cells. Indeed, compared to the growing MTs with typical comets in the control cells in the 5 mM group, in the 55 mM group comets were evident but MTs were growing (**Figure 3.5c, panel I**). This is reflected by the modest tapering of

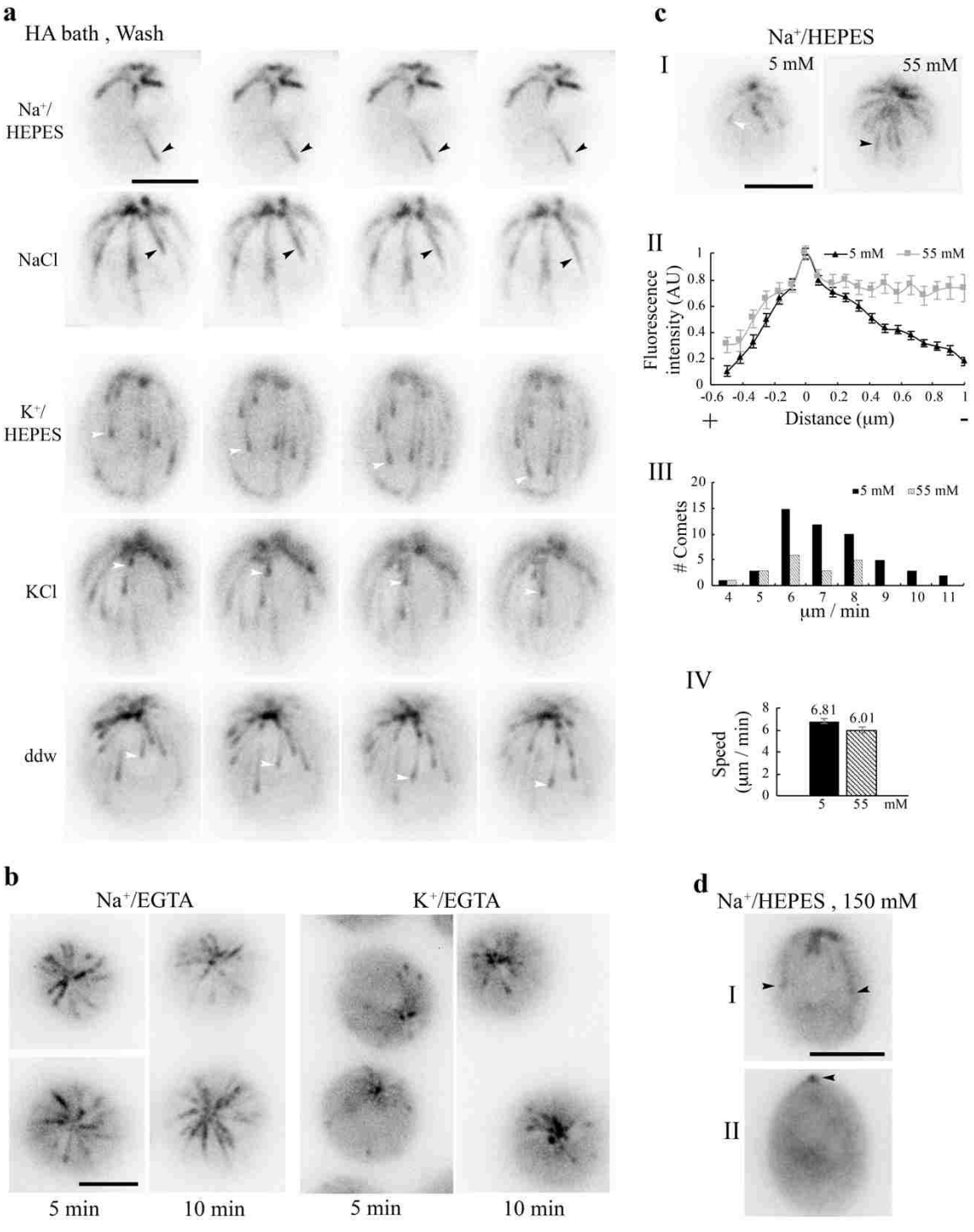
a
HA bath , Wash
Na+/ HEPES
NaCl
K+/ HEPES
KCl
ddw
b
Na+/EGTA
K+/EGTA
5 min
10 min
5 min
10 min
c
Na+/HEPES
I
5 mM
55 mM
II
5 mM
55 mM
Fluorescence intensity (AU)
Distance (μm)
+
-
III
5 mM
55 mM
Comets
μm / min
IV
Speed (μm / min)
6.81
6.01
5
55
mM
d
Na+/HEPES , 150 mM
I
II

Figure 3.5. Na^+-dependent changes of the MT system. (**a**) MTs in cells were largely frozen after 5-min 10 mM pH 3 HA bath and 3 minutes in the wash solution, such as 5 mM pH 7.4 Na^+/ HEPES buffer or 5 mM NaCl solution (black arrowheads). In contrast, growing MTs with a comet (white arrowheads) returned if the wash buffer lacked Na^+, such as 5 mM K^+/HEPES buffer, 5 mM KCl solution, or the ddw. (**b**) Thick MTs in cells resuspended in 21 mN Na^+/EGTA for 5 minutes or 10 minutes (left panel), contrary to comets in cells in 21 mM K^+/ EGTA (right panel). Thick MTs were still growing after 5-minute incubation but static after 10-minute incubation (**c**) High $[Na^+]_{ex}$, without preexposure to HA, was sufficient to alter comet patterns. Contrary to typical comets in cells resuspended in the HEPES buffer with 5 mM Na^+, long comets were thick in cells resuspended in 55 mM Na^+ for 5 minutes (panel I). Normalized linescans confirmed little tapered intensity (panel II, n=36 comets from 11 cells in 5 mM Na^+; n=13 comets from 4 cells in 55 mM Na^+). As shown in the range of speed (panel III) the long comets were moving, and the mean speeds of short and long comets were significantly different (panel IV**,** n=51 from 11 cells in 5 mM Na^+; n=18 from 4 cells in 55 mM Na^+) (two-tailed t-test p-value = 0.0497, < 0.05). (**d**) Two representative cells after 5 minutes in 150 mM Na^+/HEPES. Some cells still retained a few thick MTs (cell I). Some only had static EB1 signals at the BB area (cell II**,** arrowhead). Scale bars, 5 μm.

comet intensity in the linescan plot (**Figure 3.5c, panel II**). Therefore, high $[Na^+]_{ex}$ still could raise $[Na^+]_{in}$, increasing the time EB1 spent at the plus end and thus comet lengths. Despite the long comets, the distribution of comet velocity (**Figure 3.5c, panel III**) and the average velocity (**Figure 3.5c, panel IV**) show that $[Na^+]_{in}$ at this level only slightly reduces MT growth rate (two-tailed t-test p-value = 0.0497, < 0.05). Thus, both comet length and MT growth are sensitive to $[Na^+]$, albeit the former has a higher sensitivity.

To test the effect of hypertonicity, WT transgenic cells were resuspended in 150 and 200 mM $[Na^+]_{ex}$ for 5 minutes before imaging. At these concentrations, flagellar motility ceased. As in 75 mM $[Ca^{2+}]$ solution (**Figure 3.2g**), most comets vanished, although static EB1 signals remained at the BB area (**Figure 3.5d**). However, some cells still contain thick fibers (**top panel**), a signature of Na^+-induced changes. Together, these results show that low Na^+ and high Na^+ elicit disparate MT responses. The modest increase of $[Na^+]_{in}$ from 55 mM $[Na^+]_{ex}$ alone promotes long comets but is insufficient to

stop MT growth. The fact that both responses are triggered by HA bath followed by 5 mM Na^+/HEPES wash or by 21 mM Na^+/EGTA strongly suggests $[Na^+]_{in}$ rises further to a level under 21 mM due to H^+/Na^+ exchange or passive diffusion through EGTA-permeablized membrane. However, most EB1 signal vanished, suggesting MT disassembly at the concentrations considered hypertonic for *Chlamydomonas*, either via $[Na^+]_{ex}$ and/or $[Ca^{2+}]_{ex}$.

3.3 Discussion

Expression of EB1-NG as a reporter loosens the bottle neck posed by autofluorescence of *Chlamydomonas* and unleashes the potential of this MT model system. Contrary to the perceived stability of the MT system in typical interphase animal cells (Lieuvin, 1994), EB1-NG reports in real time the mercurial changes of algal MT system that are elicited by excitation illumination, compression, H^+ and Na^+. I summarize the changes and discuss possible underlying mechanisms; and the new insight on the MT system, plant salinity responses and additional concerns of environmental stresses.

3.3.1 Changes Elicited by H^+

Changes of the algal MT system elicited by intracellular acidification are swift, stunning and novel (**Figure 3.2b–e, 3.3a, and 3.4**). Among heightened shank binding, diminished comet activity, paused MT growths, and MT shortening, the bird cage pattern of shank binding is the most sensitive, elicited reliably by 5 mM HA (**Figure 3.4d**). They are unlikely signaled through cell death pathways, since these changes are reversible, even after 5-minute HA bath (**Figure 3.2b, b3**). The recovery occurs within a minute, either completely (**Figure 3.2b**) or protractedly (**Figure 3.3e**), depending on exposure and wash procedures. Extracellular Ca^{2+} is not required for the HA-induced changes, since they still occur after K^+/EGTA treatment. However, I cannot rule out the involvement of Ca^{2+} released from intracellular storages and other signaling pathways.

Although the pH of $[HA]_{ex}$ that triggers these changes is ~3, I expect that the resulting intracellular pH is close to, or higher than 6.3. HA-induced changes in diffusion chambers appear before deflagellation (**Figure 3.2e**) that occurs at pH 6.3 (Braun and

Hegemann, 1999; Wheeler *et al.*, 2007). Consistent with this, the bird cage pattern could be transiently triggered merely by illumination that may open H^+-selective channelrhodopsin (**Figure 3.1f1**). Conversely, comets return to compressed cells when illumination is turned off for 30 seconds (**Figure 3.1f2**); or return within ~ 45 seconds after HA is washed away (**Figure 3.2b**). These observations strongly suggest that a slight imbalance of pH homeostasis is sufficient to elicit changes in algal MT system.

Although pH affects proteins' ionization and thus their functions and protein-protein interactions in general (Hepler, 2015), I speculate that the MT system is particularly sensitive to declining pH because of the acidic pI of tubulins and EB1. For example, the respective pI of *Chlamydomonas* α-tubulin, β-tubulin and EB1 is 5.01, 4.82, and 5.7. A decrease of pH from the resting level will make these proteins less negatively charged, especially at their C-terminal acidic tails that are central to MT-accessory protein interplays and the targets of various post-translational modifications (Buey *et al.*, 2011; Rovini *et al.*, 2013; Song and Brady, 2015). The resulting decreased repulsion could explain increased affinity of EB1 to GDP-tubulin, leading to nearly immediate appearance of the bird cage pattern in *tub2* cells (**Figure 3.4a–b**) or in WT cells exposed to 5 mM HA (**Figure 3.4d**). As pH descends further, additional changes in protein conformation may inhibit the growth of MTs and EB1 binding at plus ends, leading to comet reduction or ultimate disappearance.

These HA-induced changes explain long standing questions regarding pH variations. For example, in the pollen tube tip, the MT zone is behind the F-actin, Ca^{2+} and acid zone (Gibbon and Kropf, 1994; Hepler, 2015). Likewise, a basic shift directs MT-supported fertilization processes of sea urchins, whereas reducing pH inhibits the

processes and triggers MT disassembly (Schatten *et al.*, 1986). This and an increase of 0.3 – 0.5 pH unit in mitosis inspired the pH clock hypothesis for cell cycle control (Gagliardi and Shain, 2013). In line with this, EB1 preferentially binds to MT plus ends in arrested mitotic phase extract of *Xenopus* oocytes, but uniformly decorates MTs in interphase extract (Tirnauer, 2002) perhaps with a lower pH, analogous to the HA-induced bird cage pattern (**Figure 3.4c**). Given the role of EB1 in recruiting effector molecules and the swiftness of pH-induced changes in MTs and EB1 patterns, tuning pH may indeed control cell cycle at least for certain organisms.

3.3.2 Changes Elicited by Na^+

The responses elicited by $[Na^+]_{in}$ and $[H^+]_{in}$ at low concentrations are distinct. Contrary to instant appearance of H^+-elicited bird cage pattern with fine and individual MTs (**Figure 3.4d**), as Na^+ continues rising, comets lengthen; cortical MTs undergo ectopic nucleation, splitting, bundling, decelerate and stop eventually (**Figure 3.3 and 3.5**). Although it takes longer to elicit Na^+ responses, this is likely due to low Na^+ permeability. Likewise, Ca^{2+} permeability is tightly controlled. As such $[Na^+]_{in}$ and $[Ca^{2+}]_{in}$ cannot be adjusted as nimbly as $[H^+]_{in}$.

The degree of changes correlates with $[Na^+]_{in}$. These changes that are increasing with time in 21 mM Na^+/EGTA (**Figure 3.5b**) indicate that they are occurring before $[Na^+]_{in}$ reaches 21 mM, which is made possible by EGTA treatment. As EGTA chelates Ca^{2+}, this further rules out the involvement of extracellular Ca^{2+}. Similarly, Na^+-dependent responses emerge within ~45 seconds once HA bath is replaced with various solutions containing only 5 mM Na^+ (**Figure 3.5a**), suggesting accelerated rise of $[Na^+]_{in}$

due to the activity of Na^+/ H^+ exchangers (Pittman *et al.*, 2008). On the other hand, by simply relying on limited passive diffusion through the normal plasma membrane, 55 mM $[Na^+]_{ex}$ is sufficient to change comet length but only slows down growth rate slightly (**Figure 5c**). Based on the incremented responses, rather than all-or-none responses to a threshold, I speculate that algal MT system is also sensitive to $[Na^+]_{in}$, perhaps in a linear manner. Contrary to increasing $[Na^+]_{ex}$, raising $[K^+]_{ex}$ had no observable effect (**Figure 3.5a–c**). Although this is reasonable given high $[K^+]_{in}$, ~70 mM in *Chlamydomonas* cells (Malhotra and Glass, 1995), it highlights its selective sensitivity of the algal MT system to Na^+ and rules out mere ionic effects. One interesting possibility is that Na^+ binds to particular sites in algal tubulins, analogous to Ca^{2+} binding sites in mammalian tubulins (Solomon, 1977; Serrano *et al.*, 1985).

3.3.3 Common Changes Elicited by High Extracellular HA, Na^+, and Ca^{2+}

EB1 signals largely vanish at 150 mM $[Na^+]_{ex}$ (**Figure 3.5d**), as in 10 mM HA (**Figure 3.2c and 3.3a**) and 75 mM Ca^{2+} (**Figure 3.2g**) except residual static signals at the BB area. This is likely caused by synergistic disassembly and paused new growth, and an immotile EB1 population underneath BBs respectively (Pedersen *et al.*, 2003; Yan, 2005). The similar outcomes caused by distinct ions and obvious shrinkage of the cell body at even higher concentrations of Na^+ and Ca^{2+} suggest that hypertonicity is involved. I envisage that high concentration responses could be caused by one cation exceeding a threshold concentration; and/or simultaneous rises of multiple electrolytes as H_2O moves out of cells. Hypertonicity may evoke additional pathways.

The capture of endwise resorption only in low concentration conditions (**Figure**

3.2d and 3.4d) suggests that increased concentrations of these ions will heighten shortening- the incidence and/or speed. This is reminiscent of high Ca^{2+} effects. *In vitro*, Ca^{2+} blocks MT formation (Weisenberg, 1972), whereas 0.5-0.6 mM Ca^{2+} - in the absence of MAPs - could increase shortening incidence and accelerate shortening speed of MTs beyond 150 μm/min (Karr *et al.*, 1980; O'Brien *et al.*, 1997). Although pH shock and high $[Ca^{2+}]_{ex}$ only temporarily raise $[Ca^{2+}]_{in}$ up to 1 μM (Wheeler *et al.*, 2007), the lower concentration may be sufficient to heighten shortening. However, this possibility is weakened by the same result despite EGTA treatment.

Other proteins and signaling pathways are involved in the electrolyte-elicited responses. Kinesin-13 that catalyzes MT disassembly at a lower speed (Helenius *et al.*, 2006) becomes phosphorylated within 5 minutes following pH shock; and knockdown of kinesin-13 ameliorated the pH shock-induced reduction in MT lengths and numbers (Wang *et al.*, 2013). Although EB1 patterns appear fully recovered 1 minute after a pH pulse (**Figure 3.2b**), quantitative analysis and using similar reporters are needed to compare the results. Similarly, osmotic or salt stresses activate an atypical tubulin-kinase and phospholipase D to trigger disassembly or reorganization of plant MT system (Dhonukshe *et al.*, 2003; Fujita *et al.*, 2013). For yeast, sorbitol hypertonicity induces frozen MTs (Robertson and Hagan, 2008) and the recovery in 38 minutes involves a stress-induced MAP kinase. Similar paradigms may be responsible for the resumption of MT dynamic in HA-bathed algae that takes ~55 minutes (**Figure 3.3f**).

Electrolyte sensitivity of the algal MT system is contrary to the perceived stable MT system in interphase mammalian cells (Lieuvin, 1994) that have 140 mM $[Na^{+}]_{ex}$, and 140 mM $[K^{+}]_{in}$ (Pohl *et al.*, 2013). Consistent with this, no obvious changes of EB1-

EGFP patterns in mammalian epithelial cells are elicited by compression or illumination (Matov *et al.*, 2010). Likewise, both Na^+ and K^+ promote tubulin polymerization, with 160 mM Na^+ as the optimal condition (Olmsted and Borisy, 1975). Different cation sensitivities could be due to sequence divergence of tubulin. The other is the presence of different accessory proteins. MAPs obscure the cation sensitivity of mammalian MTs (Olmsted and Borisy, 1975; Wolff *et al.*, 1996). Alternatively, signaling pathways or the capacity to maintain electrolyte homeostasis could differ. Thus, while fundamental features of the MT system - likely dynamic instability and EB1 plus end tracking - are universal, electrolyte sensitivity and responses could diverge.

The sensitivity of algal MT system to Na^+ is consistent with enlarged or clustered algal cells cultured in high salt media (Takouridis *et al.*, 2015). This could be caused by anomalies in the MT-supported processes in the cell cycle, such as mitosis and trafficking-dependent release of hatching enzymes (Kubo *et al.*, 2009). Yet this fresh water green alga has several strategies to adapt to salinity (Perrineau *et al.*, 2014), such as glycerol production (Husic and Tolbert, 1986), switches in gene expression (Gao *et al.*, 2016), sexual reproduction and mutations (Takouridis *et al.*, 2015). Salinity adaptation and the incredible H^+ and Na^+ sensitivity of algal MT system that bears semblance to that in both animal and plant cells demand a fresh look at how environmental stresses affect diverse organisms.

One is ocean acidification by anthropogenic CO_2 (Royal, 2005). Hindered shell formation from the resulting extracellular acidification with pH declining by merely 0.1 unit has rightfully raised much alarm (Hoegh-Guldberg *et al.*, 2007; Waldbusser *et al.*, 2013; Fitzer *et al.*, 2016). Similarly, 5 mM and 7.5 mM HA differ 0.09 pH unit based on

the pKa of HA and the Henderson-Hasselbalch equation, but the intracellular acidification from this slight difference triggers distinct changes of Chlamydomonas MT (**Figure 3.4d**). Notably, dictated by CO_2 chemistry, the ratios of permeant CO_2 and H_2CO_3 to non-permeant ionic forms will increase further as solutions acidify, aggravating intracellular acidification. Therefore, intracellular acidification could be equally, if not more, insidious to marine species that are not equipped to cope with this stress; and may poise to shape aqueous landscapes and drive evolution (Cannon *et al.*, 1985).

The other is salt stress and osmostress caused by drought, which is exacerbating due to climate changes or improper agriculture practices. The H^+-enhanced, Na^+-dependent responses of algal MTs (**Figure 3.3a and 3.5**) - bundling, cold-resistance and growth inhibition - resemble salinity-elicited changes in plants (Dhonukshe *et al.*, 2003; Shoji, 2006; Wang *et al.*, 2007; Zhang *et al.*, 2012; Fujita *et al.*, 2013; Hardham, 2013; Hashimoto, 2015; Oda, 2015). The similarity comports with their common cortical MTs and a great homology of their proteins in the MT system (Pedersen *et al.*, 2003; Dymek, 2006; Gardiner, 2013) except flagellar genes (Merchant *et al.*, 2007). MT changes induced by various abiotic stresses, including salt, have prompted an interesting proposition that the MT system is an abiotic sensor of plant cells (Wang *et al.*, 2011a; Haswell and Verslues, 2015). Yet the involvement of signaling pathways and slow readouts in plant experiments question whether the changes of MTs are the consequence of salt stress instead. The EB1-reported, scaled responses that seem proportional to $[Na^+]_{in}$ and the speed of manifestations (**Figure 3.4d and 3.5**) in fresh water algae strengthen the possibility that the plant MT system is an upstream player in the salinity signaling pathways, if not the very sensor. In line with this, channel-linked MTs are

integral to osmolarity signaling transduction in mammalian osmosensory neurons (Prager-Khoutorsky *et al.*, 2014). Using the experimental strategies developed in this study, it is possible to investigate quantitatively the diverged mechanisms of eukaryotic MT systems in sensing and responding to salt stresses.

CHAPTER 4: FLAGELLA STANDARDS FOR QUANTITATIVE FLUORESCENCE MICROSCOPY

4.1 Introduction

With ever improving technologies, fluorescence microscopy is now widely used to reveal the secrets of cells in snap shots or real time. And yet it remains cumbersome to estimate the number of molecules based on the intensity of fluorescent images. Much of this is due to constraints inherent to light. For example, fluorescence intensity is influenced by excitation light spectra and intensity, which in turn could be affected by the age and condition of excitation source. Furthermore, intense excitation light can saturate and bleach fluorophores. The brightness, contrast and linear range can be further altered during image acquisition and by image processing designed to maximize the sensitivity and image quality. As such, quantitative analysis of fluorescent images is often expressed in relative terms.

Although several fluorescent standards such as quantum dots to DNA-origami (Michalet *et al.*, 2005; Schmied *et al.*, 2014) are available, intensity standards for regular fluorescence microscopy - akin to protein markers or DNA ladders for electrophoresis - remain elusive. I reasoned that eukaryotic flagella could be converted into such standards with appropriate intensity, scale and biocompatibility that allows to be imaged with biomedical samples.

Eukaryotic cells utilize motile flagella, or the synonymous cilia, to sweep surrounding fluid. The rhythmic movement is typically powered by a nanomachine, the

9+2 axoneme in each flagellum, with 9 microtubule doublets encircling two singlet microtubules in the center (Smith and Yang, 2003) (**Figure 4.1Aa**). Both types of microtubules associate with a variety of molecular complexes distributed at a precise location periodically throughout the length (**Figure 4.1Ab**) like a nanoruler. In theory, the proteins in these complexes could carry defined numbers of fluorescent proteins per unit length, and, thus such, flagella could be used as standards. To test this, I engineered transgenic algae, *Chlamydomonas* that grew fluorescent flagella in which a fluorescent protein (FP) was fused to an axonemal protein of known stoichiometry. I then demonstrated the linearity of their fluorescence and their utility as intensity standards for quantitative analysis of diverse fluorescence images.

4.2 Results

4.2.1 RSP3 as a Fluorophore Carrier

Various tags were added to axonemal proteins without obvious effects on axonemal assembly and functions (Bower *et al.*, 2013; Oda *et al.*, 2014; Yanagisawa *et al.*, 2014). For this proof-of-principle study, I used the well-characterized RSP3 in the radial spoke (RS) to carry a FP. Under electron microscopy (EM), the RS appears like a Y-shaped complex with a stalk anchoring to outer doublets and its enlarged head projecting toward the center (**Figure 4.1Aa–b, arrowheads**). For *Chlamydomonas*, two RSs are positioned at a 32-64 nm alternate interval throughout the length of each outer doublet (**Figure 4.1Ab**). Thus a 96-nm flagellar segment will contain 18 RSs (= 9 outer doublets X 2).

The RSP3 homodimer spans the RS with its C-terminal tail at the spokehead (Sivadas *et al.*, 2012; Oda *et al.*, 2014) (**Figure 4.1Ac–d, arrows**). As a structural scaffold, RSP3 dimer binds to the other spoke subunits (Sivadas *et al.*, 2012; Oda *et al.*, 2014) and docking the RS to outer doublets (Diener, 1993). As such, *Chlamydomonas* RSP3 mutant, *pf14*, generates paralyzed flagella lacking nearly all RSs (Huang, 1981). RSs and motility is fully restored by introducing genomic DNA expressing RSP3 without or with a tag (Williams, 1989; Gupta *et al.*, 2012; Sivadas *et al.*, 2012). This allows us to tag nearly every RSP3 in flagella. In theory, every 96 nm in the flagella of transgenic *pf14* strains with fully restored RSP3 tagged with a fluorescent protein (FP) would have 36 (=18 X 2) RSP3 molecules and thus 36 FPs. The dispersion of FPs and the protection of the protein shell (Gather and Yun, 2014) shall minimize photoquenching.

Curiously, a study resorted to immunofluorescence to amplify the signal of

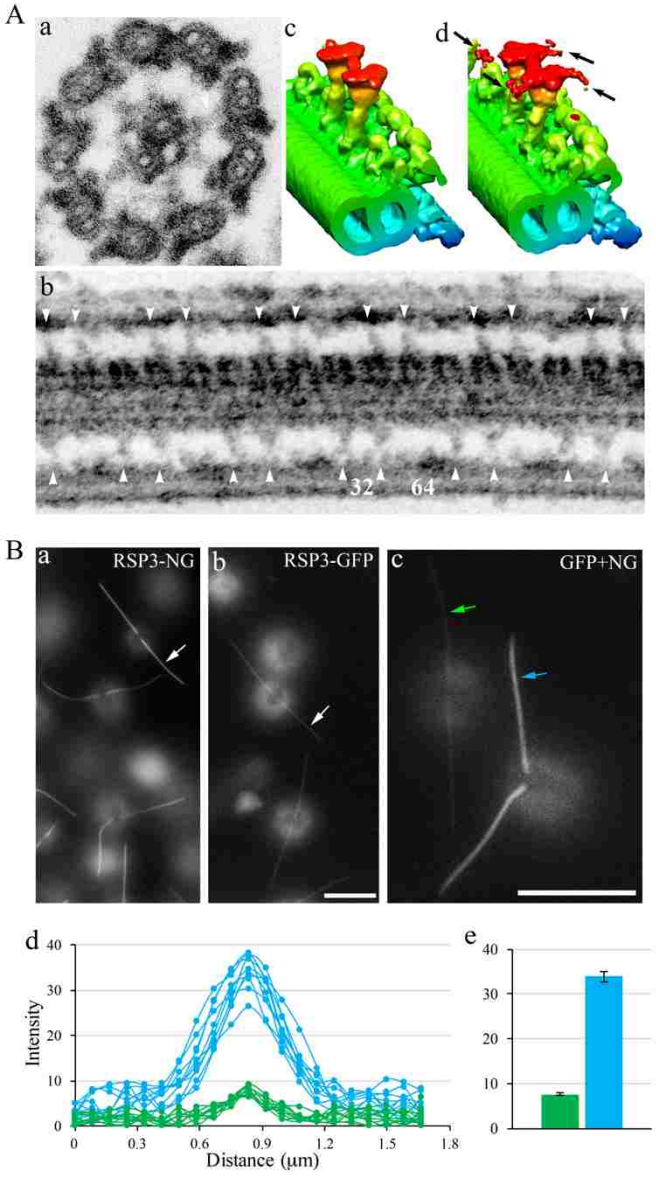

Figure 4.1. *Chlamydomonas* flagella with fluorescent RSP3 in the radial spokes. (**A**) Radial spokes (white arrowhead) are anchored to each of the 9 outer doublets revealed in the axoneme cross section (a), and appeared as a pair every 96 nm in the longitudinal section (b). Comparison of a 96-nm repeat derived from cryo-electron tomograms of flagella with RSP3 (c, EM database ID, 5845) or with RSP3-streptavidin (d, EM database ID, 5847) shows that RSP3's C-terminal tag is near the spoke head region (arrows). Bar, 100 nm. (**B**) RSP3-NG flagella are brighter than RSP3-GFP flagella. (a) Live RSP3-NG cells. (b) Live RSP3-GFP (cells) (c) Co-imaging of cells with RSP3-NG (blue arrow) and

RSP3-GFP (green arrow) flagella. Fluorescence intensities of flagella were measured by using a line tool across the flagella and presented as a profile plot (d) and peak intensity histogram (e), n=10, Mann-Whitney U test, $P < 0.001$. The distance represents the length of the line tool. Bar, 10 μm.

enhanced green fluorescent protein (EGFP) tagged to an axonemal protein in *Chlamydomonas* (Bower *et al.*, 2013). Thus, I engineered genomic constructs expressing RSP3 tagged to a CrGFP or NG that was 2.7 X-fold brighter than EGFP but had similar excitation and emission spectra and photostability (Shaner *et al.*, 2013). Upon transformation into *pf14*, the plasmid would insert randomly into the genome. Typically, nearly 1/3 of insertional events led to the expression of both antibiotic resistant gene and the RSP3 gene. For fully rescued clones, all cells swam like WT cells, while their flagella contained normal levels of RSP3-FP as shown by western blots.

4.2.2 Comparison of RSP3-CrGFP Flagella and RSP3-NG Flagella

For imaging, cells were coerced to adhere to coverslips with flagella, to position the autofluorescing cell body at a distinct focal plane (Harris *et al.*, 2015). All images were acquired with a 40 X objective and a 1-second exposure unless stated otherwise. Both RSP3-NG and RSP3-CrGFP appeared evenly distributed throughout the entire flagella except the distal end where outer doublets taper off and the proximal end that overlapped with the cell body (**Figure 4.1Ba-b**). When imaged together, RSP3-CrGFP flagella were clearly dimmer than RSP3-NG flagella, barely distinguishable from autofluorescence (**Figure 4.1Bc**). Curiously, an intensity profile plot measured across flagella (**Figure 4.1Bd**) and the peak intensity (**Figure 4.1Be**) showed that RSP3-NG flagella - in the presence of the cell body - were approximately 4.4 X brighter than RSP3-

CrGFP flagella (Mann-Whitney U test, $P < 0.001$), rather than the expected 2.7 X ratio. The ratio was still 3.2 X for purified flagella. Interestingly, we found there are two mutations, I_{204} and H_{232}, in CrGFP polypeptide different from the commonly known EGFP. After reversing both mutations to T and L respectively, the corrected CrGFP was brighter than the original one. Quantification of large sample sizes is needed to confirm if the corrected CrGFP flagella are only 2.7 X dimmer than NG flagella. For the rest of analysis, I focused on RSP3-NG flagella.

4.2.3 Characterization of RSP3-NG Flagella

Entire flagella of ~12 μm in suspension often did not orient in one focal plane. Those that did, glow evenly throughout the length (**Figure 4.2Aa**). The focal plane problem was alleviated by air drying flagella on poly-L-lysine-coated glass surfaces. Plasm membranes are negative-charged that can associate with negative-charged poly-L-lysine. Flagella appeared unchanged following rehydration (**Figure 4.2Ab**). This may simplify packaging of flagella as commercial products. Interestingly, the profile plot (**Figure 4.2Ac**) and peak intensity histogram (**Figure 4.2Ad**) showed that rehydrated flagella became 1.4 X brighter than never-dried flagella (two-tailed t-test p-value < 0.001). This and the increased FP intensity following alkaline treatment (Xiong *et al.*, 2014) showcase non-genetic modulations of FP intensity.

To assess the linear range, I measured the intensity of the overlapped region and the nearby non-overlapped region of rehydrated flagella (**Figure 4.2Ba**). As expected, the peak intensity of individual measurements (**Figure 4.2Bb**) or the averages (**Figure 4.2Bc**) showed that the overlapped regions (**grey bars**) were about 2 X brighter than the

nearby regions (**blue bars**) (two-tailed t-test p-value < 0.001). I also measured split axonemal fibers. Typically, 9 outer doublets would splay in buffers containing protease that broke down the structural constraints. To prevent RSs from degradation, I instead applied shear force, manually moving back-and-forth coverslips adhered with flagella. Such maneuvers split most flagella into 2 to 3 fibrous bundles visible with a 100 X objective and a 9-second exposure (**Figure 4.2Ca**). Analysis of enlarged images (**Figure 4.2Cb–f**) showed that individual subfibers were 1/2 - 1/3 as bright as the intact region. Thus, the reduced intensity level is still within the linear range. Notably, some subfibers became further fragmented (**Figure 4.2Cd–e**). 20-second exposures revealed released fragmented particles (**Figure 4.2Cf, green arrows**) of seemingly uniform size and intensity that was ~1/12th of the intact region (**red arrow**). These "quant"-like particles remain to be investigated.

4.2.4 Retained NG Fluorescence after Methanol Fixation

Albeit prized for live cell imaging, FPs are easily obscured by intense autofluorescence from chlorophyll and similar pigments in plant cells. While methanol fixation can extract pigments, it also renders GFP nearly invisible. I found that RSP3-NG flagella indeed became dimmer after methanol fixation (**Figure 4.3Aa, red dots**) compared to unfixed ones (**blue dots**). Quantitative analysis (**Figure 4.3Ab–c**) showed that methanol fixation reduced NG fluorescence intensity by ~60% (two-tailed t-test p-value < 0.001). Notably, the overlapped regions (**white arrows and grey bars**) of fixed flagella were still about two times brighter than non-overlapped regions (**red bars**) (two-tailed t-test p-value < 0.001). Thus, the dimmer methanol-fixed RSP3-NG flagella are

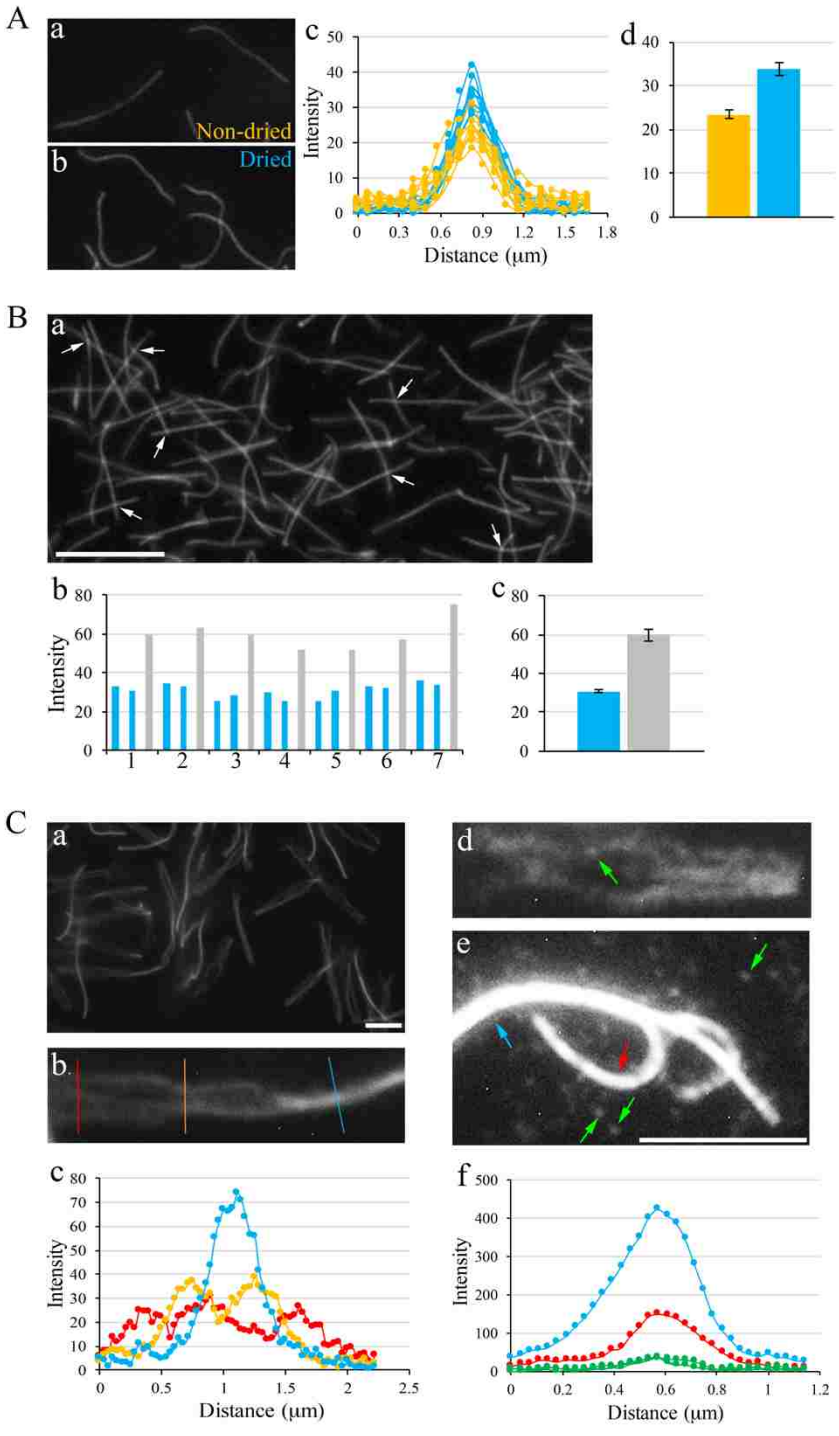
A
a
Non-dried
b
Dried
c
Intensity
Distance (μm)
d
B
a
b
Intensity
c
C
a
b
c
Intensity
Distance (μm)
d
e
f
Intensity
Distance (μm)

Figure 4.2. Quantitative analysis of fluorescence intensity of RSP3-NG flagella. (**A**) Comparison of flagella in suspension (a) and rehydrated flagella following air dry (b). Fluorescence distributed evenly throughout the length of excised flagella. Dehydration made flagella fully adhered to poly-L-lysine coating, rendering entire flagella at the same focal plane. It also enhanced fluorescence intensity of NG flagella, as shown in the profile plot (c) and peak intensity histogram (d), n =10, two-tailed t-test p-value < 0.001. (**B**) Doubled intensity at overlapped regions. The peak intensity at overlapped regions (a, gray arrows) from 7 flagella was nearly two-fold to that at nearby non-overlapped region as shown in individual measurements (b) and as averages (c), two-tailed t-test p-value < 0.001. Bar, 10 μm. (**C**) Reduced intensity of split RSP3-NG flagella. Manual movements of coverslips sheared the microtubule bundle in the adhered flagella into subfibers visualized with a 100 X objective and a 9-second (a-b, d) and 20-second (e) exposure. Some subfibers were further sheared into fragments (d-e, green arrows), some of which were released as quant-like particles (e). Fluorescence intensity was measured in enlarged images at the regions marked by color lines or arrows (b, e) and presented as profiles of the corresponding color (c, f). The distances represent the length of line tools across the flagella at the indicated positions. Bars, 5 μm.

still within the linear range.

To assess the removal of autofluorescence, I analyzed methanol-fixed *Chlamydomonas* cells expressing EB1-NG (Harris *et al.*, 2015). After rehydration, live cells were added to the slide prior to image acquisition. EB1 preferentially binds to the plus end of growing microtubules, rendering a typical comet pattern in live or fixed cells. While EB1-NG comets in fixed cells (**Figure 4.3B, orange arrow**) were dimmer than in live cells (**blue arrow**), autofluorescence also decreased proportionally. For images with lower autofluorescence, methanol fixation may increase signal to background ratio (S/B). Methanol-fixed comets were visible after a 10-second exposure (**Figure 4.3Ba–b**) and remained visible after the subsequent 1-second exposure (**Figure 4.3Bc–d**), demonstrating NG's photostability and the value of low excitation light intensity. As expected, exposure times affect EB1-NG comet lengths in live cells but not in fixed cells. Thus, NG and RSP3-NG flagella are compatible with methanol fixation that could be

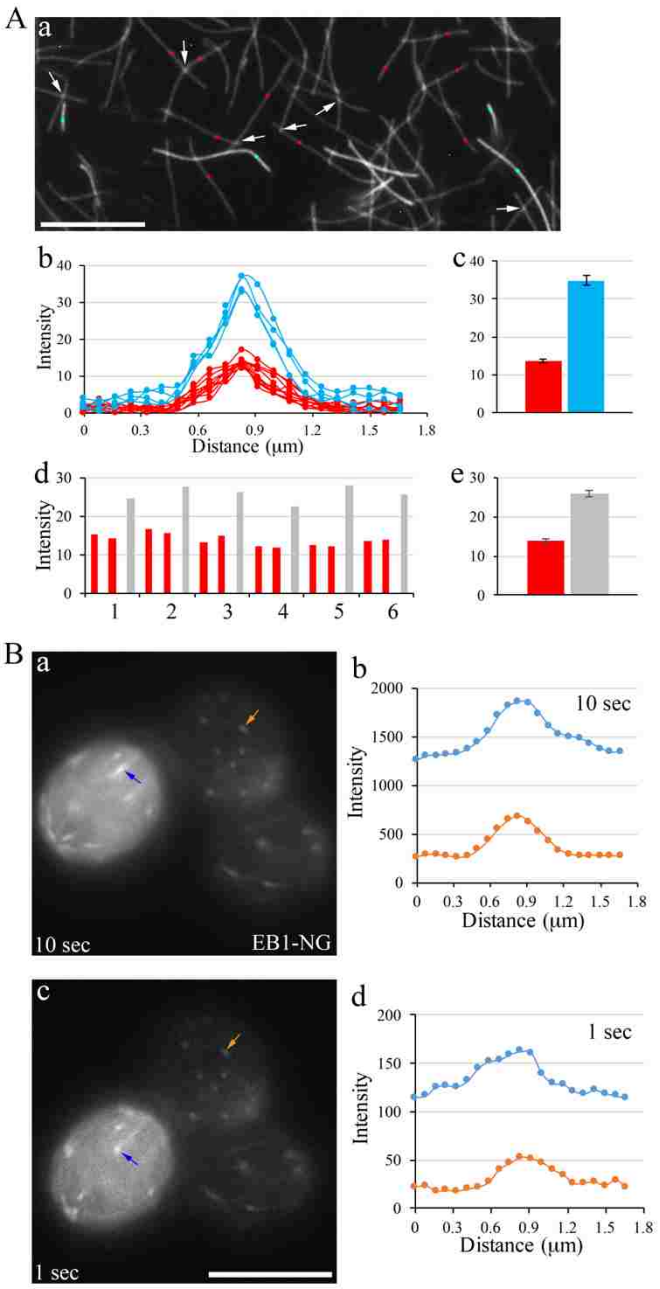

Figure 4.3. The effects of methanol fixation on NG fluorescence and autofluorescence. (**A**) Reduced intensity of RSP3-NG flagella following methanol fixation. RSP3-NG flagella adhered to a poly-L-lysine-coated slide were fixed with methanol first. The image was acquired following rehydration and addition of unfixed flagella (a). Fixed (red dots, n=10) flagella are significantly dimmer than unfixed (blue

dots, n=4) flagella (two-tailed t-test p-value < 0.001). Overlapped regions (arrow, n=6) of fixed flagella are around two-fold brighter than the individual ones (n=12, two-tailed t-test p-value < 0.001). Fluorescence intensities were measured and presented as a profile plot (b), peak intensity histogram (c), individual (d) and average (e) intensity histogram at overlapped and neighboring regions. (**B**) Methanol fixation reduced EB1-NG signal (orange arrow) and autofluorescence in the cell body (blue arrow) proportionally in WT cells immobilized on poly-L-lysine-coated slides. The images were acquired following rehydration and addition of live cells (a, c) and quantitatively analyzed (b, d). Note, with limited intensity of excitation light, EB1-NG comets were detectable in 1 second (c) exposure following a 10-second exposure (a). Their length appeared identical regardless of exposure time, contrary to comets in live cells (blue arrow). Bar, 10 μm.

used in imaging events that are highly dynamic and objects that are moving rapidly or obscured by autofluorescence.

4.2.5 Application of RSP3-NG Flagella

I then used RSP3-NG flagella to estimate the numbers of fluorescent fusion proteins. For elongated objects as flagella, I obtained rough estimates by comparing the peak intensity measured across indicated sites. For closer estimations or objects of a non-linear shape I compared mean intensities (total intensities/area). I first compared RSP3-NG flagella with EB1-NG-enriched tips of full length flagella where plus ends of 9+2 microtubules turned over perpetually (Marshall and Rosenbaum, 2001; Harris *et al.*, 2015). The tip EB1-NG population is dynamic. The intensity reduces as flagella reach full length. As shown by images of live cell flagella adhered to coverslips (**Figure 4.4A**), EB1-NG tips of ~1-μm long (**red arrows**) were as bright as, or slightly dimmer than, RSP3-NG flagellum segments (**blue arrows**) (two-tailed t-test p-value = 0.771, > 0.05). Considering the similar abundance of tagged and untagged EB1 (Harris *et al.*, 2015), this equates to 270 EB1-NG molecules and thus 270 EB1 dimers recruited to the flagellar tip

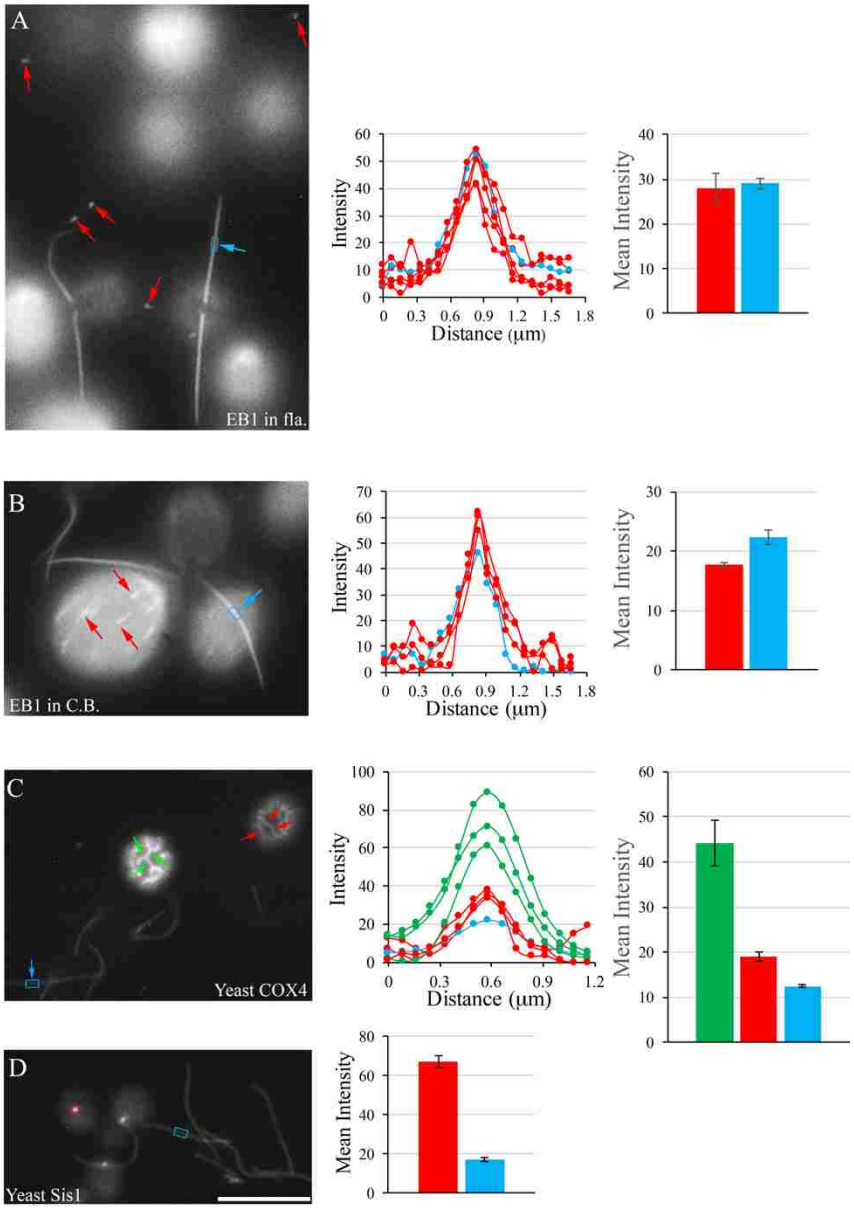

Figure 4.4. Applications of RSP3-NG flagella as fluorescence intensity standards. Flagella were co-imaged with objects of interest (left panels). The indicated sites (arrows) and encircled area, including 2-μm flagellar segments (blue rectangles) as standards, were measured. The corresponding profile plot, peak intensity histogram or mean intensity (total intensity/selected area) histogram were shown at the right. (**A**) Comparison of EB1-NG at flagella tips of live cells with RSP3-NG flagella adhered to the glass slide, n=3, two-tailed t-test p-value = 0.771, > 0.05. (**B**) Comparison of EB1-NG

comets underneath the plasma membrane and RSP3-NG flagella from live suspended cells, n=3, two-tailed t-test p-value = 0.026, < 0.05. Only the flagella segments and EB1 comets at similar focal planes were measured. (**C**) Yeast cells expressing different amounts of COX4-GFP that illuminated mitochondrial tubules. 580-nm mitochondrial segments, n=3, represented by green and red arrows; rehydrated flagellar segments, n=10, represented by a blue arrow. Mitochondrial tubules labelled by green arrows are brighter than the red labelled, two-tailed t-test p-value = 0.008, < 0.05. The dim mitochondrial tubules are brighter than flagellar segments, two-tailed t-test p-value < 0.001. (**D**) Yeast cells expressing Sis1-GFP. A fraction of Sis1-GFP was enriched in one spot (IPOD). A IPOD is significantly brighter than a flagellar segment. IPOD, n=3; flagella segments, n=10. Mann-Whitney U test, P < 0.001. Bar, 10 μm.

that contain 20 microtubules (9 X 2 + 2 in **Figure 4.1A**).

Interestingly, it was reported that there are ~ 270 EB dimers in each comet of growing microtubules in epithelial cells (Seetapun *et al.*, 2012). To assess EB1-NG comets in *Chlamydomonas*, I compare RSP3-NG flagella with EB1 comets primarily at the tip of growing cortical microtubules underneath the plasma membrane, following the cell body contour (Harris *et al.*, 2015). Profile plots of comets and flagella at a similar focal plane showed that the leading end of most comets (**Figure 4.4B, red arrow**) were also as bright as RSP3-NG flagella, if not brighter (**Figure 4.4B, profile plot**). However, the averaged fluorescence intensity of an entire comet region is dimmer than that of a flagellum segment (two-tailed t-test p-value = 0.026, < 0.05) (**Figure 4.4B, profile plots and histogram**). This equates to ~160 or 270 EB1 dimers/ comet, depending on the background area selected for subtraction. This shows that microtubule dynamics in fresh water algae and in mammalian cells are similar; and background and perhaps the threshold algorithm selected for defining comets' boundary will influence the estimate. Furthermore, the similar EB1 molecules in one comet and in a flagellar tip that contains 20 microtubules suggest that the rate of the perpetual microtubule turnover at the full

length flagellar tip decelerates to ~1/20th of a growing microtubule in the cell body. This information may foster new models of flagellar length control.

To demonstrate broad utilities, I imaged rehydrated flagella with transgenic *Saccharomyces cerevisiae* strains expressing fusion proteins irrelevant to microtubules. One strain expressed GFP tagged to the first 21 amino acids of COX4 in the cytochrome c complex (Jensen *et al.*, 2000). COX4-GFP illuminated the mitochondrial tubular network but its level varied among individual yeast cells (**Figure 4.4C**). Measurements of 580-nm long areas (**arrows**) showed that the mitochondrial tubule in one cell was about twice as bright as that in the other cell (two-tailed t-test p-value = 0.008, < 0.05) and the dim tubule was still brighter than RSP3-NG flagella (two-tailed t-test p-value < 0.001) (Figure 4.4C, histogram). Taking into consideration of the larger diameters of mitochondria (Pedersen *et al.*, 2003; Westermann, 2008), the 2.7 X brightness ratio of NG/GFP, and the 1.4 X brighter rehydrated RSP3-NG flagella, a 96-nm mitochondria segment on average would contain ~581 COX4-GFP polypeptides in the bright cell and ~200 in the dimmer cell, compared to 36 RSP3-NG in a 96-nm flagellar segment. This showcases an easy way to determine kinetics of diverse reactions in mitochondria.

The other yeast strain expressed GFP-tagged Sis1, a HSP40 co-chaperon involved in trafficking misfolded polypeptides to the insoluble protein deposit (IPOD) (Kaganovich *et al.*, 2008; Specht *et al.*, 2011; Nillegoda and Bukau, 2015). IPOD enriched with Sis1-GFP appeared as a punctum with a mean intensity nearly 4 X greater than rehydrated RSP3-NG flagella (Mann-Whitney U test, P < 0.001) (**Figure 4.4D**). This equates to ~2,800 Sis1-GFP molecules / IPOD of a 650-nm diameter - approximately 1/7 of the estimated 20,500 Sis1 molecules in one yeast cell

(Ghaemmaghami *et al.*, 2003). I envisage that the abundance of Sis1 could be used to determine the capacity of chaperones in trafficking of misfolded proteins, not only at permissive but also at restrictive temperatures and in various mutants.

4.3 Discussion

This study harnesses a *Chlamydomonas* RSP3 mutant, the RS periodicity and the defined RSP3 stoichiometry in the 9+2 axoneme to create a new intensity standard for regular widefield fluorescence microscopy. The 2 X brightness at the overlapping regions in unfixed flagella (**Figure 4.3B**) and 1/3 dimmer methanol-fixed flagella (**Figure 4.5A**) indicate at least a 6 X linear range.

Several factors may influence the accuracy level of the estimates. One is the S/B, especially for signals far weaker than the standard (**Figure 4.2Cc**) or strong backgrounds (**Figure 4.4B**). For example, as the signal of RSP3-CrGFP flagella is barely above the background, the ratios of RSP3-CrGFP/RSP3-NG, measured with or without cell body, differ and are higher than the expected value (**Figure 4.1B**). Photobleaching and phototoxicity may reduce accuracy. This could be avoided by using minimal excitation light in exchange of a longer exposure time (**Figure 4.3B**). Once images are acquired, images could be further adjusted without affecting profile plot analysis. Another factor is focal planes as shown in different flagellar areas and EB1 comets of curved cortical microtubules (**Figure. 4.4A–B**). This could be addressed by quantifying standards and objects at different focal planes captured in separate images but with identical imaging parameters. Similar principles may be applicable to quantify 3D objects acquired by confocal microscope. In a same vein, different images could be compared quantitatively, as long as image acquisition conditions and flagellar standards were identical.

It is worthwhile to point out that contrary to the toxicity of common quantum dots, flagella are biocompatible. In addition, by using molecular biology and genetic tools amenable to *Chlamydomonas* to switch tags or carrier proteins of different periodicities

(Yanagisawa *et al.*, 2014), the spectroscopic properties and intensity of flagellar standards could be tweaked further. Finally, it is rather easy and economical to harvest flagella in large quantities. With these advantages, I foresee broad applications of flagella standards in quantitative fluorescent images analysis.

CHAPTER 5: DISCUSSION

Intense autofluorescence has constrained investigations of cells with chloroplasts. By addressing this key issue and taking advantage of *Chlamydomonas* as a model organism, this dissertation resulted in critical discoveries of broad significance and improved the applications of fluorescence microscopy.

5.1 Overcome of Fluorescence from Chloroplast

Previous studies and this dissertation address partially the fluorescence background that obscure signals in cells with chloroplasts. One strategy is to elevate the S/B, by raising signals and/or reducing background. It was demonstrated recently that among the FPs expressed in *Chlamydomonas* and measured using respective optimal filter sets in a spectrophometer, CrGFP's S/B is the lowest (Rasala *et al.*, 2013), whereas mCherry's S/B is ~2X higher than CrGFP's. FPs with yellow and orange emission spectra have the highest S/B. While this is disheartening given the popularity of GFP and EGFP, it shows that red FPs could be useful so long as proper filters are used to block red intense fluorescence with emission spectra longer than 640 nm from key fluorophores in chloroplast (Welschmeyer, 1994; Ustin *et al.*, 2009; Kleinegris *et al.*, 2010) (**Table 5.1**). However, these findings do not exactly agree with our observations of CrGFP (Fuhrmann *et al.*, 1999), NG (Shaner *et al.*) and mCherry (Lectreck) using a commonly used wide-field fluorescence microscopy.

Consistent with the lowest S/B ratio of CrGFP among all FPs measured in *Chlamdyomonas* (Rasala *et al.*, 2013), CrGFP fusion proteins are exceedingly dim. EB1-NG imaged with the filter sets for FITC/EGFP is the only fusion protein tested in this dissertation that could reveal the expected comet pattern. In contrast, EB1-CrGFP and EB1-mCherry could only reveal the basal body area and the flagellar tip which were spatially separated from the chloroplast (not shown). Furthermore, RSP3-NG flagella are 4.4 X brighter than RSP3-GFP flagella - rather than the expected 2.7 X (**Figure 4.1Bd–e**).

We found that the unexpected low intensity of CrGFP is due to two residues near the C-terminus of CrGFP - I_{204} and H_{232} - that differ from those in commonly used EGFPs. In particular, GFPs with I_{204} lack the second excitation peak around 488 nm (Ehrig *et al.*, 1995) - the very excitation spectra for the first evolved EGFP (Heim *et al.*, 1995) and permitted by the optimal filter set for FITC and GFP. This suggests that CrGFP cannot be properly excited using the filter sets for GFP and thus leading to the low S/B ratio. After site-directed mutagenesis, replacing I and H back to T and L, respectively, in most EGFP variants, the intensity of RSP3-EGFP flagella is visibly brighter than flagella with RSP3-CrGFP and dimmer than flagella with RSP3-NG as expected (not shown). These two fluorescent standards remain to be compared quantitatively to test if the intensity ratio is near the expected 2.7. Thus, I created RSP3-NG flagella (**Figure 4.2**) and RSP3-EGFP flagella for fluorescence standards; and recovered the EGFP plasmid for the *Chlamydomonas* community.

While mCherry's S/B is 2 X higher than CrGFP, EB1-mCherry was undetectable at all under the typical mCherry/Texas red filter sets. Only when the long path emission

filter was replaced with a short band path one, EB1-mCherry signals at the basal body area emerged as EB1-CrGFP. This illustrates that filter band paths should be tailored for

Table 5.1. Spectra of key photosynthetic pigments and fluorescent proteins

	Excitation (nm)	**Emission (nm)**
Chlorophylls (Welschmeyer, 1994)	Peaks 400 – 480; 625 –700	Peak 640 – 680
Carotenoid (Kleinegris *et al.*, 2010)	Peak 400 – 550	Peaks 540 – 600; > 650
EGFP (Shaner *et al.*, 2005)	Peak 488	Peak 507
NG (Shaner *et al.*, 2005)	Peak 506	Peak 517
mCherry (Shaner *et al.*, 2005)	Peak 587	Peak 610
Filters for CrGFP/EGFP/NG (Used in this dissertation)	460 – 500	510 – 560
Filters for mCherry (Used in this dissertation)	532 – 587	595 – 635

FPs as well as cell types. However, surprisingly, EB1-mCherry comets were still invisible. Given the narrow band path, it is not feasible to use an even narrower emission filter which will further reduce mCherry signals. The problem may be partly due to the new emission filter being too narrow, sacrificing too much long spectra mCherry signals. This could be tested using an emission filter with a ~10-nm red shift. The problem may be due to the rising intensity of red spectra autofluorescence during imaging. This unexpected phenomenon was not reported in the previous study using instant readouts of spectrophotometer and deconvolution microscopy in which out-of-focus signals are subtracted by computation (Rasala *et al.*, 2013). While this phenomenon will be less

problematic for snapshot images, deconvolution microscopy or high abundance of FPs, it could pose substantial challenges for recording a process of more than one minute. It remains to be investigated if reduced excitation intensity will dampen the rise of red autofluorescence. It will also be useful to measure the spectra range of this fluorescence and identify the autofluorescence emitter. If the spectrum extends lower, this may limit the advantages of yellow and orange FPs. Mutagenesis, abolishing the enzyme producing the causative compounds may be possible to address this problem that will limit the usefulness of the commonly used mCherry in the cell body.

In contrast, although EB1-NG is only 4.4 X brighter than CrGFP, it is sufficient to reveal the comet pattern and the electrolyte-induced switches of this pattern and MT dynamics (**Figure 3.1 – 3.4**). Even though I have not created EB1-EGFP strain, its S/B is likely only slightly better than mCherry, and it is unlikely that it could reveal the bird cage pattern. Thus, NG presents a rare opportunity to investigate low intensity signals in *Chlamydomonas* and plant cells.

It is possible to further optimize imaging conditions for NG. For convenience, NG is typically imaged with filter sets for FITC and EGFP. As NG's spectra are slightly longer than EGFP's, its S/B shall improve if the emission filter of the FITC/EGFP filter set is replaced with a yellow-shift shortpass filter, which is relatively easy and inexpensive to do. In theory, this filter could also further reduce the green spectra autofluorescence. This may allow detection of the NG-fusion proteins whose pattern is not as intense as EB1 comets or bird cage. Also, gene editing replacing competitive endogenous protein will increase the S/B and reflect natural kinetics better. Creations of

new bright FPs with different spectra will expand the palette of FP tools suitable for plant research.

5.2 pH- and Na^+-induced Alternate EB1 Patterns

The shank binding and alternative patterns induced by HA and Na^+ demonstrate mechanistic complexity of the EB1 (**Figure 1.3**). While it is well established that EB1 dimer uses its two N-terminal domains to track the plus end of growing MTs, new findings are still emerging despite extensive studies for more than 2 decades (Su *et al.*, 1995). As odd as it seems, it was only revealed recently that simply binding to MT plus-end EB1 reduces GTP cap size and increases MT dynamic instability (Duellberg *et al.*, 2016). EB1 shank binding is by no means new. It is not surprising that shank binding increases when EB1 is over saturated (Mimori-Kiyosue *et al*., 2005; Grimaldi *et al*., 2014). Yet genetically modified systems expressing tubulins, EB variants and MAPs also can promote or inhibit EB1-MT shank binding *in vivo* (Leterrier *et al.*, 2011; Goldspink *et al.*, 2013; Thomas *et al.*, 2016). Cryo-electron tomography of reconstituted MTs and EB1 also revealed primarily shank binding (Guesdon *et al.*, 2016). Interestingly, shank binding is found to be cell cycle dependent in Xenopus egg extracts (Tirnauer et al., 2002). Specifically, shank binding occurs in the interphase extracts but not mitotic extracts. However, it was not clear if shank binding is relevant physiologically or pathologically. These long-standing mystifying observations could be explained by reversible redistribution of EB1 to MT shank induced by rising $[H^+]_{in}$ and $[Na^+]_{in}$.

Shank binding could be significant functionally in several non-mutual exclusive manners, depending on the saturation degree of EB1 and the molecules that are

inadvertently recruited to the shank. As EB1 could modulate both MT dynamics, EB1 shank binding may increase MT stability, consistent with the apparent freezing of the bird-cage pattern induced by light (**Figure 3.1**). Also, it may contribute to Na^+-induced ectopic nucleation, branching and bundling, perhaps through EB1-recruited effectors. Decoration of MTs with EB1 could modulate MAPs' actions or trafficking along MTs. In addition, the effector molecules could potentially affect a number of reactions, such as nucleation, branching, bundling and severing of MTs. Together, they may manifest as altered cellular processes supported by the MT system.

5.3 pH-induced Changes in MT Dynamics

Given the broad effect of pH, it is not surprising that the MT system is sensitive to pH (Regula *et al.*, 1981). This study shows how sensitive it is and how pH reshapes the MT system in real time *in vivo*. These discoveries in turn provide experimental evidence supporting the hypothesis that pH regulates vital cellular processes, such as the cell cycle, through MTs. They also demonstrate that *Chlamydmonas* is an *in vivo* system for investigating additional concerns caused by ocean acidification.

The pH clock hypothesis proposes that changes of intracellular pH regulates the cell cycle by affecting microtubule dynamics (Gagliardi and Shain, 2013). It is founded on the correlation of cyclic pH fluctuation with the cell cycle in many cells. Typically, pH shifts to basic in the mitotic phase during which MT kinetics is heightened. Reduction of intracellular pH prevents assembly of the MT in sea urchin eggs after the sperm incorporation, which arrests the fertilization process (Schatten *et al.*, 1986). Aside from the temporal correlation, it is proposed that pH guides pollen tube elongation based on

the spatial correlation of four semi-overlapping zones of MTs, actins, calcium and low pH (Cardenas *et al.*, 2008). Despite the correlation and the important roles of the MT system in cellular processes that require trafficking and motions, the broad effects of pH question if pH-induced effects on MTs are specific, if the effects are secondary to other events, and whether the changes are relevant. These concerns were addressed by concentration-dependent pH-induced changes in the MT system in real time (**Figure 3.2 and 3.4d**). As pH is decreasing, the bird cage pattern appears first, followed by MT growth stops and hastened shortening. The swiftness and gravity of these effects proportional to H^+ concentrations suggest direct effects of pH on MTs and perhaps also EB1.

The effective pH levels, inferred based on deflagellation, are likely consistent with the range of pH changes during the cell cycle, between 6.8 – 6.3. The swiftness of the responses is ideal for the control of the progression in the cell cycle as well as mitosis in which each phase occurs decisively and accurately. It will be of interest to measure the precise pH throughout mitosis to learn if pH changes precede the onset of each phase. One possibility is that the pH level is fine tuned to switch on each phase. Or pH is generally higher during mitosis, conferring an overall high level of MT dynamics. As pH could signal sweeping changes in the MT system, I propose that H^+ could be considered as a 2^{nd} messenger like Ca^{2+} but selectively for the MT system. Considering the important role of the MT system, it is plausible that pH homeostasis is tightly controlled because pH changes might cause the broad effects through pH's signaling of MTs.

Swift changes in the MT system by intracellular acidification demand a consideration that is not common for studies of the MT system - ocean acidification. As

accumulation of anthropogenic CO_2 accelerates, so does ocean acidification and intracellular acidification. It is projected that pH will drop 0.1 unit by 2050. Notably, this seemingly minor change in logarithmic scale actually equates with ~41% increase in $[H^+]$ (Orr *et al.*, 2005). Such increase is known to perturb shell formation of marine organisms which convert bicarbonate into calcium bicarbonate (Orr *et al.*, 2005; Waldbusser *et al.*, 2013; Fitzer *et al.*, 2016). While this drastic effect on shell-forming animals alone is alarming from the standpoints of ecology and economy, broad ramifications are not apparent. It is important to point out that 5 mM and 7.5 mM HA that trigger the striking switch of *Chlamydomonas* MT from the bird cage pattern to rapid shortening is equivalent to a difference of 0.09 pH unit. This further demonstrates different MT behaviors under different pH levels. It will be important to determine the exact $[H^+]_{in}$ that switches respective changes. Predictably around pH 6.3 or higher is sufficient to depolymerize MTs, since only 7.5 mM HA triggers deflagellation that occurs when intracellular pH drops to 6.3 (**Figure 3.4d**). It is also crucial to measure how CO_2 levels affect intracellular acidification in representative marine species. In addition, given the sensitivity of plant MTs to salt stress, it will be informative to investigate how pH affects the MT system in representative plant cells, alone or in combination with salt stress.

Given the broad involvement of the MT system in diverse cellular processes, especially intracellular trafficking and related cell division, intracellular acidification could alter the physiology in fundamental ways - either MT-supported processes or straining the capacity of pH homeostasis. It is worthwhile to point out that the enormous green algae family contributes to at least 70% of oxygen production on earth (Walker, 1980). It may not be farfetched that intracellular acidification from ocean acidification

alters the physiology of green algae in general, and consequently O_2 output at a global scale.

5.4 Na^+-induced Changes in MT Dynamics

It has been appreciated for a long time that the plant MT system is susceptible to various stresses, including salt stress and osmostress (Shoji, 2006; Wang *et al.*, 2011a; Fujita *et al.*, 2013). The changes are not merely pathological consequences. Perturbation studies with Taxol suggest that Na^+-induced MT reorganization is crucial for plant seedlings to survive stresses, perhaps through changes in the cell wall (Wang *et al.*, 2007). In the same line, Na^+-induced cold-resistant MTs could be one of the means for organisms to survive in cold environments. It is possible that cold adaptation of plant cells may change $[Na^+]$ or osmolarity to render a cold-resistant MT system. So far plant studies have not yet manipulated $[Na^+]_{in}$ directly. If the plant MT system also exhibits rapid and distinct changes in responses to a range of $[Na^+]_{in}$, the MT system may serve as the sensor for salt and osmolarity for plant cells.

Relative to $[K^+]_{in}$, $[Na^+]_{in}$ is low in general (Maathuis, 2014). The potential generated from the disparate distributions of these two ions across the plasma membrane could be exploited for different purposes. While animal cells possess channels and exchangers to sense and maintain $[Na^+]_{in}$, how plant cells sense and respond to the related changes in $[Na^+]$ and osmolarity remains an enigma (Maathuis, 2014). Accumulated evidence indicates that cytoskeletons are mechanical sensors (Hoshijima, 2006; Liang *et al.*, 2014; Stachowiak *et al.*, 2014; Haswell and Verslues, 2015). In particular, it was demonstrated recently that osmoneurons sense osmolarity using MTs linked to channels

(Prager-Khoutorsky *et al.*, 2014). Hyperosmolarity deforms the plasma membrane, leading to MT deformation and changes in channel conductivity. One possibility is that salt-induced changes in plant MTs trigger downstream pathways, either through MT-linked channels or exchanger, or through redistribution of molecules, such as plant specific EB1c that might be redeployed to the nucleus through a nuclear localization sequence during electrolyte imbalance(Komaki *et al.*, 2010). With the new strategies developed in this dissertation, it should be possible to investigate the plant MT system in the context of salt stresses, osmolarity stress, cold acclimation and EB1c distributions in real time.

Because Na^+ and K^+ have similar chemical properties, it is unlikely that $[Na^+]_{in}$ is sensed through ionic interaction. A plant sodium binding protein that behaves like the prototype calcium sensor, calmodulin (Haeseleer *et al.*, 2002), is an appealing idea. Although MT system is largely conserved across all known eukaryotic species, sequences of animal and plant tubulin and MAPs do diverge, some more so than the others (Gardiner, 2013). The diverged sequences in plant proteins could be candidate sodium binding motifs.

5.5 An EB1 Capacitor Model

Based on the reversibility of induced EB1 shank binding in *Chlamydomonas* (**Figure 3.3 and 3.4**), I propose a working model - MTs are an EB1 capacitor which binds EB1 (charge) at the shank rapidly but disassociates (discharges) slowly in response to changes in pH or $[Na^+]_{in}$. I envisage that this property could be used to fine tune

available free EB1 in the cytosol that in turn modulates MT dynamics and switches reactions occurring at MT plus ends.

It was demonstrated that depletion of free cytosolic EB1 by RNAi reduced MT dynamics (Rogers *et al.*, 2002). As the EB1 shank population rises nearly instantly during intracellular acidification and EB1 comet length is highly sensitive to $[Na^+]_{in}$ (**Figure 3.3 and 3.5C**), I speculate that pH and $[Na^+]_{in}$ might significantly reduce the free cytosolic population, perhaps analogous to the RNAi depletion (Rogers *et al.*, 2002). It is possible that the depletion of cytosolic EB1 and/or EB1 shank binding reduces MT dynamics to a degree that the system freezes. This model could be tested *in vivo* to measure the populations at the shank and in the cytosol respectively. It can also be tested in a reconstituted system comprised of purified *Chlamydmonas* tubulins and EB1 that allows quantification of MT dynamics and EB1-MT interplay under varying concentrations of Na^+. This system also will test whether the effects of Na^+ are direct or through other MAPs or EB1's recruit.

5.6 Diversifications of Fluorescent Flagella as Microscopy Standards

Switches of EB1-NG intensity and patterns illustrate the importance of developing tools for easy measurement of fluorescence intensity. Amounts of EB1 in the shank or plus end of MTs could foster the development of a quantitative model describing the remobilization of EB1 populations. RSP3-NG flagella showcase the principle of ratiometric quantification of FP intensity to determine FP numbers. For accurate measurements, fluorescent flagella and unknown samples should contain identical fluorophores. Because of the proliferation of FPs with diverse optical properties,

I foresee that fluorescent flagella with uniformly distributed fluorescent fusion proteins of different stoichiometry and spectra will be of great value.

While I have created the first-generation fluorescent flagella using RSP3 as a FP carrier, the intensity is dim compared to other objects (**Figure 4.4**). Brighter fluorescent flagella standards could be generated using carrier axonemal proteins with a higher stoichiometry. One candidate is flagella-associated protein 20 (FAP20) that distributes continuously at the seam of A and B tubules in all 9 outer doublets, in contrast to the two radial spokes per 96 nm (Yanagisawa *et al.*, 2014). By comparing the intensity of flagella with RSP3-FP or FAP20-FP, it will be possible to determine the precise FAP20 stoichiometry. This strategy could be used to measure stoichiometry of any unknown axonemal proteins. Once the stoichiometry is determined, FAP20-FP flagella could serve as another suite of standards tailored to objects of brighter intensity.

Another diversification is to expand the spectra of fluorescent flagella. In theory, axonemal proteins could carry any available FPs. Aside from the existing EGFP and NG fluorescent flagella, flagella carrying the commonly used FPs, such as YFP, mCherry and tdTomato, could broaden the applications of fluorescent flagella as standards. In addition, it is possible to engineer dual color fluorescent flagella for two color imaging.

Given the diverse fluorophores used in fluorescence microscopy, it could be of value to develop flagellar standards wherein users can switch fluorophores. One option is to engineer fusion protein carrying a SNAP-tag (Juillerat *et al.*, 2003), which could be conjugated to fluorophores *in vitro* by users when needed. By swapping carriers and protein tags, it is possible to create an array of new standards that are suitable for the increasing variation of fluorescence microscopy techniques.

BIBLIOGRAPHY

Akhmanova, A., and Steinmetz, M.O. (2010). Microtubule +TIPs at a glance. J Cell Sci *123*, 3415-3419. doi:10.1242/jcs.062414

Akhmanova, A., and Steinmetz, M.O. (2015). Control of microtubule organization and dynamics: two ends in the limelight. Nat Rev Mol Cell Bio *16*, 711-726. doi:10.1038/nrm4084

Applegate, K.T., Besson, S., Matov, A., Bagonis, M.H., Jaqaman, K., and Danuser, G. (2011). plusTipTracker: Quantitative image analysis software for the measurement of microtubule dynamics. J Struct Biol *176*, 168-184. doi:10.1016/j.jsb.2011.07.009

Arikawa, M., and Suzaki, T. (2002). Reactivation of Ca2+-dependent cytoplasmic contraction in permeabilized cell models of the heliozoon Echinosphaerium akamae. Cell Motil Cytoskeleton *53*, 267-272. doi:10.1002/cm.10071

Bloodgood, R.A., and Levin, E.N. (1983). Transient Increase in Calcium Efflux Accompanies Fertilization in Chlamydomonas. Journal of Cell Biology *97*, 397-404. doi:DOI 10.1083/jcb.97.2.397

Bornens, M. (2008). Organelle positioning and cell polarity. Nat Rev Mol Cell Bio *9*, 874-886. doi:10.1038/nrm2524

Bower, R., Tritschler, D., Vanderwaal, K., Perrone, C.A., Mueller, J., Fox, L., Sale, W.S., and Porter, M.E. (2013). The N-DRC forms a conserved biochemical complex that maintains outer doublet alignment and limits microtubule sliding in motile axonemes. Mol Biol Cell *24*, 1134-1152. doi:10.1091/mbc.E12-11-0801

Braun, F.J., and Hegemann, P. (1999). Direct measurement of cytosolic calcium and pH in living Chlamydomonas reinhardtii cells. Eur J Cell Biol *78*, 199-208. doi:10.1016/S0171-9335(99)80099-5

Buey, R.M., Mohan, R., Leslie, K., Walzthoeni, T., Missimer, J.H., Menzel, A., Bjelic, S., Bargsten, K., Grigoriev, I., Smal, I., Meijering, E., Aebersold, R., Akhmanova,

A., and Steinmetz, M.O. (2011). Insights into EB1 structure and the role of its C-terminal domain for discriminating microtubule tips from the lattice. Mol Biol Cell *22*, 2912-2923. doi:10.1091/mbc.E11-01-0017

Cannon, C., van Adelsberg, J., Kelly, S., and Al-Awqati, Q. (1985). Carbon-dioxide-induced exocytotic insertion of H+ pumps in turtle-bladder luminal membrane: role of cell pH and calcium. Nature *314*, 443-446. doi:10.1038/314443a0

Cardenas, L., Lovy-Wheeler, A., Kunkel, J.G., and Hepler, P.K. (2008). Pollen tube growth oscillations and intracellular calcium levels are reversibly modulated by actin polymerization. Plant Physiol *146*, 1611-1621. doi:10.1104/pp.107.113035

Cocco, G., Chu, D.C., and Pandolfi, S. (2010). Colchicine in clinical medicine. A guide for internists. Eur J Intern Med *21*, 503-508. doi:10.1016/j.ejim.2010.09.010

Conduit, P.T., Wainman, A., and Raff, J.W. (2015). Centrosome function and assembly in animal cells. Nat Rev Mol Cell Bio *16*, 611-624. doi:10.1038/nrm4062

Deisseroth, K. (2011). Optogenetics. Nat Methods *8*, 26-29. doi:10.1038/nmeth.f.324

Dhonukshe, P., Laxalt, A.M., Goedhart, J., Gadella, T.W.J., and Munnik, T. (2003). Phospholipase D activation correlates with microtubule reorganization in living plant cells. Plant Cell *15*, 2666-2679. doi:10.1105/tpc.014977

Diener, D.R. (1993). Assembly of flagellar radial spoke proteins in Chlamydomonas: identification of the axoneme binding domain of radial spoke protein 3. The Journal of Cell Biology *123*, 183-190. doi:10.1083/jcb.123.1.183

Dixit, R. (2004). Encounters between Dynamic Cortical Microtubules Promote Ordering of the Cortical Array through Angle-Dependent Modifications of Microtubule Behavior. THE PLANT CELL ONLINE *16*, 3274-3284. doi:10.1105/tpc.104.026930

Duellberg, C., Cade, N.I., Holmes, D., and Surrey, T. (2016). The size of the EB cap determines instantaneous microtubule stability. Elife *5*. doi:10.7554/eLife.13470

Dymek, E.E. (2006). A kinesin-like calmodulin-binding protein in Chlamydomonas: evidence for a role in cell division and flagellar functions. Journal of Cell Science *119*, 3107-3116. doi:10.1242/jcs.03028

Ehrig, T., O'Kane, D.J., and Prendergast, F.G. (1995). Green-fluorescent protein mutants with altered fluorescence excitation spectra. FEBS Lett *367*, 163-166.

Fitzer, S.C., Chung, P., Maccherozzi, F., Dhesi, S.S., Kamenos, N.A., Phoenix, V.R., and Cusack, M. (2016). Biomineral shell formation under ocean acidification: a shift from order to chaos. Scientific Reports *6*, 21076. doi:10.1038/srep21076

Fuhrmann, M., Oertel, W., and Hegemann, P. (1999). A synthetic gene coding for the green fluorescent protein (GFP) is a versatile reporter in Chlamydomonas reinhardtii. Plant J *19*, 353-361. doi:DOI 10.1046/j.1365-313X.1999.00526.x

Fujita, S., Pytela, J., Hotta, T., Kato, T., Hamada, T., Akamatsu, R., Ishida, Y., Kutsuna, N., Hasezawa, S., Nomura, Y., Nakagami, H., and Hashimoto, T. (2013). An Atypical Tubulin Kinase Mediates Stress-Induced Microtubule Depolymerization in Arabidopsis. Curr Biol *23*, 1969-1978. doi:10.1016/j.cub.2013.08.006

Fujiu, K., Nakayama, Y., Iida, H., Sokabe, M., and Yoshimura, K. (2011). Mechanoreception in motile flagella of Chlamydomonas. Nature Cell Biology *13*, 630-632. doi:10.1038/ncb2214

Gagliardi, L.J., and Shain, D.H. (2013). Is intracellular pH a clock for mitosis? Theor Biol Med Model *10*, 8. doi:10.1186/1742-4682-10-8

Gao, X., Zhang, F., Hu, J., Cai, W., Shan, G., Dai, D., Huang, K., and Wang, G. (2016). MicroRNAs modulate adaption to multiple abiotic stresses in Chlamydomonas reinhardtii. Scientific Reports *6*, 38228. doi:10.1038/srep38228

Gardiner, J. (2013). The evolution and diversification of plant microtubule-associated proteins. The Plant Journal *75*, 219-229. doi:10.1111/tpj.12189

Gardner, M.K., Zanic, M., and Howard, J. (2013). Microtubule catastrophe and rescue. Current Opinion in Cell Biology *25*, 14-22. doi:10.1016/j.ceb.2012.09.006

Gather, M.C., and Yun, S.H. (2014). Bio-optimized energy transfer in densely packed fluorescent protein enables near-maximal luminescence and solid-state lasers. Nature Communications *5*, 5722. doi:10.1038/ncomms6722

Ghaemmaghami, S., Huh, W.-K., Bower, K., Howson, R.W., Belle, A., Dephoure, N., O'Shea, E.K., and Weissman, J.S. (2003). Global analysis of protein expression in yeast. Nature *425*, 737-741. doi:10.1038/nature02046

Gibbon, B.C., and Kropf, D.L. (1994). Cytosolic pH Gradients Associated with Tip Growth. Science *263*, 1419-1421. doi:10.1126/science.263.5152.1419

Goldspink, D.A., Gadsby, J.R., Bellett, G., Keynton, J., Tyrrell, B.J., Lund, E.K., Powell, P.P., Thomas, P., and Mogensen, M.M. (2013). The microtubule end-binding protein EB2 is a central regulator of microtubule reorganisation in apico-basal epithelial differentiation. Journal of Cell Science *126*, 4000-4014. doi:10.1242/jcs.129759

Gorman, D.S., and Levine, R.P. (1965). Cytochrome F and Plastocyanin - Their Sequence in Photosynthetic Electron Transport Chain of Chlamydomonas Reinhardi. P Natl Acad Sci USA *54*, 1665-&. doi:DOI 10.1073/pnas.54.6.1665

Grimaldi, A.D., Maki, T., Fitton, B.P., Roth, D., Yampolsky, D., Davidson, M.W., Svitkina, T., Straube, A., Hayashi, I., and Kaverina, I. (2014). CLASPs are required for proper microtubule localization of end-binding proteins. Dev Cell *30*, 343-352. doi:10.1016/j.devcel.2014.06.026

Grossman, A.R., Lohr, M., and Im, C.S. (2004). Chlamydomonas reinhardtii in the landscape of pigments. Annu Rev Genet *38*, 119-173. doi:10.1146/annurev.genet.38.072902.092328

Guesdon, A., Bazile, F., Buey, R.M., Mohan, R., Monier, S., Garcia, R.R., Angevin, M., Heichette, C., Wieneke, R., Tampe, R., Duchesne, L., Akhmanova, A., Steinmetz, M.O., and Chretien, D. (2016). EB1 interacts with outwardly curved and straight regions of the microtubule lattice. Nat Cell Biol *18*, 1102-1108. doi:10.1038/ncb3412

Gupta, A., Diener, D.R., Sivadas, P., Rosenbaum, J.L., and Yang, P. (2012). The versatile molecular complex component LC8 promotes several distinct steps of flagellar assembly. The Journal of Cell Biology *198*, 115-126. doi:10.1083/jcb.201111041

Habbig, S., and Liebau, M.C. (2015). Ciliopathies - from rare inherited cystic kidney diseases to basic cellular function. Mol Cell Pediatr *2*, 8. doi:10.1186/s40348-015-0019-1

Haeseleer, F., Imanishi, Y., Sokal, I., Filipek, S., and Palczewski, K. (2002). Calcium-binding proteins: intracellular sensors from the calmodulin superfamily. Biochem Biophys Res Commun *290*, 615-623. doi:10.1006/bbrc.2001.6228

Hardham, A.R. (2013). Microtubules and biotic interactions. The Plant Journal *75*, 278-289. doi:10.1111/tpj.12171

Harris, E.H. (2001). Chlamydomonas as a Model Organism. Annu Rev Plant Physiol Plant Mol Biol *52*, 363-406. doi:10.1146/annurev.arplant.52.1.363

Harris, J.A., Liu, Y., Yang, P., Kner, P., and Lechtreck, K.F. (2015). Single-particle imaging reveals intraflagellar transport-independent transport and accumulation of EB1 in Chlamydomonas flagella. Molecular Biology of the Cell *27*, 295-307. doi:10.1091/mbc.e15-08-0608

Hashimoto, T. (2015). Microtubules in Plants. The Arabidopsis Book *13*, e0179. doi:10.1199/tab.0179

Haswell, E.S., and Verslues, P.E. (2015). The ongoing search for the molecular basis of plant osmosensing. The Journal of General Physiology *145*, 389-394. doi:10.1085/jgp.201411295

Hegemann, P., and Berthold, P. (2009). Sensory Photoreceptors and Light Control of Flagellar Activity. In: The Chlamydomonas Sourcebook: Elsevier BV, 395-429. doi:10.1016/b978-0-12-370873-1.00050-2

Hegemann, P., and Moglich, A. (2011). Channelrhodopsin engineering and exploration of new optogenetic tools. Nat Methods *8*, 39-42. doi:10.1038/Nmeth.F.327

Heim, R., Cubitt, A.B., and Tsien, R.Y. (1995). Improved green fluorescence. Nature *373*, 663-664. doi:10.1038/373663b0

Helenius, J., Brouhard, G., Kalaidzidis, Y., Diez, S., and Howard, J. (2006). The depolymerizing kinesin MCAK uses lattice diffusion to rapidly target microtubule ends. Nature *441*, 115-119. doi:10.1038/nature04736

Hepler, P.K. (2015). The Cytoskeleton and Its Regulation by Calcium and Protons. Plant Physiology *170*, 3-22. doi:10.1104/pp.15.01506

Heuser, T., Dymek, E.E., Lin, J.F., Smith, E.F., and Nicastro, D. (2012). The CSC connects three major axonemal complexes involved in dynein regulation. Molecular Biology of the Cell *23*, 3143-3155. doi:10.1091/mbc.E12-05-0357

Hilton, L.K., Meili, F., Buckoll, P.D., Rodriguez-Pike, J.C., Choutka, C.P., Kirschner, J.A., Warner, F., Lethan, M., Garces, F.A., Qi, J., and Quarmby, L.M. (2016). A Forward Genetic Screen and Whole Genome Sequencing Identify Deflagellation Defective Mutants in Chlamydomonas, Including Assignment of ADF1 as a TRP Channel. G3: Genes|Genomes|Genetics. doi:10.1534/g3.116.034264

Hoegh-Guldberg, O., Mumby, P.J., Hooten, A.J., Steneck, R.S., Greenfield, P., Gomez, E., Harvell, C.D., Sale, P.F., Edwards, A.J., Caldeira, K., Knowlton, N., Eakin, C.M., Iglesias-Prieto, R., Muthiga, N., Bradbury, R.H., Dubi, A., and Hatziolos, M.E. (2007). Coral Reefs Under Rapid Climate Change and Ocean Acidification. Science *318*, 1737-1742. doi:10.1126/science.1152509

Horst, C.J., Fishkind, D.J., Pazour, G.J., and Witman, G.B. (1999). An insertional mutant ofChlamydomonas reinhardtii with defective microtubule positioning. Cell Motility and the Cytoskeleton *44*, 143-154. doi:10.1002/(sici)1097-0169(199910)44:2<143::aid-cm6>3.0.co;2-3

Hoshijima, M. (2006). Mechanical stress-strain sensors embedded in cardiac cytoskeleton: Z disk, titin, and associated structures. Am J Physiol Heart Circ Physiol *290*, H1313-1325. doi:10.1152/ajpheart.00816.2005

Huang, B. (1981). Radial spokes of Chlamydomonas flagella: genetic analysis of assembly and function. The Journal of Cell Biology *88*, 80-88. doi:10.1083/jcb.88.1.80

Husic, H.D., and Tolbert, N.E. (1986). Effect of Osmotic Stress on Carbon Metabolism in Chlamydomonas reinhardtii: Accumulation of Glycerol as an Osmoregulatory Solute. PLANT PHYSIOLOGY *82*, 594-596. doi:10.1104/pp.82.2.594

Jensen, R.E., Aiken Hobbs, A.E., Cerveny, K.L., and Sesaki, H. (2000). Yeast mitochondrial dynamics: Fusion, division, segregation, and shape. Microscopy Research and Technique *51*, 573-583. doi:10.1002/1097-0029(20001215)51:6<573::aid-jemt7>3.0.co;2-2

Jiang, X., and Stern, D. (2009). Mating and tetrad separation of Chlamydomonas reinhardtii for genetic analysis. J Vis Exp. doi:10.3791/1274

Jinkerson, R.E., and Jonikas, M.C. (2015). Molecular techniques to interrogate and edit the Chlamydomonas nuclear genome. Plant J *82*, 393-412. doi:10.1111/tpj.12801

Juillerat, A., Gronemeyer, T., Keppler, A., Gendreizig, S., Pick, H., Vogel, H., and Johnsson, K. (2003). Directed evolution of O6-alkylguanine-DNA alkyltransferase for efficient labeling of fusion proteins with small molecules in vivo. Chem Biol *10*, 313-317.

Kaganovich, D., Kopito, R., and Frydman, J. (2008). Misfolded proteins partition between two distinct quality control compartments. Nature *454*, 1088-1095. doi:10.1038/nature07195

Karr, T.L., Kristofferson, D., and Purich, D.L. (1980). Mechanism of Microtubule Depolymerization - Correlation of Rapid Dilution-Induced Disassembly Experiments with a Kinetic-Model for Endwise Depolymerization. Fed Proc *39*, 1819-1819.

Khmelinskii, A., Roostalu, J., Roque, H., Antony, C., and Schiebel, E. (2009). Phosphorylation-dependent protein interactions at the spindle midzone mediate cell cycle regulation of spindle elongation. Dev Cell *17*, 244-256. doi:10.1016/j.devcel.2009.06.011

Kindle, K.L. (1990). High-Frequency Nuclear Transformation of Chlamydomonas-Reinhardtii. P Natl Acad Sci USA *87*, 1228-1232. doi:DOI 10.1073/pnas.87.3.1228

King, S.M., and Witman, G.B. (1990). Localization of an Intermediate Chain of Outer Arm Dynein by Immunoelectron Microscopy. Journal of Biological Chemistry *265*, 19807-19811.

Kleinegris, D.M.M., van Es, M.A., Janssen, M., Brandenburg, W.A., and Wijffels, R.H. (2010). Carotenoid fluorescence in Dunaliella salina. J Appl Phycol *22*, 645-649. doi:10.1007/s10811-010-9505-y

Komaki, S., Abe, T., Coutuer, S., Inze, D., Russinova, E., and Hashimoto, T. (2010). Nuclear-localized subtype of end-binding 1 protein regulates spindle organization in Arabidopsis. J Cell Sci *123*, 451-459. doi:10.1242/jcs.062703

Kozminski, K.G., Johnson, K.A., Forscher, P., and Rosenbaum, J.L. (1993). A motility in the eukaryotic flagellum unrelated to flagellar beating. Proc Natl Acad Sci U S A *90*, 5519-5523.

Kubo, T., Kaida, S., Abe, J., Saito, T., Fukuzawa, H., and Matsuda, Y. (2009). The Chlamydomonas Hatching Enzyme, Sporangin, is Expressed in Specific Phases of the Cell Cycle and is Localized to the Flagella of Daughter Cells Within the Sporangial Cell Wall. Plant and Cell Physiology *50*, 572-583. doi:10.1093/pcp/pcp016

Kumar, P., and Wittmann, T. (2012). +TIPs: SxIPping along microtubule ends. Trends Cell Biol *22*, 418-428. doi:10.1016/j.tcb.2012.05.005

Lang, M., Stober, F., and Lichtenthaler, H.K. (1991). Fluorescence emission spectra of plant leaves and plant constituents. Radiation and Environmental Biophysics *30*, 333-347. doi:10.1007/bf01210517

Lechtreck, K.F., Johnson, E.C., Sakai, T., Cochran, D., Ballif, B.A., Rush, J., Pazour, G.J., Ikebe, M., and Witman, G.B. (2009). The Chlamydomonas reinhardtii BBSome is an IFT cargo required for export of specific signaling proteins from flagella. J Cell Biol *187*, 1117-1132. doi:10.1083/jcb.200909183

Lefebvre, P.A. (1978). Flagellar elongation and shortening in Chlamydomonas. IV. Effects of flagellar detachment, regeneration, and resorption on the induction of flagellar protein synthesis. The Journal of Cell Biology *78*, 8-27. doi:10.1083/jcb.78.1.8

Leterrier, C., Vacher, H., Fache, M.P., d'Ortoli, S.A., Castets, F., Autillo-Touati, A., and Dargent, B. (2011). End-binding proteins EB3 and EB1 link microtubules to ankyrin G in the axon initial segment. Proc Natl Acad Sci U S A *108*, 8826-8831. doi:10.1073/pnas.1018671108

Liang, X., Madrid, J., and Howard, J. (2014). The Microtubule-Based Cytoskeleton Is a Component of a Mechanical Signaling Pathway in Fly Campaniform Receptors. Biophysical Journal *107*, 2767-2774. doi:10.1016/j.bpj.2014.10.052

Lieuvin, A. (1994). Intrinsic microtubule stability in interphase cells. The Journal of Cell Biology *124*, 985-996. doi:10.1083/jcb.124.6.985

Lindemann, C.B., and Lesich, K.A. (2010). Flagellar and ciliary beating: the proven and the possible. J Cell Sci *123*, 519-528. doi:10.1242/jcs.051326

Lloyd, C., and Chan, J. (2004). Microtubules and the shape of plants to come. Nat Rev Mol Cell Bio *5*, 13-22. doi:10.1038/nrm1277

Lohret, T.A., McNally, F.J., and Quarmby, L.M. (1998). A role for katanin-mediated axonemal severing during Chlamydomonas deflagellation. Mol Biol Cell *9*, 1195-1207.

Maathuis, F.J. (2014). Sodium in plants: perception, signalling, and regulation of sodium fluxes. J Exp Bot *65*, 849-858. doi:10.1093/jxb/ert326

Malhotra, B., and Glass, A.D.M. (1995). Potassium Fluxes in Chlamydomonas reinhardtii (II. Compartmental Analysis). Plant Physiology *108*, 1537-1545. doi:10.1104/pp.108.4.1537

Marshall, W.F., and Rosenbaum, J.L. (2001). Intraflagellar transport balances continuous turnover of outer doublet microtubules. The Journal of Cell Biology *155*, 405-414. doi:10.1083/jcb.200106141

Matov, A., Applegate, K., Kumar, P., Thoma, C., Krek, W., Danuser, G., and Wittmann, T. (2010). Analysis of microtubule dynamic instability using a plus-end growth marker. Nat Methods *7*, 761-768. doi:10.1038/nmeth.1493

Maurer, Sebastian P., Cade, Nicholas I., Bohner, G., Gustafsson, N., Boutant, E., and Surrey, T. (2014). EB1 Accelerates Two Conformational Transitions Important for Microtubule Maturation and Dynamics. Curr Biol *24*, 372-384. doi:10.1016/j.cub.2013.12.042

Maurer, Sebastian P., Fourniol, Franck J., Bohner, G., Moores, Carolyn A., and Surrey, T. (2012). EBs Recognize a Nucleotide-Dependent Structural Cap at Growing Microtubule Ends. Cell *149*, 371-382. doi:10.1016/j.cell.2012.02.049

Melki, R., Carlier, M.F., Pantaloni, D., and Timasheff, S.N. (1989). Cold Depolymerization of Microtubules to Double Rings - Geometric Stabilization of Assemblies. Biochemistry *28*, 9143-9152.

Merchant, S.S., Prochnik, S.E., Vallon, O., Harris, E.H., Karpowicz, S.J., Witman, G.B., Terry, A., Salamov, A., Fritz-Laylin, L.K., Marechal-Drouard, L., Marshall, W.F., Qu, L.H., Nelson, D.R., Sanderfoot, A.A., Spalding, M.H., Kapitonov, V.V., Ren, Q., Ferris, P., Lindquist, E., Shapiro, H., Lucas, S.M., Grimwood, J., Schmutz, J., Cardol, P., Cerutti, H., Chanfreau, G., Chen, C.L., Cognat, V., Croft, M.T., Dent, R., Dutcher, S., Fernandez, E., Fukuzawa, H., Gonzalez-Ballester, D., Gonzalez-Halphen, D., Hallmann, A., Hanikenne, M., Hippler, M., Inwood, W., Jabbari, K., Kalanon, M., Kuras, R., Lefebvre, P.A., Lemaire, S.D., Lobanov, A.V., Lohr, M., Manuell, A., Meier, I., Mets, L., Mittag, M., Mittelmeier, T., Moroney, J.V., Moseley, J., Napoli, C., Nedelcu, A.M., Niyogi, K., Novoselov, S.V., Paulsen, I.T., Pazour, G., Purton, S., Ral, J.P., Riano-Pachon, D.M., Riekhof, W., Rymarquis, L., Schroda, M., Stern, D., Umen, J., Willows, R., Wilson, N., Zimmer, S.L., Allmer, J., Balk, J., Bisova, K., Chen, C.J., Elias, M., Gendler, K., Hauser, C., Lamb, M.R., Ledford, H., Long, J.C., Minagawa, J., Page, M.D., Pan, J., Pootakham, W., Roje, S., Rose, A., Stahlberg, E., Terauchi, A.M., Yang, P., Ball, S., Bowler, C., Dieckmann, C.L., Gladyshev, V.N., Green, P., Jorgensen, R., Mayfield, S., Mueller-Roeber, B., Rajamani, S., Sayre, R.T., Brokstein, P., Dubchak, I., Goodstein, D., Hornick, L., Huang, Y.W., Jhaveri, J., Luo, Y., Martinez, D., Ngau, W.C.A., Otillar, B., Poliakov, A., Porter, A., Szajkowski, L., Werner, G., Zhou, K., Grigoriev, I.V., Rokhsar, D.S., and Grossman, A.R. (2007). The Chlamydomonas Genome Reveals the Evolution of Key Animal and Plant Functions. Science *318*, 245-250. doi:10.1126/science.1143609

Michalet, X., Pinaud, F.F., Bentolila, L.A., Tsay, J.M., Doose, S., Li, J.J., Sundaresan, G., Wu, A.M., Gambhir, S.S., and Weiss, S. (2005). Quantum dots for live cells, in vivo imaging, and diagnostics. Science *307*, 538-544. doi:10.1126/science.1104274

Miller, D.J. (1979). Are cardiac muscle cells ‘skinned’ by EGTA or EDTA? Nature *277*, 142-143. doi:10.1038/277142a0

Mimori-Kiyosue, Y., Grigoriev, I., Lansbergen, G., Sasaki, H., Matsui, C., Severin, F., Galjart, N., Grosveld, F., Vorobjev, I., Tsukita, S., and Akhmanova, A. (2005). CLASP1 and CLASP2 bind to EB1 and regulate microtubule plus-end dynamics at the cell cortex. J Cell Biol *168*, 141-153. doi:10.1083/jcb.200405094

Mitchison, T., and Kirschner, M. (1984). Dynamic instability of microtubule growth. Nature *312*, 237-242. doi:10.1038/312237a0

Mittelmeier, T.M., Boyd, J.S., Lamb, M.R., and Dieckmann, C.L. (2011). Asymmetric properties of theChlamydomonas reinhardtiicytoskeleton direct rhodopsin

photoreceptor localization. The Journal of Cell Biology *193*, 741-753. doi:10.1083/jcb.201009131

Mukhtar, E., Adhami, V.M., and Mukhtar, H. (2014). Targeting Microtubules by Natural Agents for Cancer Therapy. Mol Cancer Ther *13*, 275-284. doi:10.1158/1535-7163.Mct-13-0791

Muller-Reichert, T., Chretien, D., Severin, F., and Hyman, A.A. (1998). Structural changes at microtubule ends accompanying GTP hydrolysis: Information from a slowly hydrolyzable analogue of GTP, guanylyl (,)methylenediphosphonate. Proceedings of the National Academy of Sciences *95*, 3661-3666. doi:10.1073/pnas.95.7.3661

Mussgnug, J.H. (2015). Genetic tools and techniques for Chlamydomonas reinhardtii. Appl Microbiol Biotechnol *99*, 5407-5418. doi:10.1007/s00253-015-6698-7

Nagel, G., Ollig, D., Fuhrmann, M., Kateriya, S., Mustl, A.M., Bamberg, E., and Hegemann, P. (2002). Channelrhodopsin-1: A light-gated proton channel in green algae. Science *296*, 2395-2398. doi:DOI 10.1126/science.1072068

Nagel, G., Szellas, T., Huhn, W., Kateriya, S., Adeishvili, N., Berthold, P., Ollig, D., Hegemann, P., and Bamberg, E. (2003). Channelrhodopsin-2, a directly light-gated cation-selective membrane channel. Proceedings of the National Academy of Sciences *100*, 13940-13945. doi:10.1073/pnas.1936192100

Nillegoda, N.B., and Bukau, B. (2015). Metazoan Hsp70-based protein disaggregases: emergence and mechanisms. Frontiers in Molecular Biosciences *2*. doi:10.3389/fmolb.2015.00057

O'Brien, E.T., Salmon, E.D., and Erickson, H.P. (1997). How calcium causes microtubule depolymerization. Cell Motility and the Cytoskeleton *36*, 125-135. doi:10.1002/(sici)1097-0169(1997)36:2<125::aid-cm3>3.0.co;2-8

Oda, T., Yanagisawa, H., Yagi, T., and Kikkawa, M. (2014). Mechanosignaling between central apparatus and radial spokes controls axonemal dynein activity. The Journal of Cell Biology *204*, 807-819. doi:10.1083/jcb.201312014

Oda, Y. (2015). Cortical microtubule rearrangements and cell wall patterning. Frontiers in Plant Science *6*. doi:10.3389/fpls.2015.00236

Olmsted, J.B., and Borisy, G.G. (1975). Ionic and nucleotide requirements for microtubule polymerization in vitro. Biochemistry *14*, 2996-3005. doi:10.1021/bi00684a032

Orr, J.C., Fabry, V.J., Aumont, O., Bopp, L., Doney, S.C., Feely, R.A., Gnanadesikan, A., Gruber, N., Ishida, A., Joos, F., Key, R.M., Lindsay, K., Maier-Reimer, E., Matear, R., Monfray, P., Mouchet, A., Najjar, R.G., Plattner, G.K., Rodgers, K.B., Sabine, C.L., Sarmiento, J.L., Schlitzer, R., Slater, R.D., Totterdell, I.J., Weirig, M.F., Yamanaka, Y., and Yool, A. (2005). Anthropogenic ocean acidification over the twenty-first century and its impact on calcifying organisms. Nature *437*, 681-686. doi:10.1038/nature04095

Paredez, A.R. (2006). Visualization of Cellulose Synthase Demonstrates Functional Association with Microtubules. Science *312*, 1491-1495. doi:10.1126/science.1126551

Pedersen, L.B., Geimer, S., Sloboda, R.D., and Rosenbaum, J.L. (2003). The Microtubule Plus End-Tracking Protein EB1 Is Localized to the Flagellar Tip and Basal Bodies in Chlamydomonas reinhardtii. Curr Biol *13*, 1969-1974. doi:10.1016/j.cub.2003.10.058

Perrineau, M.-M., Zelzion, E., Gross, J., Price, D.C., Boyd, J., and Bhattacharya, D. (2014). Evolution of salt tolerance in a laboratory reared population of C hlamydomonas reinhardtii. Environmental Microbiology *16*, 1755-1766. doi:10.1111/1462-2920.12372

Picariello, T., Valentine, M., Yano, J., and Van Houten, J. (2014). Reduction of meckelin leads to general loss of cilia, ciliary microtubule misalignment and distorted cell surface organization. Cilia *3*, 2. doi:10.1186/2046-2530-3-2

Piehl, M., Tulu, U.S., Wadsworth, P., and Cassimeris, L. (2004). Centrosome maturation: Measurement of microtubule nucleation throughout the cell cycle by using GFP-tagged EB1. Proceedings of the National Academy of Sciences *101*, 1584-1588. doi:10.1073/pnas.0308205100

Pittman, J.K., Edmond, C., Sunderland, P.A., and Bray, C.M. (2008). A Cation-regulated and Proton Gradient-dependent Cation Transporter from Chlamydomonas reinhardtii Has a Role in Calcium and Sodium Homeostasis. Journal of Biological Chemistry *284*, 525-533. doi:10.1074/jbc.m807173200

Pohl, H.R., Wheeler, J.S., and Murray, H.E. (2013). Sodium and Potassium in Health and Disease. In: Metal Ions in Life Sciences: Springer Nature, 29-47. doi:10.1007/978-94-007-7500-8_2

Prachayasittikul, V., Isarankura-Na-Ayudhya, C., Tantimongcolwat, T., Nantasenamat, C., and Galla, H.-J. (2007). EDTA-induced Membrane Fluidization and Destabilization: Biophysical Studies on Artificial Lipid Membranes. Acta Biochimica et Biophysica Sinica *39*, 901-913. doi:10.1111/j.1745-7270.2007.00350.x

Prager-Khoutorsky, M., Khoutorsky, A., and Bourque, Charles W. (2014). Unique Interweaved Microtubule Scaffold Mediates Osmosensory Transduction via Physical Interaction with TRPV1. Neuron *83*, 866-878. doi:10.1016/j.neuron.2014.07.023

Quarmby, L.M. (1996). Ca2+ influx activated by low pH in Chlamydomonas. The Journal of General Physiology *108*, 351-361. doi:10.1085/jgp.108.4.351

Quarmby, L.M. (2009). Deflagellation. In: The Chlamydomonas Sourcebook: Elsevier BV, 43-69. doi:10.1016/b978-0-12-370873-1.00040-x

Rasala, B.A., Barrera, D.J., Ng, J., Plucinak, T.M., Rosenberg, J.N., Weeks, D.P., Oyler, G.A., Peterson, T.C., Haerizadeh, F., and Mayfield, S.P. (2013). Expanding the spectral palette of fluorescent proteins for the green microalga Chlamydomonas reinhardtii. The Plant Journal *74*, 545-556. doi:10.1111/tpj.12165

Ravelli, R.B.G., Gigant, B., Curmi, P.A., Jourdain, I., Lachkar, S., Sobel, A., and Knossow, M. (2004). Insight into tubulin regulation from a complex with colchicine and a stathmin-like domain. Nature *428*, 198-202. doi:10.1038/nature02393

Regula, C.S., Pfeiffer, J.R., and Berlin, R.D. (1981). Microtubule Assembly and Disassembly at Alkaline Ph. Journal of Cell Biology *89*, 45-53. doi:DOI 10.1083/jcb.89.1.45

Roberts, A.J., Kon, T., Knight, P.J., Sutoh, K., and Burgess, S.A. (2013). Functions and mechanics of dynein motor proteins. Nat Rev Mol Cell Bio *14*, 713-726. doi:10.1038/nrm3667

Robertson, A.M., and Hagan, I.M. (2008). Stress-regulated kinase pathways in the recovery of tip growth and microtubule dynamics following osmotic stress in S. pombe. Journal of Cell Science *121*, 4055-4068. doi:10.1242/jcs.034488

Rogers, S.L., Rogers, G.C., Sharp, D.J., and Vale, R.D. (2002). DrosophilaEB1 is important for proper assembly, dynamics, and positioning of the mitotic spindle. The Journal of Cell Biology *158*, 873-884. doi:10.1083/jcb.200202032

Ronkin, R.R., and Buretz, K.M. (1960). Sodium and Potassium in Normal and ParalyzedChlamydomonas. The Journal of Protozoology *7*, 109-114. doi:10.1111/j.1550-7408.1960.tb00715.x

Rose, A.S., Bradley, A.R., Valasatava, Y., Duarte, J.M., Prli, A., #263, and Rose, P.W. (2016). Web-based molecular graphics for large complexes. In: Proceedings of the 21st International Conference on Web3D Technology, Anaheim, California: ACM, 185-186. doi:10.1145/2945292.2945324

Rose, A.S., and Hildebrand, P.W. (2015). NGL Viewer: a web application for molecular visualization. Nucleic Acids Res *43*, W576-579. doi:10.1093/nar/gkv402

Rosenbaum, J.L., and Witman, G.B. (2002). Intraflagellar transport. Nat Rev Mol Cell Biol *3*, 813-825. doi:10.1038/nrm952

Rovini, A., Gauthier, G., Bergès, R., Kruczynski, A., Braguer, D., and Honoré, S. (2013). Anti-Migratory Effect of Vinflunine in Endothelial and Glioblastoma Cells Is Associated with Changes in EB1 C-Terminal Detyrosinated/Tyrosinated Status. PLoS ONE *8*, e65694. doi:10.1371/journal.pone.0065694

Royal, S. (2005). Ocean acidification due to increasing atmospheric carbon dioxide. Royal Society: [London].

Sayas, C.L., and Avila, J. (2014). Crosstalk between Axonal Classical Microtubule-Associated Proteins and End Binding Proteins during Axon Extension: Possible Implications in Neurodegeneration. J Alzheimers Dis *40*, S17-S22. doi:10.3233/Jad-132315

Schatten, G., Bestor, T., Balczon, R.O.N., Henson, J., and Schatten, H. (1986). Intracellular pH Shift Initiates Microtubule-Mediated Motility during Sea Urchin

Fertilization. Annals of the New York Academy of Sciences *466*, 940-944. doi:10.1111/j.1749-6632.1986.tb38480.x

Schibler, M.J. (1991). The colR4 and colR15 beta-tubulin mutations in Chlamydomonas reinhardtii confer altered sensitivities to microtubule inhibitors and herbicides by enhancing microtubule stability. The Journal of Cell Biology *113*, 605-614. doi:10.1083/jcb.113.3.605

Schmied, J.J., Raab, M., Forthmann, C., Pibiri, E., Wünsch, B., Dammeyer, T., and Tinnefeld, P. (2014). DNA origami–based standards for quantitative fluorescence microscopy. Nat Protoc *9*, 1367-1391. doi:10.1038/nprot.2014.079

Scholey, J.M., and Anderson, K.V. (2006). Intraflagellar transport and cilium-based signaling. Cell *125*, 439-442. doi:10.1016/j.cell.2006.04.013

Scranton, M.A., Ostrand, J.T., Fields, F.J., and Mayfield, S.P. (2015). Chlamydomonas as a model for biofuels and bio-products production. Plant J *82*, 523-531. doi:10.1111/tpj.12780

Seetapun, D., Castle, Brian T., McIntyre, Alistair J., Tran, Phong T., and Odde, David J. (2012). Estimating the Microtubule GTP Cap Size In Vivo. Curr Biol *22*, 1681-1687. doi:10.1016/j.cub.2012.06.068

Serrano, L., Montejo De Garcini, E., Hernandez, M.A., and Avila, J. (1985). Localization of the tubulin binding site for tau protein. European Journal of Biochemistry *153*, 595-600. doi:10.1111/j.1432-1033.1985.tb09342.x

Seward, H.E., and Bagshaw, C.R. (2009). The photochemistry of fluorescent proteins: implications for their biological applications. Chem Soc Rev *38*, 2842-2851.

Shaner, N.C., Lambert, G.G., Chammas, A., Ni, Y., Cranfill, P.J., Baird, M.A., Sell, B.R., Allen, J.R., Day, R.N., Israelsson, M., Davidson, M.W., and Wang, J. (2013). A bright monomeric green fluorescent protein derived from Branchiostoma lanceolatum. Nat Methods *10*, 407-409. doi:10.1038/nmeth.2413

Shaner, N.C., Steinbach, P.A., and Tsien, R.Y. (2005). A guide to choosing fluorescent proteins. Nat Methods *2*, 905-909.

Shin, S.E., Lim, J.M., Koh, H.G., Kim, E.K., Kang, N.K., Jeon, S., Kwon, S., Shin, W.S., Lee, B., Hwangbo, K., Kim, J., Ye, S.H., Yun, J.Y., Seo, H., Oh, H.M., Kim, K.J., Kim, J.S., Jeong, W.J., Chang, Y.K., and Jeong, B.R. (2016). CRISPR/Cas9-induced knockout and knock-in mutations in Chlamydomonas reinhardtii. Sci Rep *6*, 27810. doi:10.1038/srep27810

Shoji, T. (2006). Salt Stress Affects Cortical Microtubule Organization and Helical Growth in Arabidopsis. Plant and Cell Physiology *47*, 1158-1168. doi:10.1093/pcp/pcj090

Siegrist, S.E., and Doe, C.Q. (2007). Microtubule-induced cortical cell polarity. Genes Dev *21*, 483-496. doi:10.1101/gad.1511207

Sivadas, P., Dienes, J.M., St Maurice, M., Meek, W.D., and Yang, P.F. (2012). A flagellar A-kinase anchoring protein with two amphipathic helices forms a structural scaffold in the radial spoke complex. Journal of Cell Biology *199*, 639-651. doi:10.1083/jcb.201111042

Smith, E.F., and Yang, P. (2003). The radial spokes and central apparatus: Mechano-chemical transducers that regulate flagellar motility. Cell Motility and the Cytoskeleton *57*, 8-17. doi:10.1002/cm.10155

Solomon, F. (1977). Binding sites for calcium on tubulin. Biochemistry *16*, 358-363. doi:10.1021/bi00622a003

Song, Y., and Brady, S.T. (2015). Post-translational modifications of tubulin: pathways to functional diversity of microtubules. Trends Cell Biol *25*, 125-136. doi:10.1016/j.tcb.2014.10.004

Specht, S., Miller, S.B.M., Mogk, A., and Bukau, B. (2011). Hsp42 is required for sequestration of protein aggregates into deposition sites inSaccharomyces cerevisiae. The Journal of Cell Biology *195*, 617-629. doi:10.1083/jcb.201106037

Stachowiak, M.R., Smith, M.A., Blankman, E., Chapin, L.M., Balcioglu, H.E., Wang, S., Beckerle, M.C., and O'Shaughnessy, B. (2014). A mechanical-biochemical feedback loop regulates remodeling in the actin cytoskeleton. Proc Natl Acad Sci U S A *111*, 17528-17533. doi:10.1073/pnas.1417686111

Su, L.K., Burrell, M., Hill, D.E., Gyuris, J., Brent, R., Wiltshire, R., Trent, J., Vogelstein, B., and Kinzler, K.W. (1995). Apc Binds to the Novel Protein Eb1. Cancer Res *55*, 2972-2977.

Takouridis, S.J., Tribe, D.E., Gras, S.L., and Martin, G.J.O. (2015). The selective breeding of the freshwater microalga Chlamydomonas reinhardtii for growth in salinity. Bioresource Technology *184*, 18-22. doi:10.1016/j.biortech.2014.10.120

Taschner, M., and Lorentzen, E. (2016). The Intraflagellar Transport Machinery. Cold Spring Harb Perspect Biol *8*. doi:10.1101/cshperspect.a028092

Taylor, A.R., Brownlee, C., and Wheeler, G.L. (2012). Proton channels in algae: reasons to be excited. Trends in Plant Science *17*, 675-684. doi:10.1016/j.tplants.2012.06.009

Tazawa, M., and Shimmen, T. (1987). Cell Motility and Ionic Relations in Characean Cells as Revealed by Internal Perfusion and Cell Models. In: International Review of Cytology: Elsevier BV, 259-312. doi:10.1016/s0074-7696(08)61724-6

Thomas, G.E., Bandopadhyay, K., Sutradhar, S., Renjith, M.R., Singh, P., Gireesh, K.K., Simon, S., Badarudeen, B., Gupta, H., Banerjee, M., Paul, R., Mitra, J., and Manna, T.K. (2016). EB1 regulates attachment of Ska1 with microtubules by forming extended structures on the microtubule lattice. Nat Commun *7*, 11665. doi:10.1038/ncomms11665

Tirnauer, J.S. (2002). EB1-Microtubule Interactions in Xenopus Egg Extracts: Role of EB1 in Microtubule Stabilization and Mechanisms of Targeting to Microtubules. Molecular Biology of the Cell *13*, 3614-3626. doi:10.1091/mbc.02-04-0210

Tortosa, E., Galjart, N., Avila, J., and Sayas, C.L. (2013). MAP1B regulates microtubule dynamics by sequestering EB1/3 in the cytosol of developing neuronal cells. The EMBO Journal *32*, 1293-1306. doi:10.1038/emboj.2013.76

Umen, J.G. (2014). Green algae and the origins of multicellularity in the plant kingdom. Cold Spring Harb Perspect Biol *6*, a016170. doi:10.1101/cshperspect.a016170

Ustin, S.L., Gitelson, A.A., Jacquemoud, S., Schaepman, M., Asner, G.P., Gamon, J.A., and Zarco-Tejada, P. (2009). Retrieval of foliar information about plant pigment

systems from high resolution spectroscopy. Remote Sens Environ *113*, S67-S77. doi:10.1016/j.rse.2008.10.019

Verdaasdonk, J.S., Lawrimore, J., and Bloom, K. (2014). Determining absolute protein numbers by quantitative fluorescence microscopy. Method Cell Biol *123*, 347-365. doi:10.1016/B978-0-12-420138-5.00019-7

Vitre, B., Coquelle, F.M., Heichette, C., Garnier, C., Chrétien, D., and Arnal, I. (2008). EB1 regulates microtubule dynamics and tubulin sheet closure in vitro. Nature Cell Biology *10*, 415-421. doi:10.1038/ncb1703

Waldbusser, G.G., Brunner, E.L., Haley, B.A., Hales, B., Langdon, C.J., and Prahl, F.G. (2013). A developmental and energetic basis linking larval oyster shell formation to acidification sensitivity. Geophysical Research Letters *40*, 2171-2176. doi:10.1002/grl.50449

Walker, J.C.G. (1980). The Oxygen Cycle. In: The Natural Environment and the Biogeochemical Cycles, ed. O. Hutzinger, Berlin, Heidelberg: Springer Berlin Heidelberg, 87-104.

Wang, C., Li, J., and Yuan, M. (2007). Salt Tolerance Requires Cortical Microtubule Reorganization in Arabidopsis. Plant and Cell Physiology *48*, 1534-1547. doi:10.1093/pcp/pcm123

Wang, C., Zhang, L.J., and Chen, W.F. (2011a). Plant Cortical Microtubules Are Putative Sensors under Abiotic Stresses. Biochemistry-Moscow+ *76*, 320-326. doi:10.1134/S0006297911030047

Wang, L., Piao, T., Cao, M., Qin, T., Huang, L., Deng, H., Mao, T., and Pan, J. (2013). Flagellar regeneration requires cytoplasmic microtubule depolymerization and kinesin-13. Journal of Cell Science *126*, 1531-1540. doi:10.1242/jcs.124255

Wang, S., Kurepa, J., Hashimoto, T., and Smalle, J.A. (2011b). Salt Stress-Induced Disassembly of Arabidopsis Cortical Microtubule Arrays Involves 26S Proteasome-Dependent Degradation of SPIRAL1. THE PLANT CELL ONLINE *23*, 3412-3427. doi:10.1105/tpc.111.089920

Weaver, B.A. (2014). How Taxol/paclitaxel kills cancer cells. Molecular Biology of the Cell *25*, 2677-2681. doi:10.1091/mbc.e14-04-0916

Weisenberg, R.C. (1972). Microtubule Formation in vitro in Solutions Containing Low Calcium Concentrations. Science *177*, 1104-1105. doi:10.1126/science.177.4054.1104

Welschmeyer, N.A. (1994). Fluorometric Analysis of Chlorophyll-a in the Presence of Chlorophyll-B and Pheopigments. Limnol Oceanogr *39*, 1985-1992.

Westermann, B. (2008). Molecular Machinery of Mitochondrial Fusion and Fission. Journal of Biological Chemistry *283*, 13501-13505. doi:10.1074/jbc.r800011200

Wheeler, G.L., Joint, I., and Brownlee, C. (2007). Rapid spatiotemporal patterning of cytosolic Ca2+ underlies flagellar excision in Chlamydomonas reinhardtii. The Plant Journal *53*, 401-413. doi:10.1111/j.1365-313x.2007.03349.x

Williams, B.D. (1989). Molecular cloning and sequence analysis of the Chlamydomonas gene coding for radial spoke protein 3: flagellar mutation pf-14 is an ochre allele. The Journal of Cell Biology *109*, 235-245. doi:10.1083/jcb.109.1.235

Wolff, J., Sackett, D.L., and Knipling, L. (1996). Cation selective promotion of tubulin polymerization by alkali metal chlorides. Protein Science *5*, 2020-2028. doi:10.1002/pro.5560051008

Xiao, H., Verdier-Pinard, P., Fernandez-Fuentes, N., Burd, B., Angeletti, R., Fiser, A., Horwitz, S.B., and Orr, G.A. (2006). Insights into the mechanism of microtubule stabilization by Taxol. P Natl Acad Sci USA *103*, 10166-10173. doi:10.1073/pnas.0603704103

Xiong, H., Zhou, Z., Zhu, M., Lv, X., Li, A., Li, S., Li, L., Yang, T., Wang, S., Yang, Z., Xu, T., Luo, Q., Gong, H., and Zeng, S. (2014). Chemical reactivation of quenched fluorescent protein molecules enables resin-embedded fluorescence microimaging. Nature Communications *5*. doi:10.1038/ncomms4992

Yan, X. (2005). A Complex of Two Centrosomal Proteins, CAP350 and FOP, Cooperates with EB1 in Microtubule Anchoring. Molecular Biology of the Cell *17*, 634-644. doi:10.1091/mbc.e05-08-0810

Yanagisawa, H.a., Mathis, G., Oda, T., Hirono, M., Richey, E.A., Ishikawa, H., Marshall, W.F., Kikkawa, M., and Qin, H. (2014). FAP20 is an inner junction protein of doublet microtubules essential for both the planar asymmetrical

waveform and stability of flagella in Chlamydomonas. Molecular Biology of the Cell *25*, 1472-1483. doi:10.1091/mbc.e13-08-0464

Yang, P.F., Yang, C., Wirschell, M., and Davis, S. (2009). Novel LC8 Mutations Have Disparate Effects on the Assembly and Stability of Flagellar Complexes. Journal of Biological Chemistry *284*, 31412-31421. doi:10.1074/jbc.M109.050666

Yoshimura, K. (2011). Stimulus Perception and Membrane Excitation in Unicellular Alga Chlamydomonas. In: Coding and Decoding of Calcium Signals in Plants, ed. S. Luan, Berlin, Heidelberg: Springer Berlin Heidelberg, 79-91.

Zanic, M., Stear, J.H., Hyman, A.A., and Howard, J. (2009). EB1 Recognizes the Nucleotide State of Tubulin in the Microtubule Lattice. PLoS ONE *4*, e7585. doi:10.1371/journal.pone.0007585

Zhang, Q., Lin, F., Mao, T., Nie, J., Yan, M., Yuan, M., and Zhang, W. (2012). Phosphatidic Acid Regulates Microtubule Organization by Interacting with MAP65-1 in Response to Salt Stress in Arabidopsis. The Plant Cell *24*, 4555-4576. doi:10.1105/tpc.112.104182

Zhu, X.Y., Liu, Y., Sivadas, P., Gupta, A., and Yang, P.F. (2013). Molecular Tools for Studying the Radial Spoke. Cilia, Pt A *524*, 19-36. doi:10.1016/B978-0-12-397945-2.00002-0